A nonlinear approach in the quantification of numerical uncertainty by high-order methods for compressible turbulence with shocks

fluids

MDPI

Review

A Nonlinear Approach in the Quantification of Numerical Uncertainty by High-Order Methods for Compressible Turbulence with Shocks

H. C. Yee [1,*], P. K. Sweby [2], Björn Sjögreen [3] and D. V. Kotov [4,†]

[1] NASA Ames Research Center, Moffett Field, CA 94035, USA
[2] Department of Mathematics and Statistics, University of Reading, Whiteknights, Reading RG6 6AX, UK; p.k.sweby@reading.ac.uk
[3] MultiD Analyses AB, 421 65 Göteborg, Sweden; bjorn.sjogreen@multid.se
[4] Independent Researcher, Canada; dmitry.kotov84@gmail.com
* Correspondence: helen.m.yee@nasa.gov
† Self (Work done while associated with BARI, NASA Ames Research Center).

Abstract: This is a comprehensive overview on our research work to link interdisciplinary modeling and simulation techniques to improve the predictability and reliability simulations (PARs) of compressible turbulence with shock waves for general audiences who are not familiar with our nonlinear approach. This focused nonlinear approach is to integrate our **"nonlinear dynamical approach"** with our **"newly developed high order entropy-conserving, momentum-conserving and kinetic energy-preserving methods"** in the quantification of numerical uncertainty in highly nonlinear flow simulations. The central issue is that the solution space of discrete genuinely nonlinear systems is much larger than that of the corresponding **genuinely nonlinear continuous systems**, thus obtaining numerical solutions that might not be solutions of the continuous systems. Traditional uncertainty quantification (UQ) approaches in numerical simulations commonly employ linearized analysis that might not provide the true behavior of genuinely nonlinear physical fluid flows. Due to the rapid development of high-performance computing, the last two decades have been an era when computation is ahead of analysis and when very large-scale practical computations are increasingly used in poorly understood multiscale data-limited complex nonlinear physical problems and non-traditional fields. This is compounded by the fact that the numerical schemes used in production computational fluid dynamics (CFD) computer codes often do not take into consideration the genuinely nonlinear behavior of numerical methods for more realistic modeling and simulations. Often, the numerical methods used might have been developed for weakly nonlinear flow or different flow types other than the flow being investigated. In addition, some of these methods are not discretely physics-preserving (structure-preserving); this includes but is not limited to entropy-conserving, momentum-conserving and kinetic energy-preserving methods. Employing theories of nonlinear dynamics to guide the construction of more appropriate, stable and accurate numerical methods could help, e.g., (a) delineate solutions of the discretized counterparts but not solutions of the governing equations; (b) prevent numerical chaos or numerical "turbulence" leading to FALSE predication of transition to turbulence; (c) provide more reliable numerical simulations of nonlinear fluid dynamical systems, especially by direct numerical simulations (DNS), large eddy simulations (LES) and implicit large eddy simulations (ILES) simulations; and (d) prevent incorrect computed shock speeds for problems containing stiff nonlinear source terms, if present. For computation intensive turbulent flows, the desirable methods should also be efficient and exhibit scalable parallelism for current high-performance computing. Selected numerical examples to illustrate the genuinely nonlinear behavior of numerical methods and our integrated approach to improve PARs are included.

Keywords: nonlinear dynamics; discrete dynamics; dynamics of numerics; numerics of dynamics; uncertainty quantification; chaotic transients; direct numerical simulations; nonlinear approach to uncertainty quantification; high-order shock-capturing methods; entropy-conserving methods; physics-preserving (structure-preserving) methods; hybrid methods; nonlinear filter methods; momentum-conserving methods; kinetic-energy-preserving methods; compressible turbulence; gas dynamics; MHD

Citation: Yee, H.C.; Sweby, P.K.; Sjögreen, B.; Kotov, D.V. A Nonlinear Approach in the Quantification of Numerical Uncertainty by High-Order Methods for Compressible Turbulence with Shocks. *Fluids* **2024**, *9*, 250. https://doi.org/10.3390/fluids9110250

Academic Editors: D. Andrew S. Rees and Giuliano De Stefano

Received: 12 July 2024
Revised: 11 September 2024
Accepted: 14 September 2024
Published: 25 October 2024

1. Introduction

This paper presents an overview on our continuing long-term effort in reliable and accurate high-order numerical method development by integrating our earlier work on the application of nonlinear dynamical systems theory to improve the understanding of global nonlinear behavior of finite discretization and their connection to numerical uncertainties in CFD and computational physics. See [1–3] and the references cited therein for more details. Our approach is to use interdisciplinary knowledge gained from nonlinear studies to aid the construction of more appropriate and to improve high-order numerical methods for the simulation of compressible turbulent flows. The areas of application are the modeling and simulation of turbulence combustion, supersonic turbulence and computational astrophysics, and aiding the design of the next-generation spacecrafts and high-speed civil transports. Supersonic turbulence occurs in, e.g., scramjet engines, re-entry spacecrafts, black hole accretions, star formations, stellar winds and volcanic eruptions. We also employ these guiding principles as a nonlinear approach for uncertainty quantification (UQ) of multiscale CFD simulations. Due to the fact that our integrated multi-disciplinary nonlinear approach is not well known in the CFD community, the intent of this comprehensive overview is for general audiences who are not familiar with our nonlinear approach. It is hoped that the long overview will be helpful.

This nonlinear approach is particularly vital to improve the predictability and reliability for numerical simulation (PARs) of time-accurate, long-time integration of compressible turbulence with shock waves by DNS, LES and ILES computations. One of the many key contributing factors is that even though the numerical methods were designed to be stable and accurate for rapidly developing flows, they are either too dissipative, encounter nonlinear instability or exhibit aliasing error and other anomalies that drastically deviate from linear or linearized analyses in long-time integration of the aforementioned genuinely nonlinear multiscale fluid flows. For compressible turbulence with shock waves, designing methods with the minimal amount of numerical dissipation while maintaining numerical stability and accuracy is an intricate balancing act. Proper adaptive numerical dissipation control in high-order methods would provide accurate and stable solutions and play an integral role in the success of PARs. See our numerical method development for a variety of flow types and characteristics presented in [1,2,4–30]. See also a recent article by Glimm et al. concerning the nonlinear phenomena in turbulence simulations [31].

For definitions of linear, weakly nonlinear, moderately nonlinear and strongly nonlinear/genuinely nonlinear continuum systems and their discretized counterparts, see [31–39] for some definitions. Oversimplified definitions for weakly, moderately and strongly nonlinear systems are as follows: Consider a nonlinear system. Loosely speaking, a weakly nonlinear theory keeping only the first term of the Taylor series expansion as a function of the considered system variable/parameter would provide the behavior of a weakly nonlinear system as a function of the chosen variable/parameter. A moderately nonlinear system keeps the first two terms or the first three terms of the Taylor series expansion. A strongly nonlinear system keeps the high-order terms or all terms of the Taylor series expansion.

1.1. Central Issues

Often, numerical methods based on solution performance behavior for model linear or weakly nonlinear systems are employed by some practitioners to simulate highly coupled genuinely nonlinear systems. For example, we found in the open literature that some claims of computed turbulence are NOT turbulence of the chosen governing equations. In addition, some claims of transition to turbulence for a considered Reynolds number are **numerical transitions** to turbulence. Some of the causes are as follows: (a) employing diffusive methods, (b) lacking sufficient grid points, (c) trapping into a long numerical chaotic transient phase and mistakenly identifying as turbulence transitions that have already occurred, (d) introducing spatial nonlinearity by nonlinear shock-capturing schemes, (e) introducing nonlinearity by time discretizations, (f) introducing nonlinearity by grid

adaptations, (g) insufficient amount of numerical dissipation by low-dissipative high-order methods, (h) exhibiting wrong propagation speed of discontinuities by standard conservative shock-capturing methods for flows containing stiff source terms and discontinuities, (i) employing wrong numerical methods for flows with source terms and (j) employing entropy violating methods for external hypersonic blunt-body flows. Additional causes also exist but are beyond the scope of this overview. Examples to illustrate some of the causes or combined causes can be found in [1,2,4,6–8,18–24,40–42] and the references cited therein.

The central issue is that the solution space of discrete genuinely nonlinear systems is much **LARGER** than that of the corresponding **genuinely nonlinear continuous systems**, thus resulting in numerical solutions that are not solutions of the physical systems. A nonlinear method can introduce incorrect solutions when solving a linear system. Different numerical methods resulting from discretizing the same governing equations are separate discrete nonlinear dynamical systems as a function of the finite (non-zero) time step, finite grid spacing and tunable scheme parameter aside from the inherent physical parameters of the continuum governing equations. The traditional uncertainty quantification (UQ) approaches in numerical simulations often employ linearized analysis that might not provide the true behavior of the genuinely nonlinear physical flows. Linearized analysis relies on local behavior, and the convergence criterion is based on "**as the time step and grid spacing approach to zero"**. In all computational physics practices, finite (not extremely small) time steps and grid spacings are used. Unlike the linear model equations used for conventional stability and accuracy considerations in time-dependent partial different equations (PDEs), there is no equivalent unique nonlinear model equation for nonlinear hyperbolic and parabolic PDEs for fluid dynamics. A numerical method behaving in a certain way for a particular nonlinear differential equation (DE) (PDE or ordinary differential equation (ODE)) might exhibit a different behavior for a different nonlinear DE even though the DEs are of the same type. The need to guarantee PARs of genuinely nonlinear systems becomes acute when computations offer the **ONLY** way of generating this type of data-limited simulations; the lack of reliable observable data and/or experimental means is unfeasible for any of a number of possible reasons.

At the same time, due to the rapid advancement of high-performance computing, the last two decades have been an era when computation is far ahead of analysis and when very large-scale practical computations are increasingly used in poorly understood multiscale data-limited complex nonlinear physical problems and non-traditional fields. This is compounded by the fact that some of the numerical schemes used in production that applied CFD computer codes for modeling and simulations do not take into account the genuine nonlinear behavior of numerical methods. In addition, most of the numerical methods in use are not discretely physics-preserving (structure-preserving) methods. This includes but is not limited to entropy-conserving, momentum-conserving, and kinetic energy-preserving methods. For example, a well known non-physical solution exhibited by entropy-violating numerical methods raises concerns with the computation on grid-aligned blunt-body hypersonic external flow. Some key points are explained below.

Entropy-Violating Methods Relating to Carbuncle Effect in Hypersonic Blunt Body Simulations: Take, for example, in hypersonic modeling and simulations, the issue of "the carbuncle effect and hypersonic CFD simulations" has attracted numerical method developers for forty years, even before the term "carbuncle" was born [9,43–46]. There were many heated debates at some of the CFD conferences. This is due partially to some of the developers not being aware of earlier related work or due to the disconnect between entropy-violating numerical method development and applied CFD physical insights, and much more. Actually, these numerical anomalies are related to entropy-violating methods for one dimension (1D) flows, multidimensional (multi-D) flows and much more. They are also due to the added nonlinearity introduced by flux limiters by shock-capturing methods, the computation of external flow involving dimension-by-dimension approaches and the scaling of the eigenvector if Roe's Riemann solver or the local Lax–Friedrichs flux is used in the construction of the resulting numerical method. Some proposed cures to multi-D

high-speed blunt body simulation were presented as grid-aligned shock instability at the stagnation point. Some of these proposed cures did not provide the full picture or were not aware of earlier published work, e.g., [21,22,47]. In our work, we include integrated cures on the inaccuracy, stability and convergence issues aside from a multi-D entropy fix to cure the grid-aligned instability by entropy-violating methods. Our works preceded the heavily cited work of R. Sanders and J.J. Quirk [48,49]. See samples of later published works [43,50–52] on the subject. Private communication with D.K. Prabhu of NASA Ames Research Center in 2018 indicated that some of the CFD hypersonic production computer codes, e.g., DPLR and their unstructured version, continue to use a non-grid-aligned grid to avoid grid-aligned shock instability. Section VII will include excerpts from our 1980s published work [21,22,47,53], illustrating our enhancement of reliable numerical simulation for both steady and unsteady hypersonic blunt-body flows using entropy-violating methods.

Below, we expand our introductory discussion on the fundamentals of nonlinear behavior of numerical simulations further.

1.2. Treating Fluid Dynamics Equations as Dynamical Systems

Traditional fluid dynamics and CFD-related texts and reference books consider the Euler and Navier–Stokes equations in differential forms as coupled systems of nonlinear PDEs consisting of physical parameters. These equations are rarely classified as dynamical systems. Basically, fluid flow occurs in three possible regimes: turbulent, laminar and a transition region. The conditions that lead to each type of flow behavior are system-specific. Fluid dynamicists are interested in how the flow behaves as a function of one or more physical parameters. Of particular importance to fluid dynamicists is locating the critical value of the physical parameter where the fluid undergoes drastic changes in the flow behavior. Some examples are the prediction of transition to turbulence or laminar instability as a function of the Reynolds number; flow separation and stall as a function of Reynolds number and angle of attack; rotorcraft vibration as a function of rotation speed and flight speed; the occurrence of shock waves as a function of the body shape and/or Mach number; and the formation of vortices, flutter and other flow phenomena as a function of the angle of attack or other physical parameters.

One the other hand, one also can recast the study of admissible shock wave solutions of hyperbolic conservation laws as the study of the dynamics of heteroclitic orbits of a system of nonlinear ODEs [54] Another application is in the area of aiding the understanding of the topology of flow patterns (flow visualizations) of laboratory experiments, observable physical phenomena and numerical data. An additional important topic for CFD is the control and optimization of dynamical systems. This involves the application of optimization and control theory to dynamical systems. Some researchers use these interdisciplinary ideas to study, for example, the control of turbulence, the control of vortex generation and/or shock waves, the control of vibration in rotorcraft and the control of aerodynamic noise such as sonic boom and jet noise.

One historical note, the application of dynamical system theory to the study of spatiotemporal instabilities of aerodynamic and hydrodynamic flows and chaotic systems in fluid dynamics was discussed, respectively, in the 1994 and 1996 von Karman Institute for Fluid Dynamics Lecture Series. How the solution behaves as one or more of the system parameters is varied precisely belongs to the discipline of dynamical systems and bifurcation theory in applied mathematics. According to Ian Stewart (1990) [38],

"Bifurcation theory is a method for finding interesting solutions to nonlinear equations by tracking dull ones and waiting for them to lose stability".

Figure 1 shows a schematic diagram of stability of steady-state solutions arising through three types of bifurcation phenomena as a function of the system parameter α. The phenomenon of generating spurious steady-state numerical solutions (or other spurious asymptotes) by certain numerical schemes is often confused with the non uniqueness (or multiple steady states) of the governing equation. Actually, the existence of non-unique steady-state solutions of the continuum can complicate the numerics tremendously and

is independent of the occurrence of spurious asymptotes of the associated scheme. For example, assuming the governing equation has a unique steady-state solution as a function of the system parameter α for a bracketed interval, a numerical method can introduce non-unique spurious steady-state (and asymptotes) numerical solutions as time step Δt increases within the bracketed interval. Referring to the same figure for the discretized counterpart, the system parameter α of Figure 1 in this case would be $\alpha\Delta t$, indicating the possible spurious steady-state phenomena portion of the bifurcation diagram with a reduced bracketed interval of α than the allowable unique steady state for the continuum. The full bifurcation diagram as a function of system parameter will be illustrated later for some of the commonly used time discretizations. The occurrence of possible spurious steady-state solutions, e.g., spurious zero wave speed standing wave phenomena by some numerical method, can influence the reliability of unsteady (time-accurate) simulations. See Yee et al., Yee and Sweby, Lafon and Yee, Griffiths et al. and Sullivan et al. [6,23,24,35,55] for some examples and discussion.

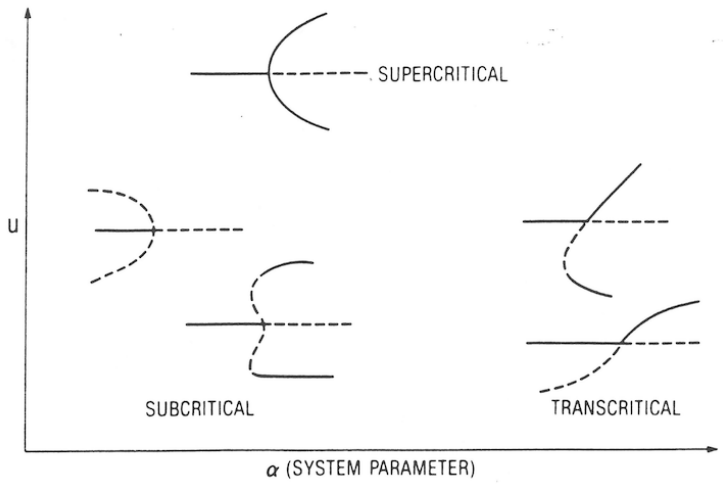

Figure 1. Stability of steady-state solutions arising through three types of bifurcation phenomena as a function of the system parameter α (- stable, - - unstable).

1.3. Isolation of the Sources of Numerical Uncertainties

In order to isolate the sources of numerical uncertainties, we need to set aside the possible discrepancy between the chosen model and the real physics and/or experimental data. Therefore, to gain first-hand insight into the "dynamics of numerics", we concentrate only on how well numerical schemes can mimic the solution behavior of the underlying governing PDEs for finite time steps and grid spacings. Even with this restriction, the study of the PARs of genuinely nonlinear compressible turbulence with shock waves encompasses elements and factors far beyond what is discussed here. The basic idea is to have a very clear distinction of numerical uncertainties from each source. These include but are not limited to the following:

- Stability and well-posedness of the governing PDEs;
- Type, order of accuracy, nonlinear stability and convergence of finite discretizations as functions of finite grid spacing, time steps and system parameters;
- Limits and barriers of existing finite discretizations for highly nonlinear stiff problems with source terms and forcing, and/or for long-time wave propagation phenomena;
- Numerical boundary condition (BC) treatments;
- Finite representation of infinite domains;
- Solution strategies in solving the nonlinear discretized equations;
- Procedures for obtaining the steady-state numerical solutions;
- Grid quality and grid adaptations;
- Multigrids;

- Domain decomposition (zonal or multicomponent approach) in solving large problems.

Although some of the numerical uncertainties can be explained and minimized by traditional numerical analysis and standard CFD practices, especially for weakly nonlinear and non-stiff governing PDEs, such practices might not be sufficient for strongly nonlinear and/or stiff problems. The need of a better understanding of the nonlinear behavior of numerical schemes being used as an integral part of computer code verification, validation and certification is needed.

1.4. Lack of Unique Nonlinear Model for Nonlinear Hyperbolic and Parabolic PDEs

As briefly mentioned earlier, a major stumbling block in genuinely nonlinear studies is that unlike the linear model equations used for conventional stability and accuracy considerations in time-dependent PDEs, there is no equivalent unique nonlinear model equation for nonlinear hyperbolic and parabolic PDEs for fluid dynamics. On one hand, a numerical method behaving in a certain way for a particular nonlinear continuum equation might exhibit a different behavior for a different nonlinear continuum equation even though they are of the same PDE type. On the other hand, even for simple nonlinear model continuum equations with known solutions, the discretized counterparts can be extremely complex to analyze, depending on the numerical methods. Except in special cases, there is no general theory at the present time to characterize the various nonlinear behaviors of the underlying discretized counterparts. Our strategy is based on the knowledge gained for nonlinear model problems with known analytical solutions to identify and explain the possible sources and remedies of numerical uncertainties in practical computations.

Throughout the discussion, the term **"discretized counterparts"** is used to mean the finite difference equations resulting from finite discretizations of the underlying DEs. The term **"dynamics"** is used loosely to mean the dynamical behavior of nonlinear dynamical systems (continuum or discrete), and **"numerics"** is used loosely to mean the numerical methods and procedures in solving dynamical systems. We would like to emphasize that in our study of the dynamics of numerics, unless otherwise stated, we always assume the continuum (governing equations) is nonlinear.

Although this overview paper is intended primarily for computational fluid dynamicists, the approaches should be useful for computational scientists, physicists, engineers and computer scientists who have a need for reliable numerical simulations.

1.5. Objective and Outline

DNS, LES, ILES and turbulence modelings are traditional methods for the simulation of compressible turbulence. The DNS, LES and ILES computations of compressible turbulence require time-accurate, nonlinearly stable methods suitable for long-time integration with minimal use of numerical dissipation, as such flows consist of the disparity of space and time scales during different stages of turbulence development. They are usually characterized by very large Reynolds numbers and even larger magnetic Reynolds numbers for magnetized turbulence in magnetohydrodynamics (MHD). In order to improve reliable compressible turbulence simulations, our interdisciplinary design of new numerical methods (a) employs quantification of numerical uncertainty via a nonlinear dynamical approach; (b) mimics and preserves physical properties of the chosen governing equations as much as possible; (c) is high order, low dissipative, low dispersive and suitable for a wide range of flow speeds within the same computational domain; (d) is suitable for flows consisting of disparity of space and time scales during different stages of turbulence development; (e) possesses high-order stable summation-by-parts (SBP) numerical boundary operators for non-periodic boundaries [56–58]; (f) is applicable for 3D spatial and time-varying deforming grids with geometric conservation law property (GCL); and (g) is nonlinear, stable, efficient and exhibits scalable parallelism for current high-performance computing.

The specific background and motivation are presented in Section 2. Sources of nonlinearities and knowledge gained from nonlinear model problems are discussed in Section 3. Section 4 discusses spurious numerics by time discretizations. Section 5 discusses the

nonlinear behavior of adaptive numerical methods. Section 6 gives a brief description on source term treatments in reacting flows to obtain the correct propagation speed of discontinuities for flows containing stiff source terms, shocks and shear layers. Section 7 devotes a large section to illustrate spurious numerics relevant to turbulent flow computations, especially relevant to false turbulent flow transitions (numerical transitions). Due to a large volume of disjoint proposed carbuncle cures devoted to the simulations of hypersonic blunt-body flows, we devote a complete Section 8 to include excerpts from [21,22] for the cures. We believe our early work presents an integrated cure related to the simulation of multi-D hypersonic blunt body and its relations with the carbuncle phenomena than some of the last thirty years of studies reported in the open literature. In particular, nonlinearity introduced by the nonlinear shock-capturing method that creates more spurious numeric than mere carbuncle cures will be discussed. Section 9 illustrates some test cases in spurious numerics related to problems with stiff source terms and our methods to minimize them. The test cases include simple scalar, simple system cases to a very complex 13 species of non-equilibrium reacting flow simulations. Section 10 gives a brief description of our high-order physical-preserving nonlinear filter methods. It discusses how numerical dissipation affects the predictability and reliability of turbulence simulation of compressible turbulence with shock waves. Several numerical examples illustrating our physical-preserving seventh-order nonlinear filter methods compared with standalone standard high-order shock-capturing methods will be included. In Section 11, we illustrate a comparison of eighth-order physical-preserving methods for several gas dynamics simulations, while Section 12 presents some concluding remarks.

2. Background, Motivation and Integrated Approach

The period of the 1970s and 1980s was an era of explosion of new numerical method developments in CFD, new theories of nonlinear dynamical systems and the beginning of increasing computer speed to aid numerical simulations of increases in complexity for modeling and simulation of fluid flows. Routinely, numerical methods were used to understand the dynamics of highly nonlinear continuum dynamical systems without analyzing the global nonlinear behavior of the numerical methods as the discrete dynamical system being used. Fast forward to three decades later, with more sophisticated developments in CFD, many new theories in nonlinear dynamical systems and quantum jumps in the computation speed of high-performance computing appeared, yet these two disciplines of **"Dynamics of Numerics"** and **"Numerics of Dynamics"** are still lacking close interactions.

This work consisted of a culmination of over 35 years of continuing research work by the authors and collaborators in bridging some of the gaps of interaction between these disciplines as a pairing to aid the development of more reliable and accurate simulations of genuinely nonlinear fluid flows. Some of the key concepts and our earlier efforts in bridging the gaps are reported in the lecture notes/long overview paper by Yee and Sweby, Yee and Sjögreen [1–3], and the references cited therein.

The dynamics of numerics work of Yee and Sweby [1,2] summarized the global nonlinear behavior of finite discretizations for constant or variable time steps and fixed or adaptive grid spacings using tools from dynamical systems theory. Detailed analysis of commonly used temporal and spatial discretizations for simple model problems was presented. The role of dynamics in the understanding of long-time behavior of numerical integration and the nonlinear stability, convergence and reliability of using time-marching approaches for obtaining steady-state numerical solutions in CFD was explored. Their study is complemented with examples of spurious behavior observed in steady and unsteady CFD computations. Numerically induced chaos and numerically induced chaotic transient can be mistaken as turbulence transitions. The CFD examples were chosen to illustrate non-apparent spurious behavior that was difficult to detect without extensive grid and temporal refinement studies, and some knowledge from dynamical systems theory. These studies revealed the various possible dangers of misinterpreting the numerical simulation of realistic complex flows. The details of published work related to Yee and Sweby [1,2]

encompass several dozens of their peer-reviewed publications and conference proceedings papers. See, e.g., [1,6–8,23,35,59–63].

The work of Yee and Sjögreen [3] presents their recent adaptive numerical dissipation control development for long-time integration of DNS, LES and ILES computations of compressible turbulence for gas dynamics and MHD. Their approach uses **adaptive blending of high-order physics-preserving non-dissipative methods (classical central, Padé (compact) and dispersion relation preserving (DRP))** with high-order shock-capturing methods in such a way that high-order shock-capturing methods are active only in the vicinity of shock/shear waves, and high gradient and spurious high-frequency oscillation regions guided by flow sensors. Typically, the adaptive blending of more than one method falls under two categories: **hybrid methods and nonlinear filter methods**. By examining the construction of these two approaches, the authors' nonlinear filter approach is more efficient and less CPU intensive while obtaining similar accuracy. The different stages of our high-order nonlinear filter method's development are also encompassed in several dozens of peer-reviewed publications and conference proceedings. See [3] and the references cited therein for more details. For some of the details, see [4,5,9–11,13–16,26–30,64,65].

Here, the key concepts of our work [1–3,6,7,23,24,35,66] are discussed first before the discussion of our integrated nonlinear approach in the quantification of numerical uncertainty and our high-order physics-preserving methods for more reliable simulation of compressible turbulence with shock waves.

2.1. Quantification of Numerical Uncertainty in the 1980s and 1990s

Since the late 1980s, many CFD-related journals imposed an editorial policy statement on numerical uncertainty, which pertained mainly to the accuracy, computer code and solution verification under the linearized analysis guidelines. See the book of Oberkampf and Roy [67] for a broader development and Glimm et al. [31] concerning the nonlinear phenomena in turbulence simulations.

However, the study of numerical uncertainties in practical modeling and simulation in computational physics and scientific computing encompasses very broad subject areas. At present, some of the numerical uncertainties can be explained and minimized by traditional numerical analysis and standard CFD practices. However, such practices might not be sufficient for strongly nonlinear and/or stiff problems. Examples of this type of problem are combustion, turbulent combustion, high speed and reacting flows, and certain turbulence models in Navier–Stokes computations. A good understanding of the nonlinear behavior of numerical schemes being used is a conduit to the quantification of numerical uncertainty and should be an integral part of code verification and validation. See [36] for the definition of highly (or genuinely) nonlinear problems.

2.2. Interaction of Dynamical Systems and Numerical Methods

During the late 1970s and 1980s, a new area of applied mathematics emerged from the interaction of dynamical system theory and numerical analysis. These developments addressed mainly mathematical principles and their applications of numerics in the understanding of the dynamics of differential equations (DEs) without discussing the connection between dynamics and numerics for initial value problems (IVPs) and initial boundary value problems (IBVPs). There was, however, some discussion on this connection for boundary value problems (BVPs) [32,68–74]. Studies of BVPs of the elliptic type continue to the present day. See, for example, the early four SIAM Conferences on Dynamical Systems (1990, 1992, 1995, 1997) and the Proceedings of IMA Conference on Dynamics of Numerics and Numerics of Dynamics, 31 July–2 August 1990, Bristol, England.

In the late 1980s, developments concerned with the connection between dynamics and numerics for IVPs and IBVPs slowly emerged. See, for example, [37,75–81]. These developments raised many interesting and important issues of concern that are useful to practitioners in computational sciences. Some of the issues are as follows: (a) Can advances in dynamical systems provide new insights into better understanding of numerical

algorithms and the construction of new ones? (b) Can these advances aid in the determination of a more reliable criterion on the use of existing numerical schemes for strongly nonlinear problems? (c) What is the influence of finite time steps and grid spacings rather than time steps and grid spacings approaching zero on the overall nonlinear behavior and stability of the scheme in terms of allowable initial data and discretized parameters? In the early 1990s, the use of dynamics to address the long-time behavior of numerical schemes for IVPs and IBVPs began to flourish. The 1990s work includes the Conference on Dynamics of Numerics and Numerics of Dynamics (University of Bristol, 31 July–2 August 1990), the Chaotic Numerics Workshop (Deakin University, Geelong, Australia, 12–16 July 1993), the Conference on Dynamical Numerical Analysis (Georgia Institute of Technology, Atlanta, Georgia, 14–16 December 1995) and the "Innovative Time Integrators Workshop" (Center for Mathematics and computer Science, Amsterdam, 6–8 November 1996, the Netherlands). These conferences were devoted almost entirely to dynamical numerical analysis. See the proceedings and references cited therein. See also [39,44,82–88]. The majority of the later developments concentrated on the long-time behavior of ODE solvers using variable step size based on local error controls [89]. This type of local error control in time enjoyed much success in controlling accuracy and stability for transient computations for ODEs. For time-dependent PDEs, the caveat is that regardless of whether finite difference (and finite volume) or finite element spatial discretization methods are employed, when time-marching approaches are used to obtain steady-state numerical solutions, local error controls similar to those used in ODE solvers that were designed for accuracy purposes are neither practical nor appropriate to use since such local step size error control methods might prevent the solution from reaching the correct steady-state solutions within a reasonable number of iterations. We note that the standard practice of using "local time step" (varied from grid point to grid point with the same CFL) in time-marching to the steady state is not the same as the variable step size based on local error controls.

Our studies indicated that the understanding of the dynamics of numerics for constant step size is necessary as many CFD practitioners employ the constant step size approach. Besides, the study of the dynamics of ODE solvers using variable step size based on local error control requires knowledge of the constant step size case [82]. In a series of papers, Yee et al. [23], Yee and Sweby [24,61,62], Sweby et al. [60], Sweby and Yee [59], and Lafon and Yee [6,7] studied the dynamics of finite discretization for constant time steps. The examples used in these papers were deliberately kept simple to permit explicit analysis. The approach was to take nonlinear model ODEs and PDEs with known explicit solutions (the most straightforward way of being sure of what is 'really' happening), discretize them according to various standard numerical methods and apply techniques from discrete dynamics to analyze the behavior of the discretized counterparts. To set the stage for later discussion, next, we discuss the connection of dynamical systems with CFD. Yee et al., Yee and Sweby, and Lafon and Yee [1,6,7,23,62,90] divide their studies into two categories, steady-state and time-accurate computations. Within each category, they further divide the governing PDEs into homogeneous and inhomogeneous (i.e., with or without source terms), and rapidly/slowly developing and long-time integration problems. The following subsections list outstanding issues of numerical uncertainties in CFD in which the tools of dynamical systems theory can play a role.

3. Sources of Nonlinearities and Knowledge Gained from Nonlinear Model Problems

One of the primary building blocks for the PAR of numerical simulations is to identify sources of nonlinearities (from the continuum governing equations and their discretized counterparts) and to isolate the elements and issues of numerical uncertainties due to these nonlinearities.

3.1. Nonlinearities Due to the Governing Equations vs. Nonlinearity Due to the Numerics

Typical sources of nonlinearities in CFD due to the physics are convection, diffusion, forcing, turbulence source terms, reacting flows, turbulence combustion, gravity in black holes, turbulence in magnetic clouds related problems or any combination of the above. Nonlinearities due to the numerics are less familiar. There are generally three major sources:

- Nonlinearities due to time discretizations: The discretized counterpart is nonlinear in the time step. Examples of this type are Runge–Kutta methods. If fixed time steps are used, spurious steady-state or spurious asymptotic numerical solutions can occur, depending on the initial condition (IC). Linear multistep methods (LMMs) [89] are linear in the time step; they do not exhibit spurious steady states, but implicit LMMs can stabilize unstable steady states. See Yee and Sweby [1,6,7,23,62,90] and the references cited therein for the dynamics of numerics of standard time discretizations. However, unconditionally stable LMMs can stabilize unstable steady states and much more.
- Nonlinearities due to spatial discretizations: The discretized counterpart can be nonlinear in the grid spacing and/or the scheme. Examples of nonlinear schemes are the total variation diminishing (TVD), essentially nonoscillatory (ENO) and weighted ENO (WENO) schemes and spatial schemes consisting of flux limiters. The resulting discretized counterparts are nonlinear (in the dependent variables) even though the governing equation is linear. See Yee [21] and the references cited therein for some forms of these nonlinear schemes.
- Nonlinearities due to complex geometries, boundary interfaces, grid generation, grid refinements and grid adaptations [59]: Each of these procedures can introduce nonlinearities even though the governing equation is linear.

3.2. Discrete Dynamical Systems and CFD

When we try to use numerical methods to gain insight into the fluid physics, there is an added new dimension to the overall problem. Even though we freeze the physical parameters of the governing equations, the resulting discretized counterparts are not just a nonlinear system of difference equations but also a nonlinear but discrete dynamical system as functions of the discretized parameter on their own. Depending on the scheme, the discretized counterparts usually preserve the steady states of the continuum. In addition, the discretized counterparts possess their own dynamics, which is usually richer than the continuum [23,24,37,76]. These resulting discrete dynamical systems are a function of all of the discretized parameters that are not present in the governing equations. This is one of the key factors in influencing the numerical solution to depart from the physical one if the governing equations are strongly nonlinear and stiff. It is important that before analyzing the dynamics of numerics, it is necessary to analyze (or understand) as much as possible the dynamical behavior of the governing equations and/or the physical problems using theories of DEs (ODEs and PDEs), dynamical systems of DEs and also physical guidelines. See, e.g., [91,92] for two specialized studies.

3.2.1. Nonlinear Numerical Methods

We define nonlinear numerical methods for time-dependent PDEs in the sense that the final algorithm is nonlinear even for the constant-coefficient linear PDE. It is well known that all of the TVD, total variation bounded (TVB), ENO and WENO schemes and related later shock-capturing methods development are nonlinear schemes. These types of schemes are known to have a slower convergence rate than classical shock-capturing methods and can occasionally produce nonphysical solutions for certain combinations of entropy-satisfying parameters and flux limiters (in spite of the fact that entropy-satisfying TVD, TVB and ENO schemes can suppress nonphysical solutions). See Yee [21] for a summary of the subject in the late 1980s. The second aspect of these nonlinear schemes is that even if the numerical method is formally of more than first order and if the approximation converges, the rate may still be only first order behind the shock (not just around the shock). This can

happen for systems where one characteristic may propagate part of the error at a shock into the smooth domain. See, e.g., Engquist and Sjögreen [93], which illustrated this phenomena with examples. Different designs of flux limiters to improve the time-marching to the steady states have been ongoing for the last 40 years, e.g., see two recent works [94,95].
Numerical Methods that are Linear vs. Nonlinear in Δt: In CFD, the usual classification of time-accurate schemes for time-marching approaches to the steady state are explicit, implicit and hybrid explicit and implicit methods. A less commonly known classification of numerical schemes for time-marching approaches is the identification of schemes that are linear or nonlinear in the time step (Δt) parameter space when applied to nonlinear DEs. All linear multistep methods (LMMs) of explicit or implicit type are linear in Δt, and all multistage Runge–Kutta methods are nonlinear in Δt. Lax–Wendroff/MacCormick and ADER [96,97] type of non-separable full discretizations also are nonlinear in Δt. For non-separable discretization methods and multistage Runge–Kutta time discretizations, the accuracy of the steady-state numerical solutions depends on Δt. A desirable property for a scheme that is linear in Δt is that, if the numerical solution converges, its steady-state numerical solutions are independent of the time step. Unconditional stable implicit LMMs' time integrators can stabilize unstable steady states. See [1,2,66] for some examples. For a representative fluid simulation example on stabilizing unstable steady states with implicit time integrators, see, e.g., Poliashenko and Yee 1995, an unpublished joint work. This unpublished work was presented at the 10th International Conference in Finite Element Methods, 5–8 January 1998, Tucson, Arizona. A summary is included in [1,2].

3.2.2. Dynamical Behavior of Numerical Approximations of ODEs vs. Time-Dependent PDEs

From our analyses and studies, we have shown that spurious numerical solutions can be independently introduced by time and spatial discretizations. Take the case where the ODEs are obtained from semi-discrete approximations of PDEs. The resulting system of ODEs contains more parameters (due to spatial discretizations) than those in the physical problems governed by ODEs. The parameters due to spatial discretizations for the semi-discrete approximation become the system parameter (instead of the discretized parameter) of the resulting system of ODEs. Depending on the differencing scheme, the resulting discretized counterparts of a PDE can be nonlinear in Δt, the grid spacing and the numerical dissipation parameters, even though the PDEs have only one parameter or none. One major consideration is that one might be able to choose a "safe" numerical method to solve the resulting system of ODEs to avoid spurious stable numerical solutions due to time discretizations. However, spurious numerical solutions, especially spatially varying spurious steady states introduced by spatial discretizations in nonlinear hyperbolic and parabolic PDEs for CFD applications, appear to be more difficult to avoid due to the use of a fixed mesh. In the case of the semi-discrete approach, such as methods of lines or finite element methods, if spurious numerical solutions due to spatial discretizations exist, the resulting ODE system has already inherited this spurious feature as part of the exact solution of the semi-discrete case. Thus, care must be taken in using the ODE solver computer packages for PDE applications. See Lafon and Yee [6,7] for a discussion.

3.2.3. Dynamics of Time-Marching Approaches to Obtain Steady-State Solutions

The use of time-marching approaches to obtain steady-state numerical solutions has been considered the method of choice in CFD for five decades since the pioneering work of Crocco [98] and Moretti and Abbett [99]. Moretti and Abbett used this approach to solve the inviscid supersonic flow over a blunt body without resorting to solving the steady form of PDEs of the mixed type. The introduction of efficient CFD algorithms of MacCormack [100], Beam and Warming [101], Briley and McDonald [102], and Steger [103] marked the beginning of numerical simulations of 2D and 3D Navier–Stokes equations for complex configurations. It enjoyed much success in computing a variety of weakly and moderately nonlinear fluid flow problems. For strongly nonlinear problems, the situation is more complicated. In addition to the understanding of the sources of nonlinearities,

it is necessary to isolate all elements and issues of numerical uncertainties due to these nonlinearities in time-marching to the steady state.

The following isolates some of the key elements and issues of numerical uncertainties in time-marching to the steady state.

Solving an IBVP with Unknown Initial Data: When time-marching approaches are employed to obtain steady-state numerical solutions, a BVP is transformed into an IBVP with unknown initial data. The time differencing in this case acts as a pseudo time. Linearized stability analysis indicates that a subset of the numerical solutions for certain ranges of the discretized parameters and numerical boundary conditions mimic the true solution behavior of the governing equation. However, it is less known that there exist asymptotic numerical solutions (including spurious steady states) that are not solutions of the continuum inside as well as outside the safe regions [23,61,62,104], depending on the initial data. Unlike nonlinear problems, the numerical solutions of linear or nearly linear problems are "independent" of the discretized parameters and initial data as long as the discretized parameters are inside the stability limit (or the Courant–Friedrich–Lewy (CFL) condition)—that is, the topological shapes of these solutions remain the same within the stability limit and accuracy of the scheme for linear behavior. It turns out that if constant step sizes are used, the stability, convergence rate and occurrence of spurious numerical solutions are intimately related to the choice of initial data (or start up solution).
Reliability of Residual Test: It is a common practice in time-marching approaches to obtaining the steady-state numerical solutions by the "local time step" (using the same CFL) via, e.g., time relaxation and multigrid. The criterion or guideline to measure the speed of convergence to the steady state is to monitor the residual of the computed solution if the quantity approaches (computer) machine zero. The danger is that if the computed solution is a spurious steady state, the residual would still approach machine zero as well.
Influence of Spurious Steady-State Numerical Solutions and Time-Accurate Simulations: The occurrence of spurious steady-state solutions by some numerical method can influence the true behavior of unsteady (time-accurate) simulations. For example, the spurious zero wave speed standing wave phenomena can interfere with the reliability of unsteady simulations. See Yee et al. and Griffiths et al. [23,35] for some discussion. Another issue is on the simulation of turbulence flows riding on top of a steady flow. See Sullivan et al. [55] for a practical physical example.

3.2.4. Non-Unique Steady-State Solutions of Nonlinear DEs vs. Spurious Asymptotes of the Numerical Methods

In the literature, the phenomenon of generating spurious steady-state numerical solutions (or other spurious asymptotes) by certain numerical schemes is often confused with the non-uniqueness (or multiple steady states) of the governing equation. In fact, the existence of non-unique steady-state solutions of the continuum can complicate the numerics tremendously and is independent of the occurrence of spurious asymptotes of the associated scheme. If possible, an analysis of the chosen nonlinear ODEs and PDEs and their dynamical behavior would help the study of the dynamics of numerical methods for nonlinear PDEs. A full understanding of the subject can shed some light on the controversy about the "true" existence of multiple steady-state solutions through numerical experiments for certain flow types of the Euler and/or Navier–Stokes equations. See, for example, Gimperlein et al. [105] for some discussion on the non-uniqueness in fluid flows.

3.3. Dynamics of Numerics via Tools from Bifurcation Theory

In many fluid problems, the solution behavior is well known for certain values of the physical parameters but unknown for other values. For these other values of the parameters, the problem might become very stiff and/or strongly nonlinear, making the available numerical schemes (or the scheme in use) intractable. In this situation, continuation methods in bifurcation theory can become very useful. If possible, one should

start with the physical parameter of a known or reliable steady state (e.g., flow behavior is usually known for low angles of attack but not for high angles of attack). One can then use a continuation method such as the improved pseudo arclength continuation method of Keller [106] (or the recent developments in this area) to solve for the bifurcation curve as a function of the physical parameter. See, e.g., early development by Doedel [32,69], Shroff and Keller [107], and Davidson [108]. The equations used are the discretized counterpart of the steady PDEs or the time-dependent PDEs. See Stephens and Shubin [74,109] for earlier related work.

If time-marching approaches are used, a reliable steady-state numerical solution (as a starting value on the correct branch of the bifurcation curve for a particular value of the physical parameter) is assumed. This starting steady-state numerical solution is assumed to have the proper time step and initial data combination and to have a grid spacing fine enough to resolve the flow feature. The continuation method will produce a continuous spectrum of the numerical solutions as the underlying physical parameter is varied until it arrives at a critical value p_c such that it either experiences a bifurcation point or fails to converge. Since we started on the correct branch of the bifurcation curve, the solution obtained before that p_c should be more reliable than if one starts with the physical parameter in question with unknown initial data and tries to stretch the limitation of the scheme. Note that by starting a reliable solution on the correct branch of the bifurcation curve, the dependence of the numerical solution on the initial data associated with time-marching methods can be avoided before a spurious bifurcation occurs.

Finally, when one is not sure of the numerical solution, the continuation method can be used to double check it. This approach can even reveal the true limitations of the existing scheme. In other words, the approach can reveal the critical physical parameter for which the numerical method breaks down. On the other hand, if one wants to find out the largest possible time step and/or grid spacing that one can use for a particular problem and physical parameter, one can also use continuation methods to trace out the bifurcation curve as a function of the time step and/or grid spacing. In this case, one can start with a small time step and/or grid spacing with the correct steady state and observe the critical discretized parameter as it undergoes instability or spurious bifurcation. Of course, this method for minimizing spurious steady states can still suffer from spurious behavior due to an under-resolved grid because of limited computer resources for complex practical problems. Practical guidelines to avoid under-resolved grids are yet another important building block toward reliable numerical simulations. The efficient treatment of solving the extremely large set of eigenvalue problems to study the type and stability of bifurcation points is yet another challenge. See, e.g., Fortin et al. [110], Davidson [108], and Shroff and Keller [107] for some discussions. Consequently, further development in numerical bifurcation analysis and new concepts in adaptive methods for time-marching to steady state hold a key to the minimization of spurious numerics.

3.4. A Primary Step to Minimize Spurious Numerics via Knowledge Gained from Nonlinear Model Problems

A straightforward first step of being sure of what is "really" happening with the nonlinear behavior of numerics is with the aid of elementary examples. Yee et al., Yee and Sweby (1991–1997), Sweby and Yee (1994–1995) and Griffiths et al. (1992a,b) [1,2,23,35,61,62,66,66,90] discuss the fundamentals of spurious behavior of commonly used time and spatial discretizations in CFD. Details of these examples can be found in their earlier papers. These examples consist of nonlinear model ODEs and PDEs with known analytical solutions. They illustrate the danger of employing fixed (constant) time steps and grid spacings. They were selected to illustrate the following different nonlinear behavior of numerical methods:

- Strong dependence of numerical solutions on initial data (numerical basins of attraction);
- Global asymptotic behavior of super-stable time discretizations;

- Occurrence of stable and unstable spurious asymptotes **above** the linearized stability limit of the scheme (for constant time steps);
- Occurrence of stable and unstable spurious steady states **below** the linearized stability limit of the scheme (for constant time steps);
- **Stabilization** of unstable physical steady states by implicit and semi-implicit methods;
- Interplay of initial data and time steps on the occurrence of spurious numerical asymptotes;
- Interference with the dynamics of the underlying implicit scheme by procedures in solving the nonlinear algebraic equations (resulting from implicit discretizations of the continuum equations);
- Dynamics of the linearized implicit Euler scheme solving the time-dependent equations to obtain steady states vs. Newton's method solving the steady equation;
- Spurious numerics independently introduced by spatial and time discretizations;
- Convergence problems and spurious behavior of high-resolution shock-capturing methods;
- Numerically induced and suppressed (spurious) chaos, and numerically induced chaotic transients;
- Spurious numerics generated by grid adaptations;
- Effect of spurious numerical standing wave in unsteady computations;
- Wrong propagation speed of discontinuities for problems containing stiff source terms.

We denote "spurious numerical solutions (and asymptotes)" to mean numerical solutions (asymptotes) that are solutions (asymptotes) of the discretized counterparts but are not solutions (asymptotes) of the underlying DEs. We also include steady-state solutions, periodic solutions, limit cycles, chaos and strange attractors as part of asymptotic solutions of the DEs and the corresponding discretized counterparts. See [111,112] for the definition of chaos and strange attractors. Super-stable scheme here refers to the region of numerical stability enclosing the physical instability of the true solution of the governing equation.

Aside from earlier studies by the authors and us, the aforementioned investigator, some later work carried out by Alicia Serfaty de Markus and Ronald E. Mickens [113,114] discussed the suppression of numerically induced chaos and reduction of computational errors. Their work was independently studied in 1999 and 2005 for different applications.

4. Dynamics of Numerics of Time Discretizations and Representative Examples

In this section, we briefly include the procedures we used for the study and select basic numerical examples on the dynamics of numerics by time discretizations.

4.1. Basin of Attraction of the Continuum vs. Basin of Attractions of the Discretized Counterparts

Strong dependence of solutions on initial data by the continuum and its discretized counterparts can be best analyzed by comparing the basin of attraction of the continuum and its discretized counterparts. The definition of basin of attraction will be defined shortly. It is one of the key tools to the understanding of spurious numerics. Unconditional stable time discretizations might have the property of a "numerical basin of attraction" that is larger than the underlying "exact basin of attraction" of the continuum as it can stabilize unstable steady states. Multistage Runge–Kutta methods can contribute to extra spurious steady states and asymptotes. In order to have a basic understanding of dynamical behavior of numerical methods for constant time steps, we take continuum models with known explicit solutions, discretize them according to various standard numerical methods commonly used in CFD and apply techniques from discrete dynamics to analyze the behavior of the resulting systems and to compare the nonlinear behavior of these schemes. Consequently, some of the schemes used for illustration might obviously not be suitable for that particular nonlinear model or spurious dynamics could have been avoided easily under that environment.

In our series of published work [1,2,23,35,61,62,66,90], we performed studies to gain a better understanding of the global asymptotic nonlinear behavior of (a) multistage Runge–Kutta type time discretizations and (b) explicit and implicit linear multipstep (LMM) time discretizations, including super-stable implicit LMMs. Examples of nonlinear effect caused by grid adaptation and super-stable implicit total variation diminishing (TVD) schemes on the overall performance of the numerical procedures were given. Some methods to minimize spurious steady-state numerical solutions were discussed. Here, only the fundamental concepts of strong dependence of computed solutions on initial data, basins of attraction of the continuum vs. basins of attraction of the corresponding numerical basins of attractions for two simple nonlinear scalar ODEs are shown. Here, "Exact" Basin of Attraction is a set of all initial data asymptotically approaching that asymptote for the continuum-governing equations. We use the terms "exact" basin of attraction and "numerical" basin of attraction to mean the basin of attraction of the DE and basin of attraction of the underlying discretized counterpart for the considered numerical method.

Consider the simple scalar autonomous ODE,

$$du/dt = S(u). \tag{1}$$

Here, autonomous ODEs are for $S(u)$ not explicitly dependent on t, i.e., not $S(u,t)$. The two scalar first-order autonomous nonlinear ODEs are

$$du/dt = S(u) = \alpha u(1-u) \tag{2}$$

$$du/dt = S(u) = \alpha u(1-u)(b-u), 0 < b < 1. \tag{3}$$

Equation (2) is the simplified form of the heavily studied logistic ODE with an application in biology and applied mechanics. The fixed points (steady states) u^* for (2) with $\alpha > 0$ are when $S(u^*) = 0$—that is, $u^* = 0$ (unstable) and $u^* = 1$ (stable), and no additional periodic solutions or asymptotes exist. The basin of attraction for the stable fixed point u is the entire positive half-plan for all values of $\alpha > 0$.

The fixed points for Equation (3) with $\alpha > 0$ are $u^* = 0$ (unstable), $u^* = 1$ (unstable) and $u^* = b$ (stable), and no additional periodic solutions or asymptotes exist. The basin of attraction for the stable fixed point $u^* = b$ is $0 < u < 1$ for all $\alpha > 0$.

Denoting Δt as the time step, and considering $\alpha > 0$, Figure 2 shows the full bifurcation diagram of the explicit Euler method for the logistic ODE. Note that the explicit Euler applied to the logistic ODE resulted in the famous logistic map $u^{n+1} = \alpha u^n(1-u^n)$. Unlike the underlying logistic ODE, it is well known that the logistic map possesses very rich dynamical behavior such as period-doubling (of period 2^n for any positive integer n) cascades resulting in chaos (Feigenbaum [34]). One can find Figure 2 in most of the elementary dynamical systems text books. The exact values of $r = \alpha\Delta t$ for all of the period-doubling bifurcation points and chaotic windows (intervals of r) were discovered by Feigenbaum in the late 1970s. Interested readers should consult these elementary textbooks for details. In other words, one can obtain the analytical (exact) behavior of the spurious asymptotes and numerical (spurious) chaos of the logistic map. Next, we look at more time discretizations used to solve these two different ODEs, where we present full bifurcation diagrams overlaid on top of their corresponding numerical basin of attractions.

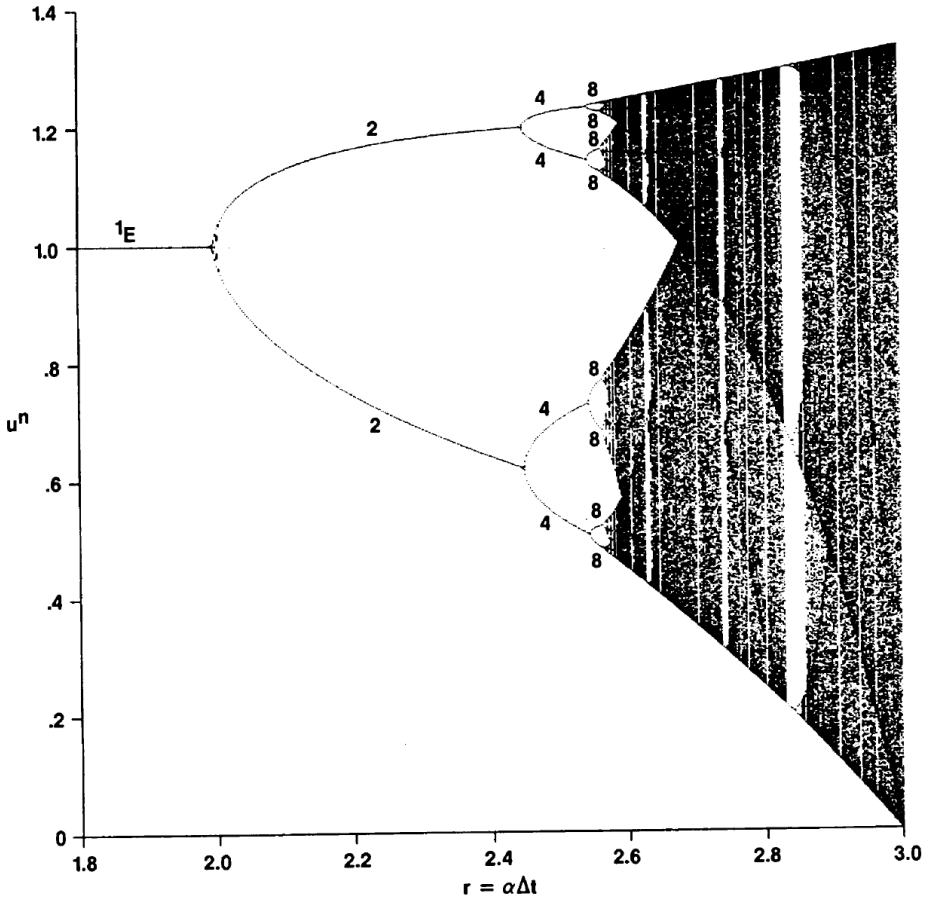

Figure 2. Full bifurcation diagram of the explicit Euler method for the logistic ODE with $\alpha > 0$.

4.2. Strong Dependence of Solutions on Initial Data by Examining Their Corresponding Basin of Attraction

It is possible that for the same Δt but two different initial data or vice versa, the scheme can converge to two different distinct numerical solutions of which one or neither of them is the true solution of the underlying ODE. Thus, in a situation where there is no prior information about the exact steady-state solution, and where a time-marching approach is used to obtain the steady-state numerical solution when initial data are not known, a stable spurious steady-state could be computed and mistaken for the correct steady-state solution. We need the corresponding "full" bifurcation diagram using this numerical approach, and we must over-plot all of the individual bifurcation diagrams of existing asymptotes of any period and chaotic attractors obtained by using the entire domain of u values as starting initial data. Thus, a better method in numerically approximating the full bifurcation diagram is dividing the domain of interest of the u axis into equal increments and using these u values as initial data. The "full" bifurcation diagram is obtained by simply over-plotting all of these individual diagrams on one. Figure 2 shows the "full" bifurcation diagrams for the corresponding fixed point diagrams of the logistic ODE using the explicit Euler method for $\alpha > 0$. Note that the full bifurcation diagram computed this way might miss some of the windows of bifurcations that occur inside the intervals of the adjacent r and/or the initial data values.

The commonly used time discretizations in CFD are multistage Runge–Kutta methods, implicit Euler/linearized implicit Euler, trapezoidal/linearized trapezoidal, three-level backward differentiation formula (BDF) and their linearized versions. Figures 3–12 illustrate selected full bifurcation diagrams with the corresponding basins of attraction overlaid

on top for the two scalar ODE models. One can see how the different methods exhibit spurious steady states and asymptotes. The complexity of the different basins of attraction and their differences in comparing with the two ODE models are also shown.

Figure 3 shows the bifurcation diagrams and basins of attraction for the logistic ODE using four different Runge–Kutta methods (Modified Euler, Improved Euler, Kutta and the classical fourth-order Runge–Kutta (R-K 4)).

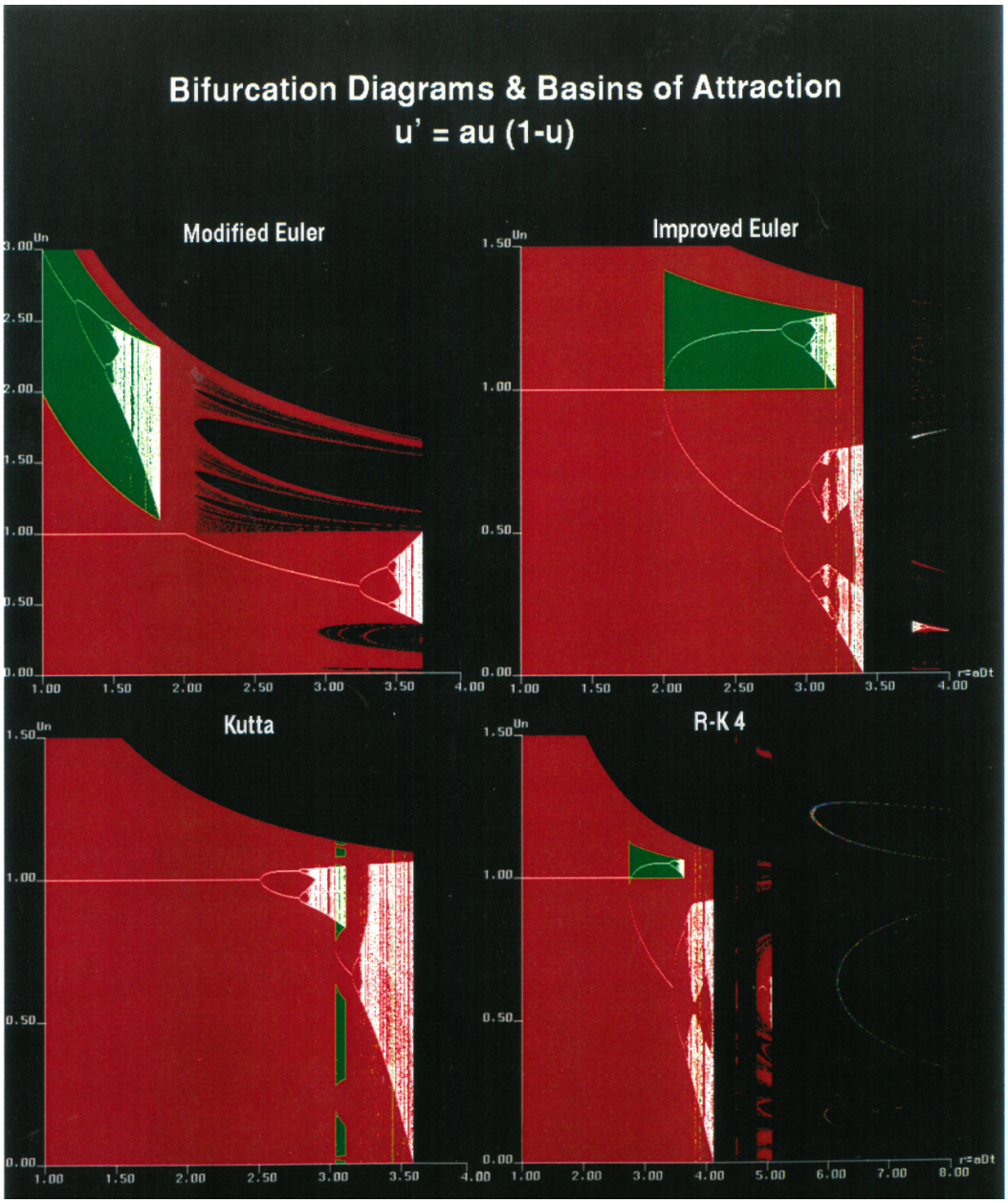

Figure 3. Full bifurcation diagram and basin of attraction for the logistic ODE using four different Runge–Kutta methods (Modified Euler, Improved Euler, Kutta and the classical fourth-order Runge–Kutta (R-K 4)), $\alpha > 0$.

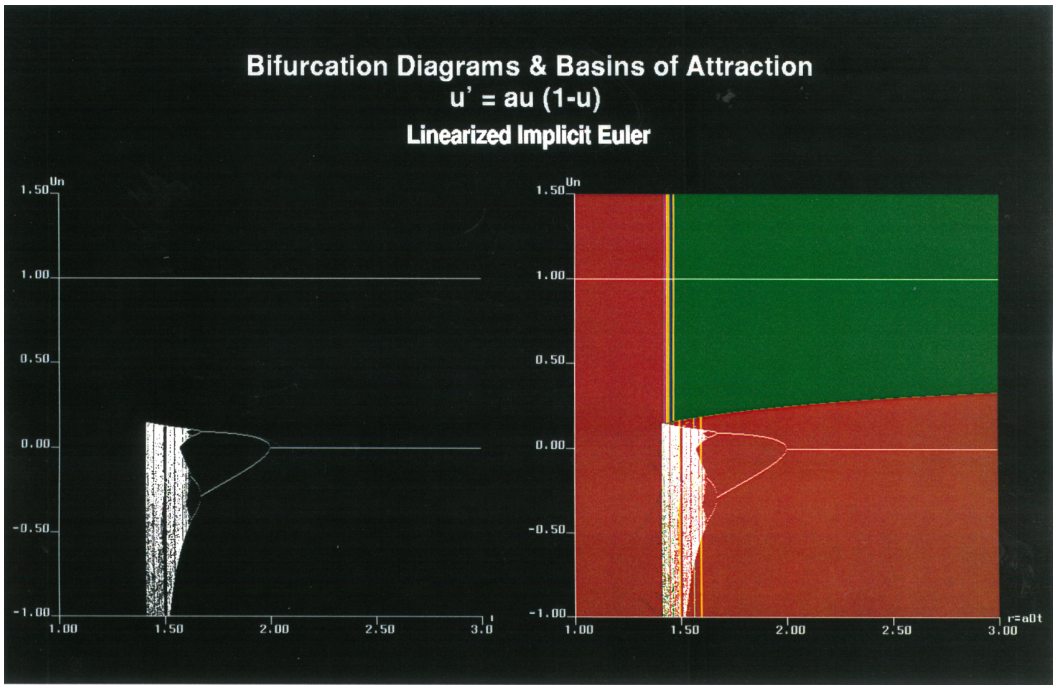

Figure 4. Full bifurcation diagram and basin of attraction for the logistic ODE using linearized implicit Euler, $\alpha > 0$.

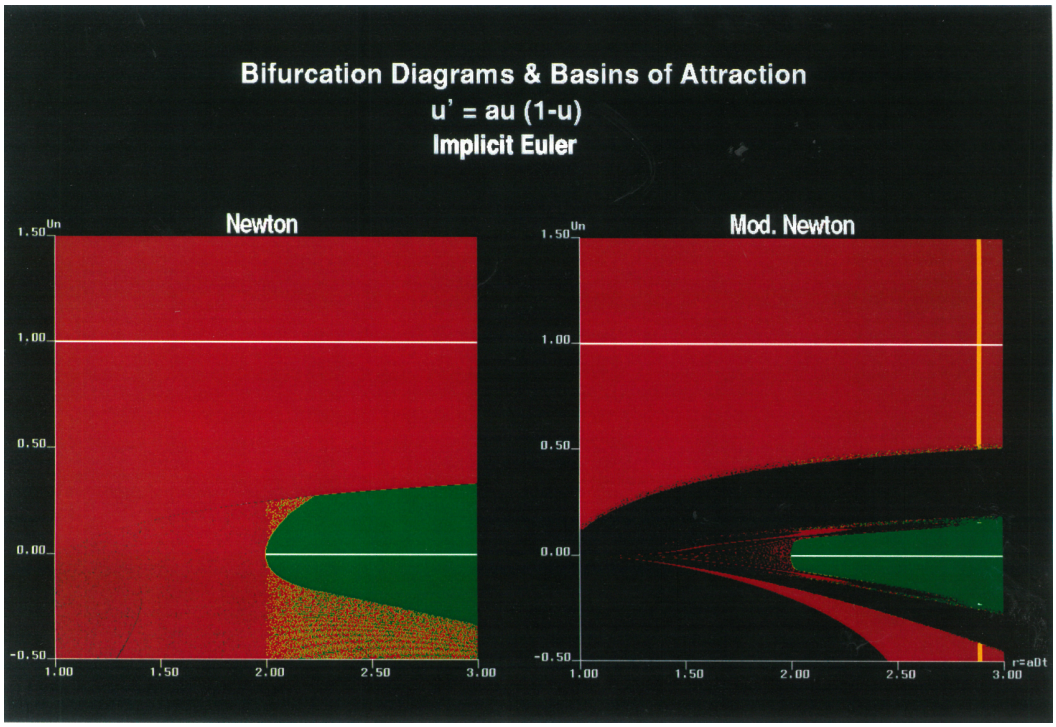

Figure 5. Full bifurcation diagram and basin of attraction for the logistic ODE using implicit Euler, $\alpha > 0$.

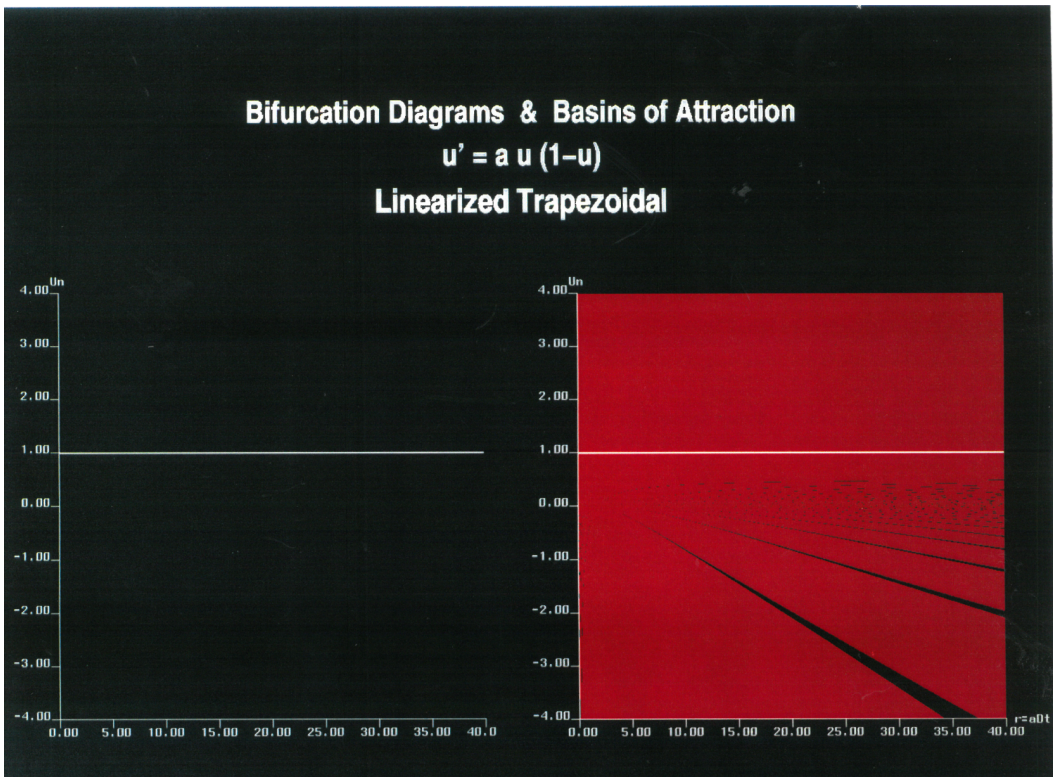

Figure 6. Full bifurcation diagram and basin of attraction for the logistic ODE using linearized trapezoidal, $\alpha > 0$.

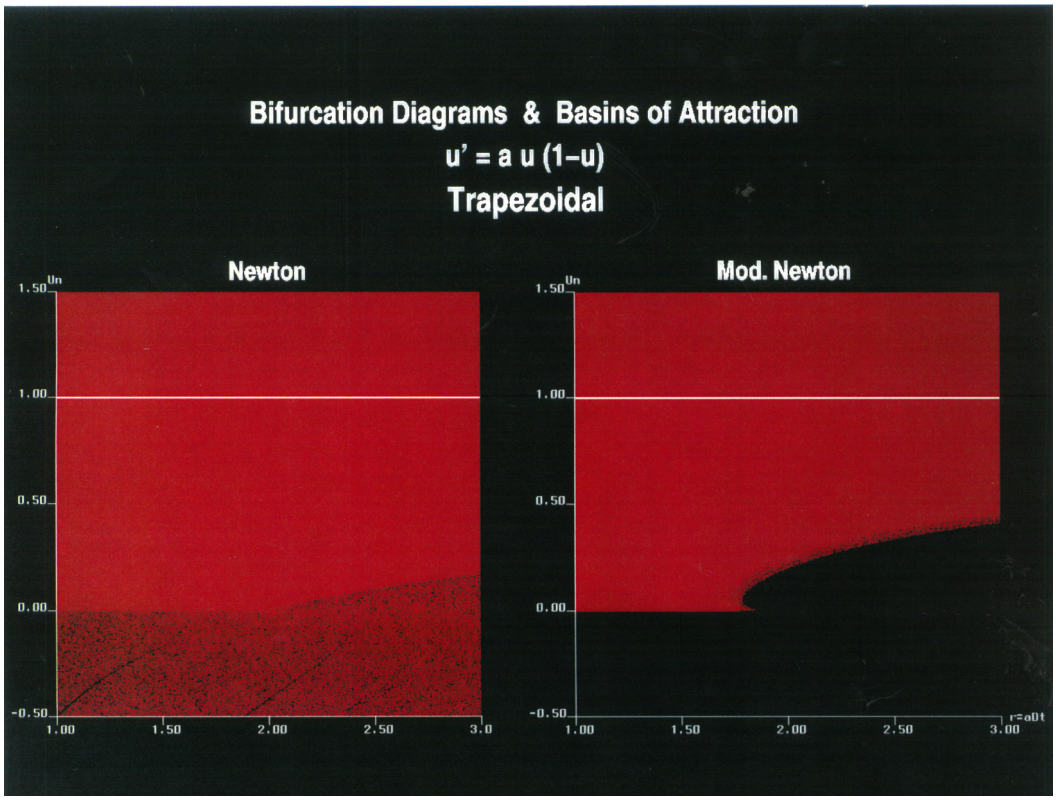

Figure 7. Full bifurcation diagram and basin of attraction for the logistic ODE using trapezoidal, $\alpha > 0$.

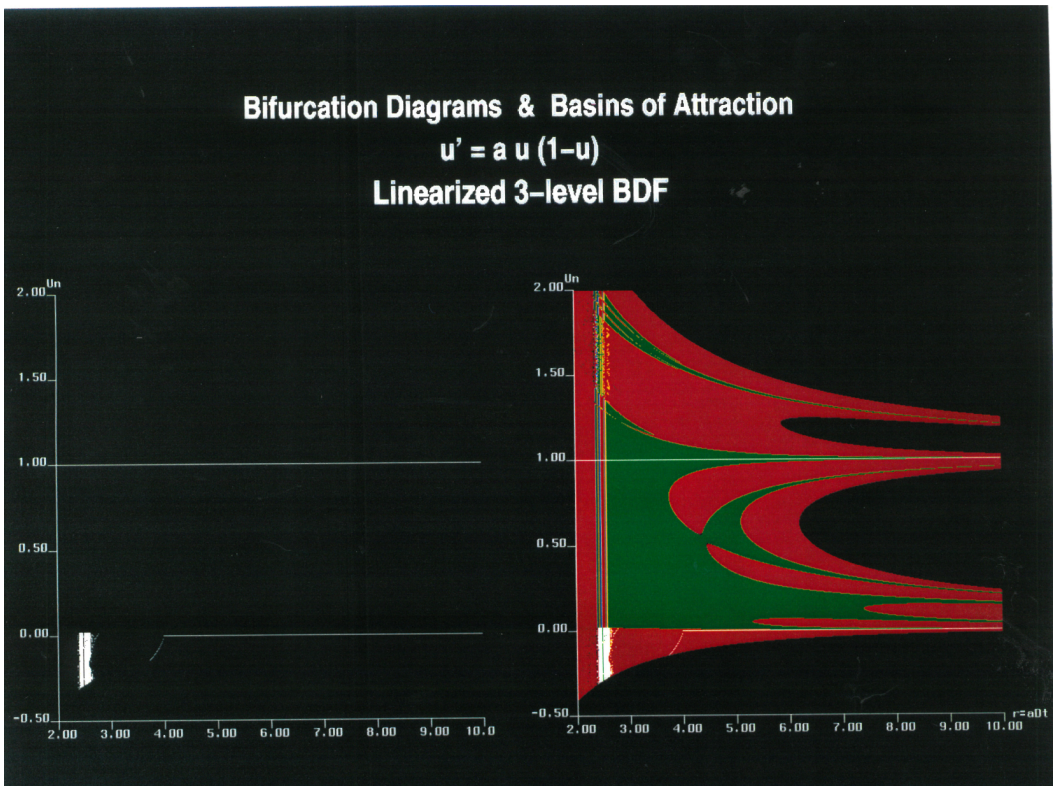

Figure 8. Full bifurcation diagram and basin of attraction for the logistic ODE using linearized 3-level BDF, $\alpha > 0$.

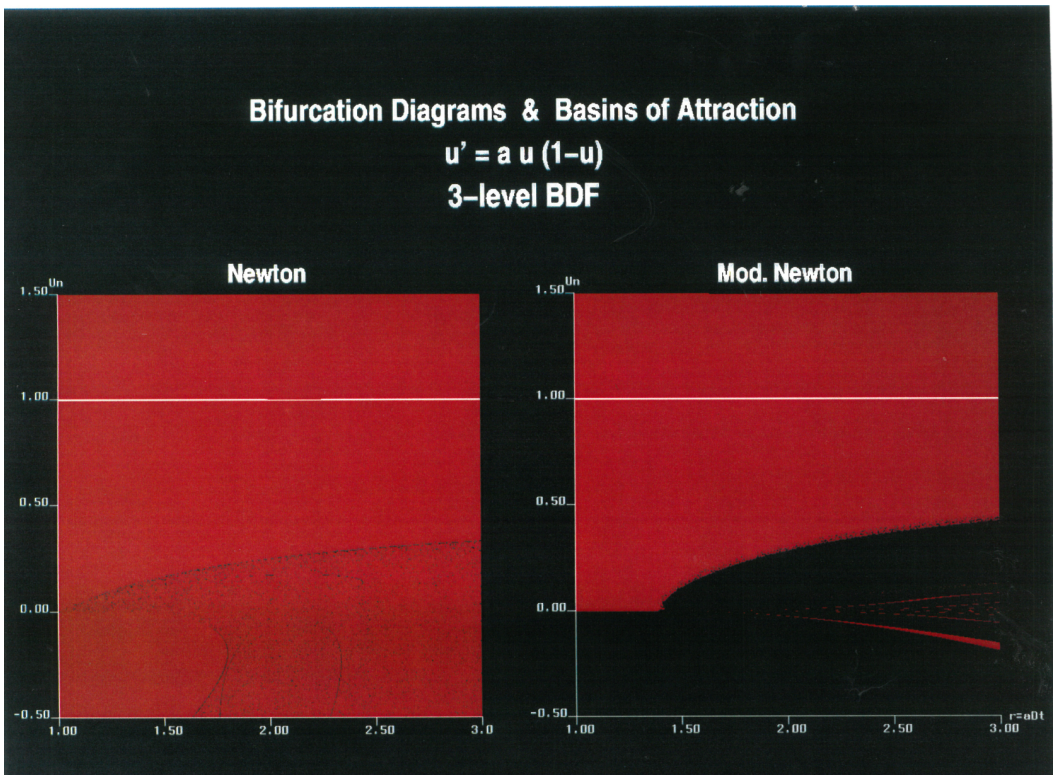

Figure 9. Full bifurcation diagram and basin of attraction for the logistic ODE using 3-level BDF, $\alpha > 0$.

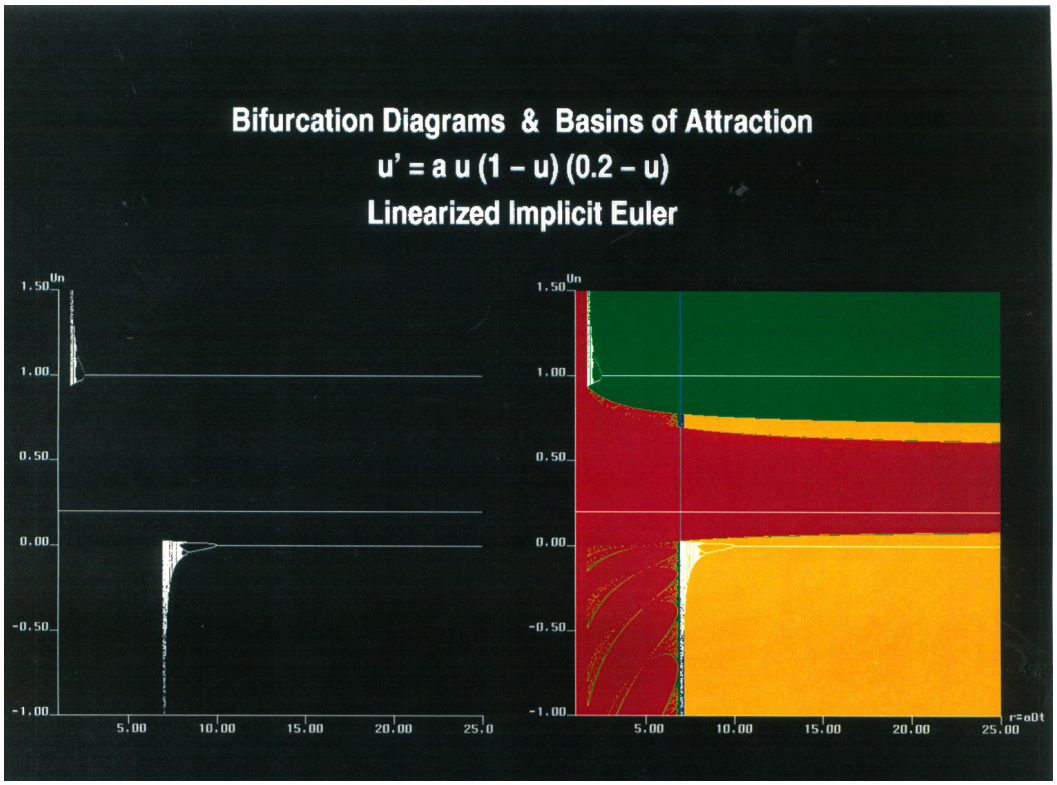

Figure 10. Full bifurcation diagram and basin of attraction for ODE (3) using linearized implicit Euler, $\alpha > 0$.

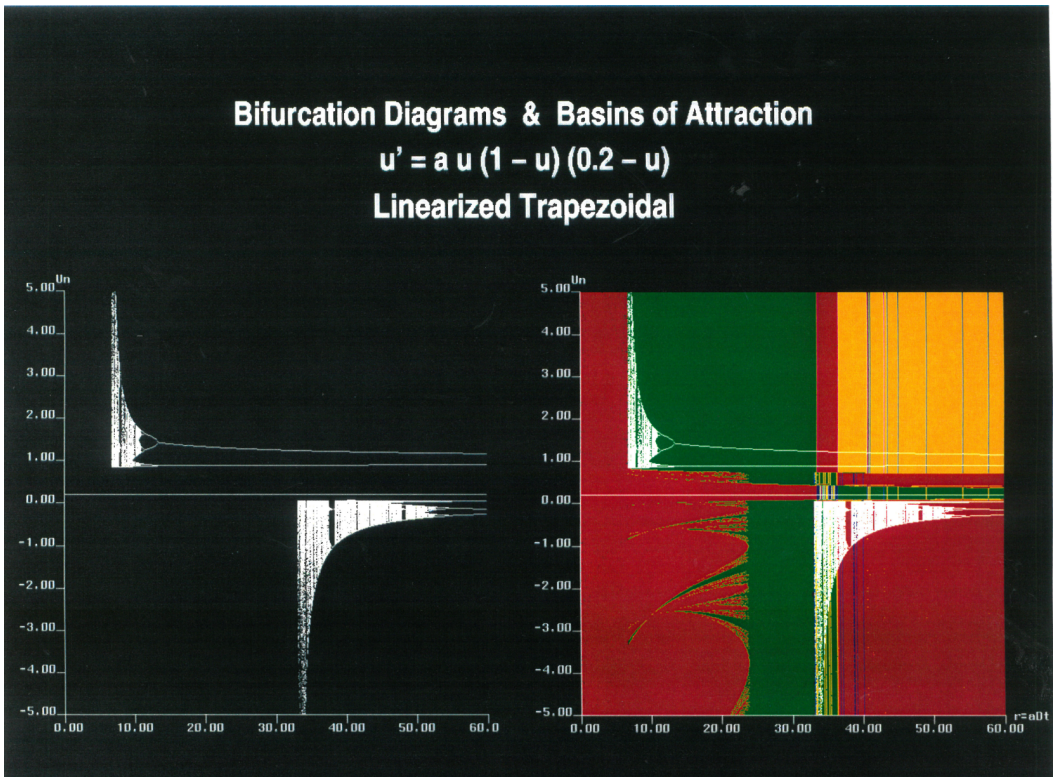

Figure 11. Full bifurcation diagram and basin of attraction for ODE (3) using linearized trapezoidal, $\alpha > 0$.

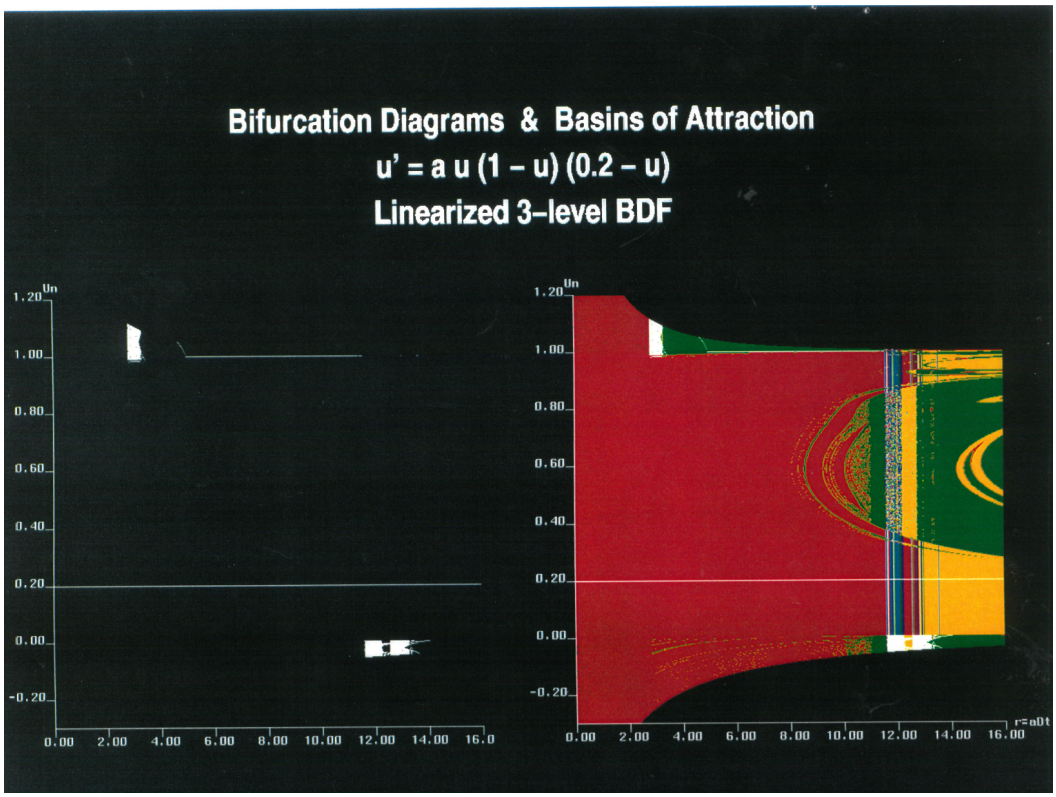

Figure 12. Full bifurcation diagram and basin of attraction for ODE (3) using linearized 3-level BDF, $\alpha > 0$.

It is interesting to note that the corresponding bifurcation diagrams of the respective discrete maps produced by the studied schemes consist of unions of "logistic-map-like" bifurcations and/or "inverted logistic-map-like" bifurcations with similar yet slightly complicated period-doubling cascades resulting in chaos. In all of the fixed point diagrams shown, the majority of the bifurcation phenomena can be divided into three kinds: flip, supercritical and transcritical bifurcations (Seydel [115]). The global asymptotic behavior of super-stable implicit LMMs indicates that unconditional stable LMMs can stabilize unstable physical steady states. From these illustrations, one can conclude that all of the studied explicit methods eventually undergo "period doubling bifurcations" leading to the "logistic-map-type bifurcations". The birth of the logistic-map-type bifurcations can occur below or beyond the linearized stability limit of the true steady state of the governing equation. Besides the regular logistic-map-type bifurcations, some of these methods undergo the so-called "inverted logistic-map-type" of period-doubling bifurcations. The above example explains the role of initial data in the generation of spurious steady-state numerical solutions, stable and unstable spurious numerical chaos and other asymptotes. Readers are referred to our work [1,66] for the forms of these studied ODE methods.

Although the basin of attraction for the stable fixed point u is the entire positive half-plan for all values of $\alpha > 0$ for the logistic ODE, the role of initial data in the occurrence of stabilizing unstable steady states of the governing equation and the introduction of stable and unstable spurious numerical chaos and other asymptotes by implicit LMMs are illustrated. See our previous papers [1,66,90] for more discussions.

It is noted that the computed bifurcation diagram cannot distinguish between the types of bifurcation and the periodicity of the spurious fixed points of any order. With the numerical basins of attraction and their respective bifurcation diagrams superimposed on the same plot, the type of bifurcation and the determination of which initial data lead to which stable asymptotes become apparent. In order to obtain the corresponding numerical basins of attraction for the schemes discussed above, one immediately realizes that, in most

cases, a numerical approach is the only recourse until more theoretical tools for searching for the basin boundaries of general discrete maps become available. We would like to add that there are isolated theories or approximate methods to locate some basin boundaries for simple discrete maps or special classes of discrete maps. Even in this case, these methods are neither practical nor are there fixed guidelines for the actual implementation of discrete maps for more complex ones of similar type. See early work by Hsu [116] for an approximate method and Friedman [117] for numerical algorithms that compute connecting orbits.

Local Error Control vs. Suppression of Spurious Numerics The previous sections discussed mainly the spurious behavior of long-time integrations of initial value problems of nonlinear ODE solvers for constant step sizes. The use of adaptive step size based on local error control for implicit methods was studied by Dieci and Estep [85]. Dieci and Estep concluded that for super-stable LMMs with local step size error control and depending on the procedure for solving the resulting nonlinear algebraic equations, spurious behavior can occur. Our preliminary study on the two variable step size control methods indicated that one shortcoming is that the size of Δt needed to avoid spurious dynamics is impractical (too small) to use, especially for needing more than one ODE method for error control. Theoretical studies on the adaptive explicit Runge–Kutta method for long-time integration have been gaining more attention. Early work by Stuart [39,88], Humphries [44], Higham and Stuart [118] and Aves et al. [82] showed that local error control offers benefits for long-term computations with certain problems and methods. Aves et al. addressed the heart of the question of whether local error control confers global properties of steady states of the IVP of autonomous ODEs using adaptive Runge–Kutta type methods. Aves et al.'s work is concerned with long-time behavior and global quantities of general explicit Runge–Kutta methods with step size control for autonomous ODEs. They studied spurious fixed points that persist for arbitrarily small error tolerances. This type of adaptive Runge–Kutta method usually consists of primary and secondary Runge–Kutta methods of different orders. Their main result is positive. When standard local error control is used, the chance of encountering spuriosity is extremely small. For general systems of ODEs, the constraints imposed by the error control criterion make spuriosity extremely unlikely. Recent development on this subject is beyond the scope of this overview paper.
Spurious Steady States and Nonphysical Wave Speeds: The possible connection of the numerical phenomenon of incorrect propagation speeds of discontinuities with the existence of some stable spurious steady states introduced by the spatial discretization was discussed in [1,2,8,25,42]. The topic will be discussed in more detail in Sections 6 and 9.

5. Adaptive Numerical Methods in Space and Time

Another important building block for PARs is adaptive numerical methods. This includes adaptive temporal and spatial schemes and grid adaptation as an integral part of the numerical solution process. For adaptive temporal discretization, it includes using more than one time integrator for error control and/or time step control, adaptive grid refinement (AMR) and, most of all, adaptive numerical dissipation controls by blending of more than one scheme based on smart flow sensors. Nearly three decades ago, using tools from dynamical systems, Yee et al. (1991–1997), Yee and Sweby (1993–1997), Griffiths et al. (1992a,b) and Lafon and Yee (1991, 1992) ([1,6,7,23,62,90]) showed that adaptive temporal and adaptive spatial schemes are important in minimizing numerically induced chaos, numerically induced chaotic transients and the false prediction of flow instability by direct numerical simulation (DNS). Their studies further indicated the need in the development of practical adaptive temporal schemes based on error controls to minimize spurious numerics due to the **full discretizations**. In addition, the development of adaptive temporal and spatial schemes based on error controls to minimize numerical artifacts due to the full discretizations is also needed. This is due to the fact that adaptive temporal or adaptive spatial schemes **alone** will not be able to provide an accurate and reliable process

to minimize numerical artifacts for time-accurate computations. Guided by the theory of nonlinear dynamics, Yee et al. [63] and Yee and Sweby [119] presented practical examples that illustrated the danger of using nonadaptive temporal and spatial schemes for studying flow instability.

Another important numerical method development is accurate, stable and reliable simulations of compressible turbulence with shock waves by adaptive numerical dissipation controls. It is well known that reliable, accurate and efficient direct numerical simulation (DNS) of turbulence in the presence of shock waves represents a significant challenge for numerical methods. Standard TVD, ENO, WENO and discontinuous Galerkin (DG) types of shock-capturing methods for the Euler equations has been routinely used for over three decades in high-speed blast wave simulations with virtually non-oscillatory, crisp resolution discontinuities. For the unaveraged unsteady compressible Navier–Stokes equations, it was observed that these schemes are still too dissipative for turbulence and transition predictions. On the other hand, hybrid schemes, where spectral and/or higher-order compact (Padé) schemes are switched to higher-order WENO or ENO schemes when shock waves are detected, have their deficiencies for complex turbulence and shock interaction. One shortcoming of this type of hybridization is that the numerical solution might experience a non-smooth transition at the switch to a different type of scheme. For 2D and 3D complex shock wave and shear surface interactions, the switch mechanism can become non-trivial and frequent activation of shock-capturing schemes is possible.

The early work of Yee et al. [26,63], Sjögreen and Yee [10,120], and Yee and Sjögreen [121,122] indicates that appropriate adaptive numerical dissipation control is essential to control nonlinear instability in general and particularly for long-time integration. A more recent integrated design approach on the construction of adaptive numerical dissipation controls can be found in Yee and Sjögreen [3] and the references cited therein. An earlier, excellent overview paper on hybrid methods for high-speed flows was presented by Pirozzoli in 2011 [123]. The nonlinear filter methods of Yee et al., which blended more than one method using a high-order entropy-conserving method [9,10,26–28], were not included in [123].

6. Numerical Source Term Treatments in Reacting Flows

We devote this section to source term treatments in reacting flows as there is a wide area of CFD, computational astrophysics and the next-generation spacecrafts and high-speed civil transport design applications. Examples of application areas are combustion, turbulence combustion, scramjet engine designs and black hole accretion. In the modeling of problems containing finite-rate chemistry or combustion, a wide range of space and time scales is often present due to the reacting terms, over and above the different scales associated with turbulent flows, leading to additional numerical difficulties. This stems mainly from the fact that the majority of widely used numerical algorithms in reacting flows were originally designed to solve non-reacting fluid flow problems. Fundamental studies on the behavior of these schemes for reacting model problems by the author and collaborators were reported in Yee and Sweby [119] and the references cited therein. In the majority of these studies, theories from dynamical systems were used to gain a better understanding of the nonlinear effects on the performance of these schemes. The main findings of this report and our recent development are as follows:

- It was shown in LeVeque and Yee [8] that, for stiff reactions containing shock waves, it is possible to obtain stable solutions that look reasonable and yet are completely wrong because the discontinuities are in the wrong locations. Stiff reaction waves move at nonphysical wave speeds, often at the rate of one grid cell per time step, regardless of their proper speed. There exist several methods that can overcome this difficulty for a single reaction term. For more than a single reaction term in fully coupled nonlinear systems, more research is needed. One impractical way of minimizing the wrong speed of propagation of discontinuities is to demand orders of magnitude grid size reduction compared with what appears to be a reasonable grid spacing in practice.

- It was shown in Lafon and Yee [6,7] that the numerical phenomenon of incorrect propagation speeds of discontinuities may be linked to the existence of some stable spurious steady-state numerical solutions.
- It was also shown in Lafon and Yee[6,7] that various ways of discretizing the reaction term can affect the stability and convergence of the spurious numerical steady states and/or the exact steady states. Pointwise evaluation of the source terms appears to be the least stable.
- It was shown in Yee et al. [23] and Griffiths et al. [35,124] that spurious discrete traveling waves can exist, depending on the method of discretizing the source term. When physical diffusion is added, it is not known what type of numerical difficulties will surface.
- Our later work with Chi-Wang Shu, Wei Wang and Dmitry V. Kotov [18–20,40–42] developed new methods to minimize spurious numerics for combustion and nonequilibrium reacting flows.

Reaction-Convection Model: Based on the work of [6–8,23,35,119], in addition to the incorrect propagation speed of discontinuities, other spurious numerics that are directly tied to the amount of numerical dissipation contained in the chosen scheme and the numerical treatment of source terms may result in possible spurious steady-state numerical solutions and spurious standing waves [6,7,23,35]. It was shown in Lafon and Yee [6,7] and in Griffiths et al. [35] that various ways of discretizing the nonlinear reaction terms can affect the stability of, and convergence to, the spurious numerical steady states and/or the exact steady states. Pointwise evaluation of the source terms appears to be the least stable. The studies of Lafon and Yee [6,7] indicated that numerical phenomena of incorrect propagation speeds of discontinuities may be linked to the existence of some stable spurious steady-state numerical solutions. More importantly, the different combination of time step, grid spacing and initial condition plays a major role in obtaining the correct solution. In addition, it was shown in Yee et al. [23] and Griffiths et al. [35] that spurious discrete traveling waves can exist, depending on the method of discretizing the source term.

The effect of spatial as well as time discretizations on the existence and stability of spurious steady-state solutions was illustrated with examples in LeVeque and Yee and in Lafon and Yee (1991, 1992) [6–8,18–20,40,42]. This phenomenon is due to the smearing of the discontinuity caused by the spatial discretization of the advection term. This introduces a nonequilibrium state into the calculation. Studies linking spurious numerical standing waves for a nonlinear reaction model by first- and second-order spatial and temporal discretizations can be found in Lafon and Yee [6,7] and in Griffiths, Stuart and Yee [2,35]. The possible wrong prediction of transition point Reynolds number by DNS due to spurious bifurcation that created a false transition point was discussed in [2]. Inaccuracy of the scheme or insufficient grid points might lead to possible spurious bifurcation as well as creating wrong propagation speed of discontinuities and smearing of turbulent fluctuations. See [2] for a discussion. For various project methods to minimize wrong propagation speed of discontinuities, see [125–128] and the references cited therein.

Section IX is devoted to illustrating selected test cases on spurious numerics related to problems with stiff source terms and our recent methods to minimize wrong computed solutions.

7. Spurious Numerics Relevant to Turbulent Flow Computations [1,2]

Four numerical examples that exhibit spurious numerics relevant to turbulent flow computations were illustrated together with other CFD examples and can be found in [1,2]. This section illustrates two examples: (a) Chaotic transients near the onset of turbulence in DNS of channel flow (Keefe 1992, Keefe and Yee 1997, [129,130]); (b) false flow transition simulation on a 2D incompressible flow over a backward-facing step as a function of Reynolds number. The numerical transition is due to a lack of grid refinement, not long enough time integration and/or lack of sufficient numerical dissipation for high-order methods. If care is not taken, spurious bifurcation of the discretized counterpart and/or a

numerically induced chaotic transient can be mistaken for the onset of physical turbulence of the governing equation. These simple examples are useful in modeling and simulations of turbulence combustion, supersonic turbulence, computational astrophysics and the next-generation spacecrafts and high-speed civil transport design. See Figure 13 for a schematic of the flow pattern of a scramjet engine. The figure source is from https://en.m.wikipedia.org/wiki/File:ScramjetDiagram.gif. This figure is in the public domain in the United States because it was solely created by NASA. See also Moura et al. [131] on the characterization of supersonic turbulent combustion in a Mach-10 scramjet combustor.

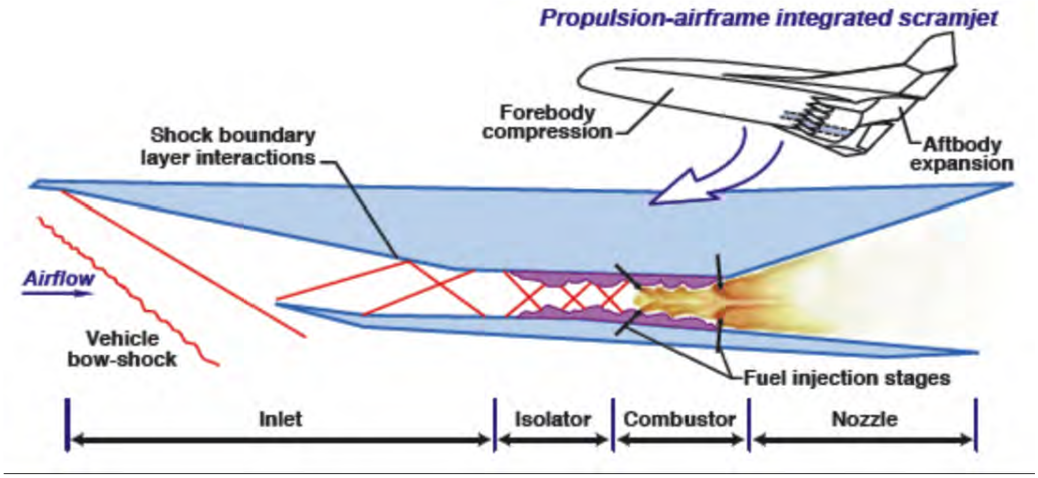

Figure 13. Schematic of flow pattern of a scramjet engine. Source: https://en.m.wikipedia.org/wiki/File:ScramjetDiagram.gif. This figure is in the public domain in the United States because it was solely created by NASA.

7.1. Chaotic Transients Near the Onset of Turbulence in Direct Numerical Simulations of Channel Flow (Keefe 1988, Keefe and Yee 1997 (Unpublished))

In addition to the inherent chaotic and chaotic transient behavior in some physical systems, numerics can independently introduce and suppress chaos as well as chaotic transients. Loosely speaking, a chaotic transient behaves like a chaotic solution ([132]). A chaotic transient can occur in a continuum or a discrete dynamical system. One of the major characteristics of a numerically induced chaotic transient is that if one does not integrate the discretized equations long enough, the numerical solution has all the characteristics of a chaotic solution. The required number of integration steps might be far beyond those found in standard CFD simulation practice before the numerical solution can get out of the chaotic transient mode. Furthermore, standard numerical methods, depending on the initial data, usually experience drastic reductions in step size and convergence rate near a bifurcation point of the continuum in addition to the bifurcation points due solely to the discretized parameters. See Yee and Sweby [1,62,90] for a discussion. Consequently, a possible numerically induced chaotic transient is especially worrisome in direct numerical simulations of the transition from laminar to turbulent flows. Except for special situations, it is extremely difficult to bracket closely the physical transition point by mere DNS of the Navier–Stokes equations. Even away from the transition point, this type of numerical simulation is already very CPU intensive and the convergence rate is usually rather slow. Due to limited computer resources, the numerical simulation can result in chaotic transients indistinguishable from sustained turbulence, yielding a spurious picture of the flow for a given Reynolds number. Consequently, it casts some doubt on the reliability of numerically predicted transition points and chaotic flows. It also influences the true connection between chaos and turbulence. See also Moore et al. [133].

Assuming a known physical bifurcation or transition point, Figure 14 illustrates the schematic of four possible spurious bifurcations due to constant time steps and constant

grid spacings. Different examples to illustrate the occurrence of these scenarios can be found in Sections 6.3 and 6.4 of our work [2]. Section 6.4 in [2] discusses the stability of the steady state (as a function of the Reynolds number) of a 2D backward-facing step problem using direct simulations. The present section is the computation by Laurence Keefe performed in the late 1980s. In 1996, we made use of the knowledge from continuum and discrete dynamical systems theory to interpret his result. We identified some of the aforementioned numerical uncertainties in his computations. The result is reported in [1].

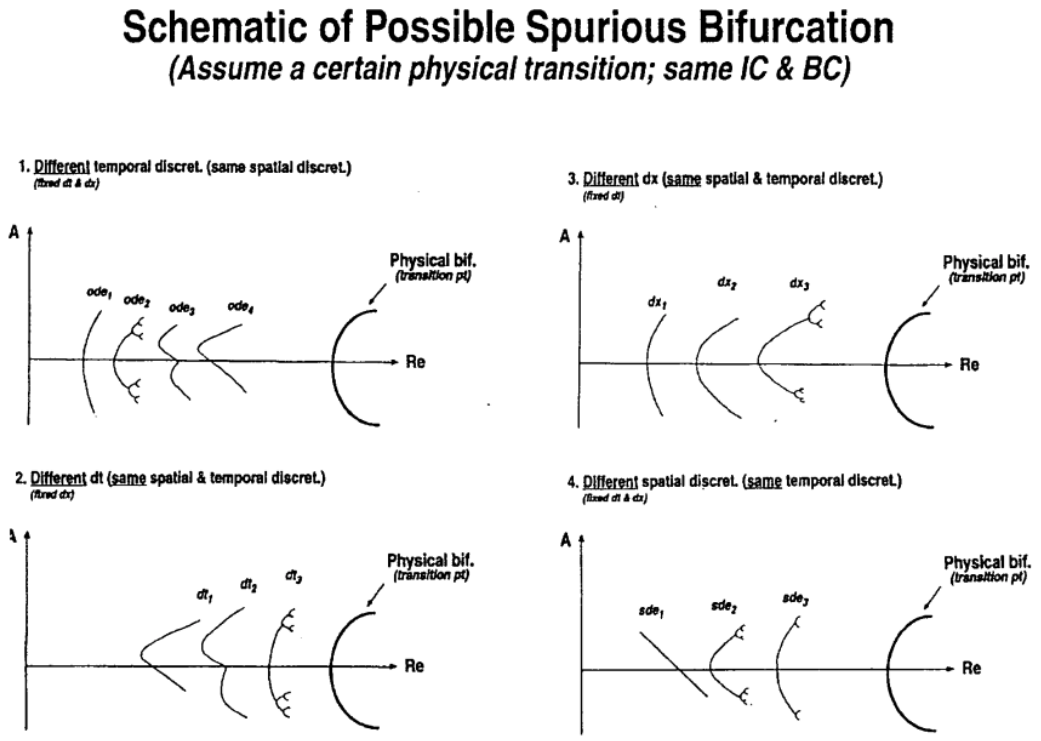

Figure 14. Schematic of possible spurious bifurcation for constant time steps and grid spacings. (**1**) Different temporal discretizations ode_1, ode_2, ode_3 and ode_4 (same spatial discretization and the same constant dt and dx). (**2**) Different constant time steps dt_1, dt_2, dt_3 and dt_4 (same temporal and spatial discretizations, and the same constant dx). (**3**) Different constant grid spacings dx_1, dx_2, dx_3 and dx_4 (same spatial and temporal discretizations, and the same constant dt). (**4**) Different spatial discretizations sde_1, sde_2 and sde_3 (same temporal discretization and the same constant dt).

The physical problem that Keefe considered is depicted in Figure 15, where a flow is confined between planes at $y = \pm 1$ and is driven in the x-direction by a mean pressure gradient dp/dx. The flow is characterized by a Reynolds number $Re = U_\infty L/\nu$, where U_∞ is the mean centerline velocity, L is the channel half-height and ν is the kinematic viscosity. Within the channel, the flow satisfies the incompressible Navier–Stokes equations and no-slip boundary conditions are applied at the walls. In the particular calculations shown here, these equations have been manipulated into velocity–vorticity form, where one integrates equations for the wall-normal velocity v and normal vorticity η, and recovers the other two velocity components from the incompressibility condition and the definition of η.

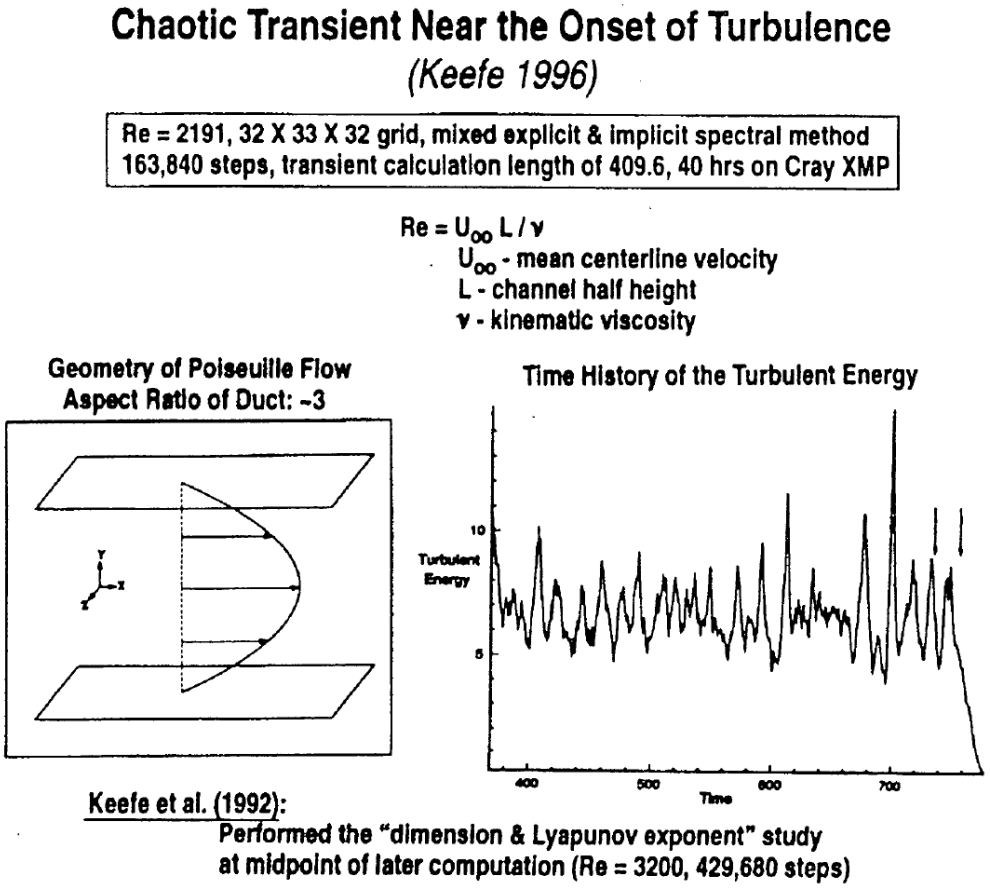

Figure 15. Three-dimensional channel flow computation by Keefe (1997) [130].

$$\frac{\partial}{\partial t}\Delta^2 v = h_v + \frac{1}{Re}\Delta^4 v, \tag{4}$$

$$\frac{\partial}{\partial t}\eta = h_g + \frac{1}{Re}\Delta^2 \eta, \tag{5}$$

$$f + \frac{\partial v}{\partial y} = 0, \tag{6}$$

where

$$f = \frac{\partial u}{\partial x} + \frac{\partial w}{\partial z}, \qquad \eta = \frac{\partial u}{\partial z} - \frac{\partial w}{\partial x}, \tag{7}$$

$$h_v = -\frac{\partial}{\partial y}\left(\frac{\partial H_1}{\partial x} + \frac{\partial H_3}{\partial z}\right) + \left(\frac{\partial^2}{\partial x^2} + \frac{\partial^2}{\partial z^2}\right) H_2, \tag{8}$$

$$h_g = \frac{\partial H_1}{\partial z} - \frac{\partial H_3}{\partial x}. \tag{9}$$

Here, the H_i contains the nonlinear terms in the primitive form of the Navier–Stokes equations and the mean pressure gradient.

The velocity increases extremely rapidly normal to the wall, and turbulent channel flows are essentially homogeneous in planes parallel to the wall. The first requires a concentration of grid points near the wall, and the second suggests use of a doubly periodic

domain in planes parallel to the wall. A spectral representation of the velocity field (u, v, w) is

$$\vec{u} = \sum_{l} \sum_{m} \sum_{n} \vec{A}_{lmn}(t) T_l(y) e^{im\alpha x + in\beta z}, \tag{10}$$

where the $T_l(y)$ are Chebyshev polynomials used for the spatial discretization. The numerical problem then becomes dependent on α and β in addition to Re. For the time discretization, mixed explicit–implicit methods are used. The nonlinear terms in the equations are advanced using second-order Adams–Bashforth or a low-storage, third-order Runge–Kutta scheme (Spalart et al. [134]), while the viscous terms are advanced by Crank–Nicholson.

One of the central problems in studies of wall-bounded shear flows is the determination of when a steady laminar flow becomes unstable and transitions to turbulence. In dynamical systems terms, the Navier–Stokes equations always have a fixed point solution for low enough Reynolds numbers; but for each flow geometry, the Reynolds number at which this fixed point bifurcates needs to be determined. In channel flow, the fixed point solution (a parabolic velocity profile across the channel, $u(y) = (1 - y^2)$) becomes linearly unstable at $Re = 5772$ (Orszag [135]). However, since turbulence appears in experiments at much lower Reynolds numbers, it was conjectured that this bifurcation must be subcritical. A subsequent numerical solution of the nonlinear stability equations (Herbert 1976, Ehrenstein and Koch 1991) [33,136] demonstrated this to be true, showing that limit cycle solutions with amplitude ϵ branch back to lower Reynolds numbers before subsequently passing through a turning point and curving back toward higher Reynolds numbers. Thus, for Reynolds numbers just above the turning point, the flow equations have at least four solutions: the fixed point, two unstable limit cycles and a chaotic solution (experimentally observed turbulence). Determining the location of the turning point in $(\alpha, \beta, \epsilon, Re)$ space is known as the minimum-critical-Reynolds-number problem, and its solution is by no means complete.

One way to investigate the turning point problem is to perform DNS of channel flow for conditions believed to be near this critical condition. Beginning with a known turbulent initial condition from higher Reynolds number, one integrates in time at the target Reynolds number to determine whether the flow decays back to the fixed point or sustains itself as turbulence. Although this may not be the most efficient way to bracket the turning point, it has the advantage that the peculiar dynamics of the flow near the turning point, whether in decay or sustained turbulence, are observable. This yields information about the path along which flows become turbulent at these low Reynolds numbers.

Unfortunately, the flow dynamics are very peculiar near the turning point, and extremely long chaotic transients are observed in the computations that make a fine determination of that point all but impossible by this method. This can be seen in Figure 15, where a time history of the turbulent energy in a channel flow (energy above that in the laminar flow) is plotted for a Reynolds number of 2191. To understand the time scale of the phenomenon, some experimental facts need to be recalled. In typical experimental investigations of channel flow, the infinite transverse and streamwise extent of the ideal flow are approximated by studying flow in high aspect ratio (10–40) rectangular ducts that are typically 50–100 duct heights long. If times are non-dimensionalized by the centerline mean velocity U_∞ and the duct half height L, then statistics on turbulence are gathered by averaging hot-wire data over intervals $\Delta t U_\infty / L \sim 200$. In the simulations and figure, the time scale is based on the friction velocity u_τ and L, where typically 15–20 $u_\tau \sim U_\infty$. Thus, averaging over intervals $\Delta t u_\tau / L \sim 10$ should and does yield stable flow statistics that compare well with experiments. The near-wall velocity profile, cross-channel turbulence intensities, and Reynolds and shear stress distribution for the $\Delta t u_\tau / L \sim 10$ interval near the end of the transient, delineated by the arrows in Figure 15, indicate the good comparison. In each case, they correspond well to available experimental data. However, consider the time scale of the transient; it spans $\Delta t u_\tau / L \sim 300$, thirty times longer than the time needed

to obtain stable statistics that would convince most experimentalists that they are viewing a fully developed turbulent channel flow. This is further complicated by the wide variation of the transient length, depending upon both the grid resolution (number of modes in the spectral representation) and the linearly stable time step of the integration. In fact, for fixed (α, β, Re), it is possible to obtain sustained turbulence for one time step but see it rapidly decay to laminar flow for another, lower value of the step.

Extended chaotic transients near bifurcation points are not an unknown phenomenon; the "meta-chaos" of the Lorenz system is but one of many known examples. However, the practicalities of numerical computation in fluid dynamics usually interfere with one's ability to discern whether transient, or sustained turbulence, is being calculated. The computations required to obtain the transient plot in Figure 15 needed 40 h of single processor time on a Cray XMP, some thirty years ago. Such a small amount of expended time was only possible because the spatial resolution of the calculation was relatively coarse ($32 \times 33 \times 32$), in keeping with the large scales of the phenomena expected at these flow conditions. Higher resolution calculations ($192 \times 129 \times 160$) (Kim et al. [137]) at greater Reynolds numbers typically have taken hundreds of hours ($\sim$250) to barely obtain the $\Delta t u_\tau / L = 10$ averaging interval that is so inadequate for detecting transients. Because such calculations are so time consuming, one typically chooses an integration time step that is a substantial fraction of the linear stability limit of the algorithm so as to maximize the calculated "flow time" for expended CPU time. However, it is clear from these transient results that this practice has some dangers when close to critical points of the underlying continuous dynamical system. Thus, it appears that just as pseudo-time integration to obtain steady solutions can result in spurious results, genuine time integration can result in chaotic transients indistinguishable from sustained turbulence and yield a spurious picture of the flow for a given Reynolds number.

7.2. Temporal and Spatial Refinement Studies of 2D Incompressible Flow over a Backward-Facing Step

The 2D incompressible flow over a backward-facing step has been addressed by many authors using a wide variety of numerical methods. Figure 16 shows the flow geometry. Fluid with constant density ρ and viscosity μ enters the upstream channel of height h with a prescribed velocity profile (usually parabolic). After traveling a distance l, the fluid passes over a backward-facing step of height s and enters the downstream channel of height $H = h + s$. After traveling a distance L downstream of the step, the fluid exits the region of interest. For Reynolds numbers considered here, the flow separates at the corner and forms a recirculating region behind the step. Additional recirculating regions form on the upper and, subsequently, lower walls of the downstream channel as the Reynolds number is increased.

Results of sustained unsteady flow from various numerical simulations have been reported for Reynolds numbers (Re) ranging from 250 up to 2500. The formulations included the vortex method, unsteady equations in stream function form, steady equations and the associated linear-stability problem, and the unsteady equations in primitive variable form. The numerical methods used cover almost all of the existing schemes in the literature. The majority of the numerical results are summarized in Gresho et al. [138]. The work of Gresho et al. was an answer to a controversy concerning the stability of the stationary solution at $Re = 800$. It was concluded by Kaiktsis et al. [139] computed by a high-order spectral element method that transition to turbulent flow has occurred at $Re = 800$. See [139] for the description of the numerical method. Kaiktsis et al. examined the long-time temporal behavior of the flow and found that the flow is steady at $Re = 500$, time-periodic at $Re = 700$ and chaotic at $Re = 800$. Gresho et al. conducted a detailed grid refinement study using four different numerical methods and concluded that the backward-facing step at $Re = 800$ is a stable steady flow.

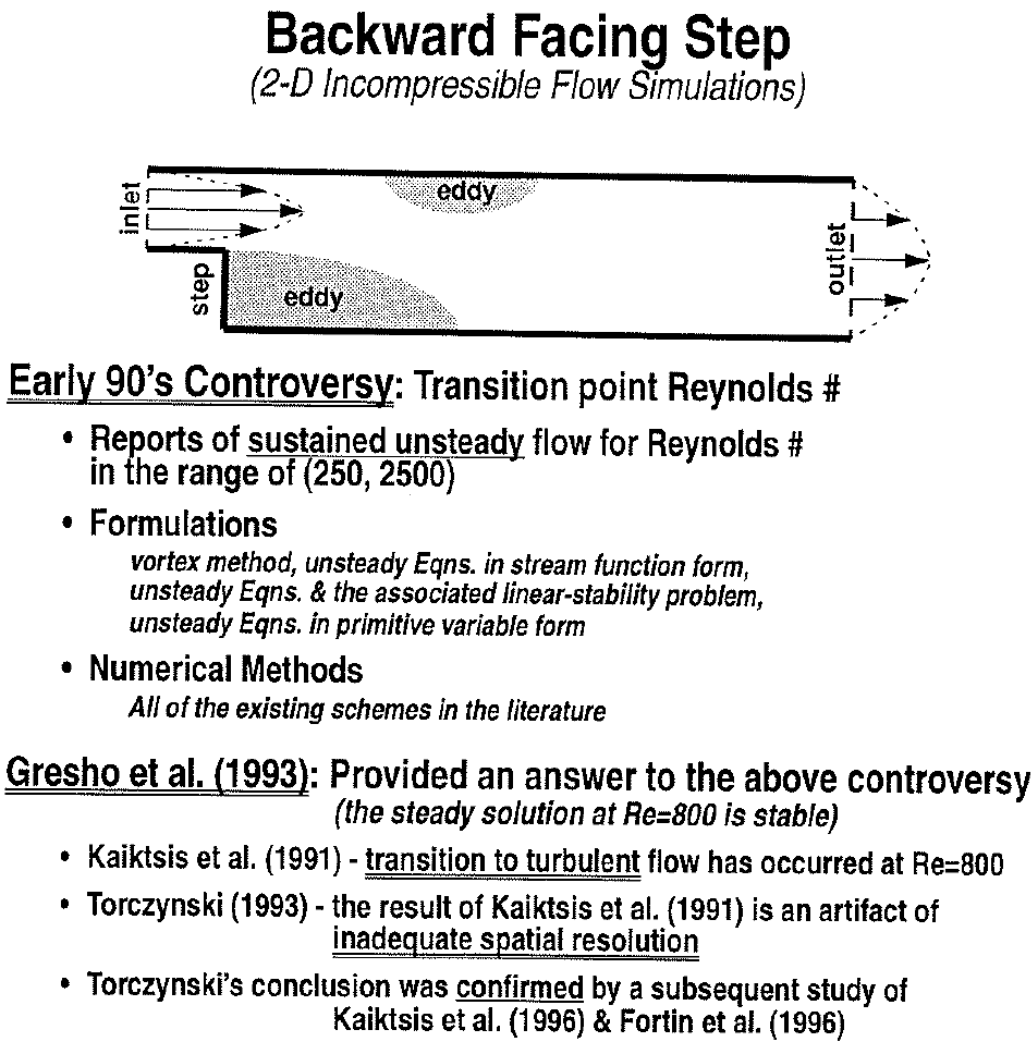

Figure 16. Schematic of the backward-facing step problem.

In addition to the study of Gresho et al., an extensive grid refinement study of this flow using a spectral element method was conducted in Torczynski [140]. The simulated geometry and the numerical method correspond to those of Kaiktsis et al. Flow was examined at Reynolds numbers of 500 and 800. His systematic grid refinement study was performed by varying both the element size and the order of the polynomial representation within the elements. For both Reynolds number values with the transient computations stopped at $t = 800$, it was observed that low-resolution grid cases exhibit chaotic-like temporal behavior whereas high-resolution grid cases evolve toward asymptotically steady flow by a monotonic decay of the transient. The resolution required to obtain asymptotically steady behavior is seen to increase with Reynolds number. These results suggest that the reported transition to sustained chaotic flow by Kaiktsis et al. at Reynolds numbers around 700 is an artifact of inadequate spatial resolution. Torczynski's conclusion was further confirmed by a subsequent study of Kaiktsis et al. [141] and Fortin et al. [110]. Fortin et al. employed tools from dynamical systems theory to search for the Hopf bifurcation point (transition point). They showed that the flow remains steady at least up to $Re = 1600$.

7.2.1. Grid Refinement Study of Torczynski (1993) [140]

In Torczynski (1993) [140], $Re = \rho\overline{u}2h/\mu$ is based on upstream conditions. The variable $\overline{u}$ is the spatial average of the horizontal velocity u over h. The geometry is

specified to match that of Kaiktsis et al. [139]. The upstream channel height h and step height s have values of $h = 1$ and $s = 0.94231$, yielding a downstream channel height of $H = 1.94231$. The corner of the step is at $(x, y) = (1, 0)$. The channel extends a distance $L = 1$ upstream from the step and a distance $L = 34$ downstream from the step to preclude undue influence of the finite channel length on the flow at $Re = 800$. The following conditions are applied on the boundaries of the computational domain: $u = v = 0$ on the upper and lower channel walls, $-p + \mu\partial u/\partial n = 0$ and $\partial v/\partial n = 0$ on the outflow boundary, and $u = [\tanh(t/16)]u_B(y) + [1 - \tanh(t/16)]u_P(y)$ and $v = 0$ on the inflow boundary and the step surface. Here, $u_B(y) = max[0, 3y(1 - y)]$ is the correct boundary condition for flow over a backward-facing step and $u_P(y) = 3(1 - y)(s + y)/(1 + s)^3$ is the Poiseuille flow observed infinitely far downstream whenever steady flow is asymptotically obtained. The initial velocity field is set equal to $u = u_P(y)$ and $v = 0$ throughout the domain. Here, v is the vertical velocity and p is the pressure. Thus, the above combination of boundary and initial conditions initially allows flow through the step surface so that the simulations can be initialized using an exact divergence-free solution of the Navier–Stokes equations. Furthermore, since the inflow boundary condition is varied smoothly in time from Poiseuille flow to flow over a backward-facing step, the flow experiences an order-unity transient that is probably strong enough to excite sustained unsteady behavior, if that is the appropriate asymptotic state for the numerical solution.

The simulations were performed using the commercial code NEKTON v2.8, which employs a time-accurate spectral-element method with the Uzawa formulation (NEKTON, 1991). Let D be the dimensionality. Each element has N^D velocity nodes located at Gauss–Lobatto–Legendre collocation points, some of which are on the element boundaries, and $(N - 2)^D$ pressure nodes located at Gauss–Legendre collocation points, all of which are internal. Within each element, the velocity components and the pressure are represented by sums of D-dimensional products of Lagrangian-interpolant polynomials based on nodal values. This representation results in continuous velocity components but discontinuous pressure at element boundaries. Henceforth, the quantity N is referred to as the element order, even though the order of the polynomials used to represent the velocity is $N - 1$. NEKTON employs mixed explicit and implicit temporal discretizations. To avoid solving a nonlinear, nonsymmetric system of equations at each time step, the convective term is advanced explicitly in time using a third-order Adams–Bashforth scheme. All other terms are treated implicitly (implicit Euler for the pressure and for the viscous terms).

In our further investigation [63], Torczynski and the first author used three spectral-element grids of differing resolution, denoted L (low), M (medium) and H (high). Detailed investigation can be found in [2,63]. Here, we include selected results of those studies. Figure 17 shows the computational domain and the grid distribution of the three spectral element grids in which the **distribution of nodes within each spectral element is not shown**. The L grid with $N = 9$ is identical to the grid of Kaiktsis et al. (1991) [139]. Four general classes of behavior are observed for the numerical solutions. First, "steady monotonic" denotes evolution of the numerical solution toward an asymptotically steady state. Second, "steady oscillatory" denotes evolution toward an asymptotically steady state with a decaying oscillation superimposed on the monotonic decay. Third, "unsteady chaotic" denotes irregular transient behavior of the numerical solution that shows no indication of evolving toward steady behavior. Fourth, "diverge" denotes a numerical solution terminated by a floating-point exception. In Figure 17, the first character denotes the grid resolution L, M or H; the first digit indicates the Reynolds number 500 or 800; and the last two digits indicate the order of the spectral element being used. For example, $L807$ means $Re = 800$ using the L grid with $N = 7$.

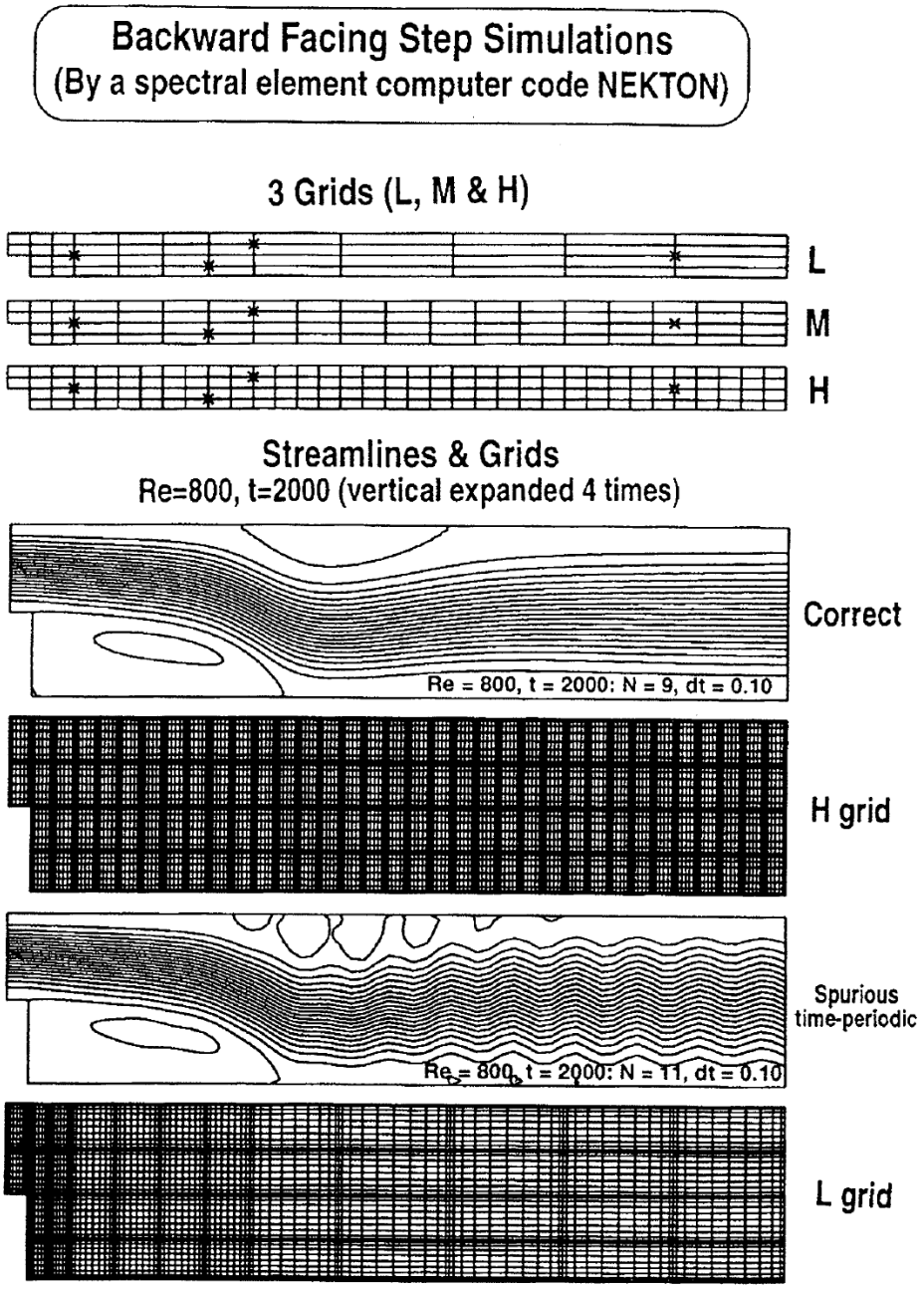

Figure 17. Three different grids, and streamlines of $H809$ and $L811$ and their corresponding grids, by the spectral element method.

Our extensive grid refinement study resulted in grid-independent steady-state numerical solutions for both $Re = 500$ and $Re = 800$. As the grid resolution is reduced below the level required to obtain grid independent solutions, chaotic-like temporal behavior occurred. The degree of grid resolution required to obtain a grid-independent solution was observed to increase as the Reynolds number is increased. Figure 17 shows the streamlines for $H809$ (steady solution) and $L811$ (spurious time-periodic solution) and the corresponding grids with the distribution of the nodes of the spectral elements shown.

7.2.2. Temporal Refinement Studies Using Knowledge from Dynamical Systems Theory

All of Torczynski's numerical solutions integrate to $t = 800$. With the knowledge of possible nonlinear behavior of numerical schemes such as long-time transients before a

steady state is reached; numerically induced chaotic transients; numerically induced or suppressed chaos; existence of spurious steady states and asymptotes; and the intimate relationship among initial data, time step and grid spacing observed in discrete dynamical systems theory, Yee et al. [63] examined the Torczynski cases in more detail.

In the Yee et al. (1997) study ([2,63]), in addition to grid refinement, temporal refinements are made on all of the under-resolved grid cases to determine if these cases sustain the same temporal behavior at a much later time or evolve into a different type of spurious behavior. At $t = 800$, cases $L506$, $L507$, $L508$, $L509$, $L811$, $M807$ and $M808$ either exhibit "unsteady chaotic" or "steady oscillatory" behavior. We integrate these cases to $t = 2000$ to determine if a change in solution behavior occurs. From the phenomena observed in Keefe's 3D channel flow computation and others, $t = 2000$ might not be long enough for a long-time transient or long chaotic transient to die out. There is also the potential of evolving into a different type of spurious or divergent behavior at a much later time. However, for this study, it appears that $t = 2000$ is sufficient. For $Re = 500$, we also recomputed some of these cases with a sequence of Δt that bracketed the benchmark study of Torczynski. The Δt values are $0.02, 0.05, 0.10, 0.125, 0.2, 0.3, 0.4$ and 0.5 for $Re = 500$. The CFL number for all of these cases is above 1 for $\Delta t > 0.10$. The reason for the investigation of $\Delta t = 0.3, 0.4$ and 0.5 is to find out, after the transients have died out, if the solution converges to the correct steady state for Δt that are a few times larger than 0.10.

For $Re = 800$, we integrate $L811$ and $M808$ with $\Delta t = 0.10$ and $M807$ with $\Delta t = 0.02, 0.05$ and 0.10 to $t = 2000$. Aside from integrating to $t = 2000$, five different initial data were examined for cases $M807$, $M809$ and $M811$ for $\Delta t = 0.10$ to determine the influence of the initial data and the grid resolution on the final numerical solution. The five initial data are as follows:

- Uniform: $u, v = 0$;
- Shear layer: $u = u_B(y) = max[0, 3y(1-y)], v = 0$;
- Solution from solving the steady Stokes equation (with no convection terms);
- Torczynski (1993) [140]: $u = u_P(y) = 3(1-y)(s+y)/(1+s)^3, v = 0$;
- Channel flow both upstream and downstream of step: Same as previous initial data except the boundary conditions.

The boundary conditions for the first three and last initial condition were parabolic inflow and no-slip at walls, whereas the boundary conditions for the fourth initial condition were those of Torczynski [140]:

$$u = [\tanh(t/16)]u_B(y) + [1 - \tanh(t/16)]u_P(y);\ v = 0.$$

The CPU time required to run the above cases ranged from less than a day to several days on a Sparc Center 2000 using one processor.

The chaotic-like behavior evolves into a time-periodic solution beyond $t = 800$ for $L506$ and $L507$, whereas the chaotic-like behavior evolves into a time-periodic solution beyond $t = 800$ for $L811$ and a divergent solution for $M807$. The "steady oscillatory" case $L508$ slowly evolves to the correct steady state with an amplitude of oscillation of 10^{-5}. The oscillation is not detectable within the plotting accuracy. The "steady oscillatory" time evolution of $M808$ is similar to that of $L508$. The numerical solutions with "steady oscillatory" and "steady monotonic" behavior at early stages of the time integration are almost identical at later stages of the time integration. They all converge to the correct steady state. The initial data study at $Re = 800$ with $\Delta t = 0.10$ is summarized in Table 5.5 of Yee et al. [63], which illustrates the intimate relationship between initial data and grid resolution.

Figure 18 shows the vertical velocity time histories at $(x, y) = (30, 0)$ advanced to a time of $t = 2000$ for $M807$ with $\Delta t = 0.02, 0.05$ and 0.10, and for $L811$ with $\Delta t = 0.10$. Case $M807$ diverges at $t = 1909.2$ with $\Delta t = 0.02$, at $t = 972.4$ with $\Delta t = 0.05$ and at $t = 827.77$ with $\Delta t = 0.10$. The time histories for these three time steps appear to show chaotic-like behavior if one stops the computations at $t = 800$. The bottom plot of Figure 18

shows the vertical velocity time histories advanced to a time of $t = 2000$ for $L811$ with $\Delta t = 0.10$. It shows the definite time-periodic spurious solution pattern. On the other hand, the time history for this case appears to show an aperiodic-like pattern if one stops the computation at $t = 800$. Note that the $L809$ grid case was used by Kaiktsis et al. [139], and they concluded that "2-D transition" has already occurred at $Re = 800$.

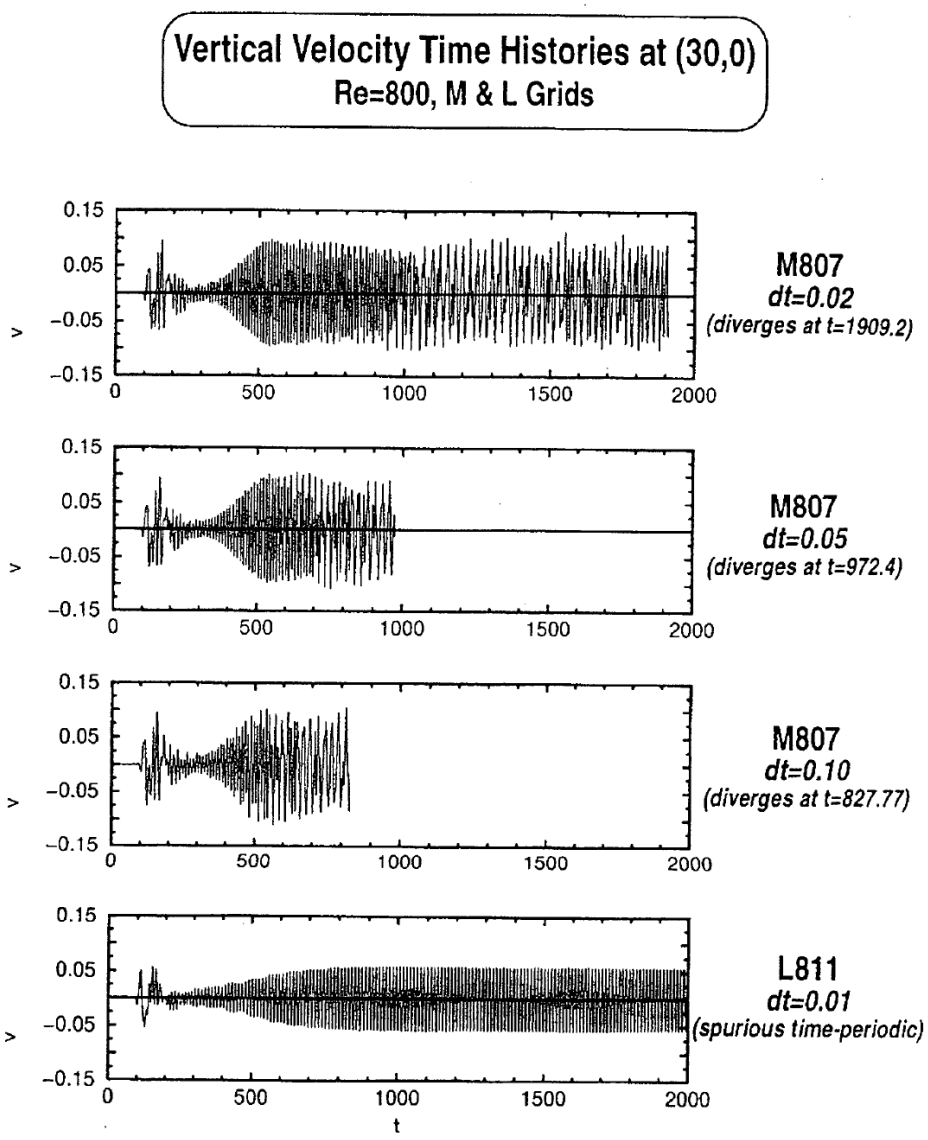

Figure 18. Vertical velocity time histories for $M807$ with time steps $0.02, 0.05, 0.10$ and $L811$ with time step 0.01 for $t = 2000$.

In summary, without the temporal refinement study (longer time integration), the $L506$, $L507$, $L811$ and $M807$ cases can be mistaken to be chaotic-like (or aperiodic-like) flow. Although the time history up to $t = 800$ appears chaotic-like, one cannot conclude it is chaotic without longer transient computations. One can conclude that with transient computations that are 2.5 times longer than Torczynski's original computations, what appeared to be aperiodic-like or chaotic-like behavior at earlier times evolved toward either a time-periodic or divergent solution at later times. These temporal behaviors appear to be long-time aperiodic-like transients or numerically induced chaotic-like transients. For $Re = 800$, five different initial data were examined to determine if the flow exhibits strong dependence on initial data and grid resolution. Results showed that the numerical solutions are sensitive to these five initial data. Note that the results presented pertain

to the characteristic of the studied scheme and the direct simulations. However, if one is certain that $Re = 800$ is a stable steady flow, a non-time-accurate method such as time-marching to obtaining the steady-state numerical solution would be a more efficient numerical procedure.

7.2.3. Spurious Bifurcation by Different Time Integrators (Henderson and Yee 1998, Unpublished)

This was a joint work with Ronald Henderson in 1998. The unpublished work was presented at the 10th International Conference in Finite Element Methods, 5–8 January 1998, Tucson, Arizona, and has also been presented at various invited lectures during the last four years. Our joint work illustrates the situation where solving the nonlinear terms of the Navier–Stokes equations by two different explicit time integrators (same implicit time integrator for the linear terms) results in spurious bifurcation. This spurious bifurcation is shown in Figure 19 as a function of the Reynolds number. These computations use the implicit Euler time integrator for the linear terms. Also, the same spatial discretization $L809$ is used with a fixed time step of $t = 0.10$. The two explicit time integrators are the third-order Adams–Bashforth (AB3) and a second-order explicit stiffly stable method (SS2) (Henderson [142]). The AB3 method experiences a spurious bifurcation near $Re = 720$, whereas the SS2 method experiences a spurious bifurcation at a larger Reynolds number near $Re = 800$. The method and the scaling for this figure can be found in Henderson [142]. Finding the exact location of these spurious bifurcation points requires more complicated computation, which is not performed here. In addition, the exact representation of this bifurcation plot is rather complicated to explain and is not important for the current discussion as it is not the main illustration for this study. When an adaptive version of the spectral element method (Henderson [142]) is used, the problem remains laminar up to $Re = 1800$. Future work, which is indicated in Figure 19, is planned, but the case has not been revisited thus far.

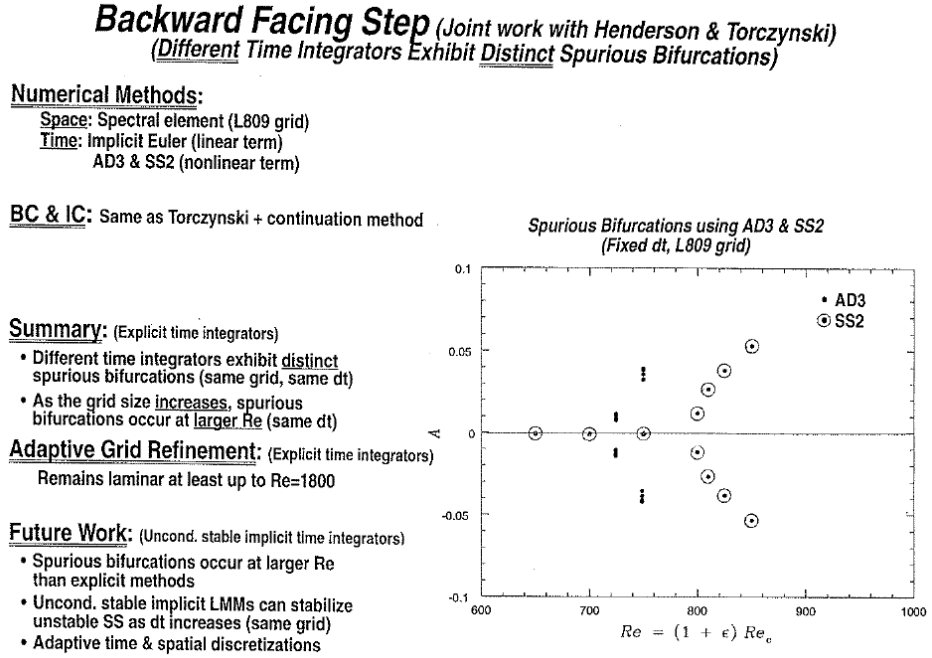

Figure 19. Different explicit time integrators (for the nonlinear terms of the Navier–Stokes equations) exhibit distinct spurious bifurcation using the same spatial discretization $L809$ and a time step of 0.10.

7.2.4. Minimization of Spurious Bifurcation by a Suitable Filter (Fischer 2001, Unpublished)

A few year later, Fischer (2001) [143] computed the same $L811$ spectral element grid using a time integrator based on the operator integration-factor splitting (OIFS) method

developed by Maday, Patera and Rønquist [144]. This scheme decouples the convective step from the Stokes update, thereby allowing CFL numbers in excess of unity. At the end of each step, Fischer applies a filter to the velocity that effectively scales the Nth-order Legendre modes within each element by $(1 - \alpha)$, where, typically, $0.05 \leq \alpha \leq 0.30$ (Fischer and Mullen [143]. Because the filter is applied on each step, its strength is a function of Δt as well as α. The spurious behavior observed by Kaiktsis et al. [139] is cured by the filter, and a stable steady-state numerical solution is obtained without further grid refinement. Figure 20 illustrates the velocity time histories at $(30, 0)$ by the filtered and unfiltered spectral element methods with $\Delta t = 0.10$.

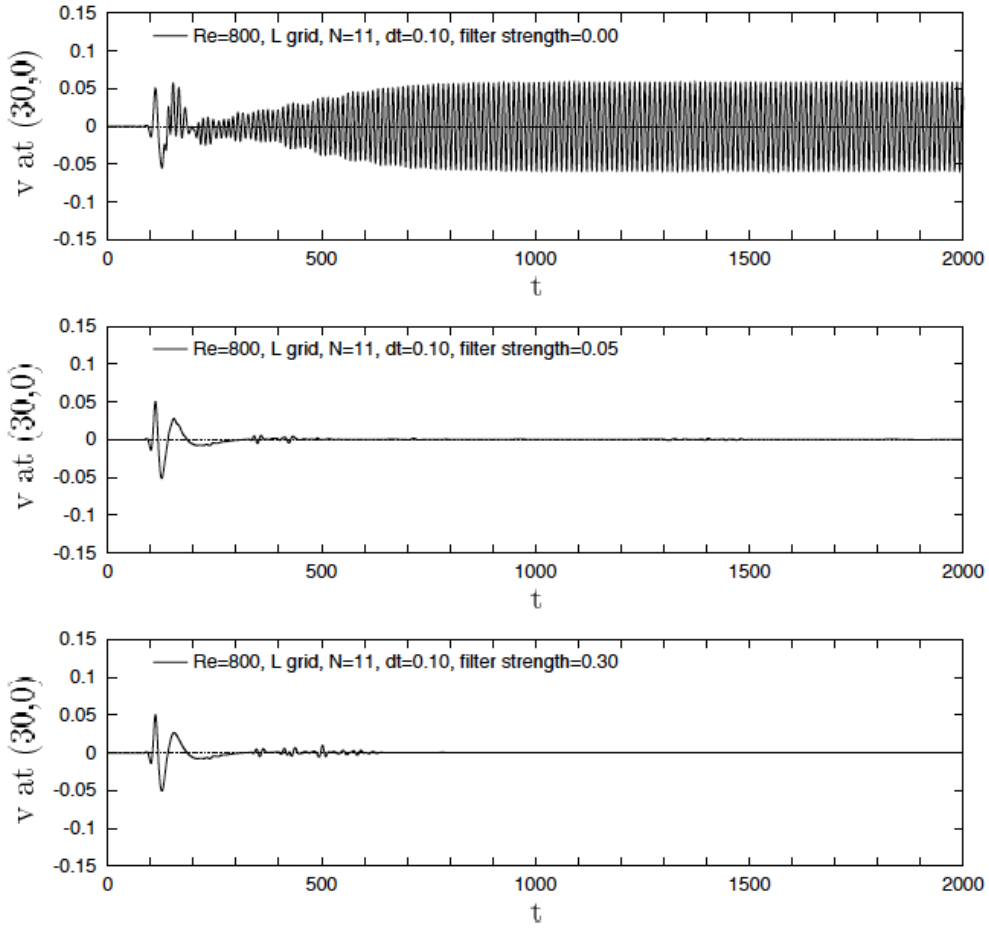

Figure 20. Comparison of the filtered with the unfiltered solutions of $L811$ with time step $dt = 0.10$. (**Top**) no filter; (**Middle**) filter (filter strength 0.05); (**Bottom**) filter (filter strength 0.3).

In summary, the above test cases illustrate all of the possible scenarios of spurious bifurcations indicated on the schematic bifurcation diagram as a function of Reynolds number by different temporal and spatial discretizations. See Gresho et al. [138] and the references cited therein for some more examples.

8. Entropy-Violating Numerical Methods and Nonlinearity-Induced Spurious Numerics by Shock-Capturing Methods

Among other spurious numerics discussed earlier, here, we would like to concentrate on the topic of "the carbuncle effect and hypersonic blunt body CFD simulations". Aside from issues in employing entropy-violating numerical methods in 1D and multi-D flows, there are added complications for the computation of external flow involving dimension-by-dimension numerical approaches on high-speed blunt body simulations. The topic has attracted numerical method developers for forty years, even before the term "carbuncle"

phenomena was born. Since the mid 1990s until the present time, there have been many explanations and proposed similar cures in the open literature. See, e.g., these later published works [43,48,49,51,52].

Below, we summarize our earlier work in the late 1980s with extensive numerical studies using our multi-D entropy fixes and other cures associated with this issue. Our key work related to this topic can be found in [21,22,47]. Since the 1983 Harten and Hyman entropy fixed by entropy violating methods [145], we have been using the various form of entropy fixes since 1983 and continuing to the present time, including high-order ENO, WENO and variants of ENO and WENO schemes. Our cure exhibits no grid-aligned shock instability issue for the hypersonic blunt body simulation for both time-marching to steady states or unsteady flows, including moving impinging shock of Types I–VI relating to the Edney experiment [146].

8.1. Avoidance of Spurious Numerics, and Enhancement of Stability and Convergence Rate for Hypersonic Flows Simulations

In [21,22,53], some elements and parameters that can affect the stability and convergence rate in high Mach number cases but have a negligible effect in low Mach number cases for steady-state inviscid blunt-body flows were identified. The current study indicated that the same elements and parameters can affect the stability and convergence rate at hypersonic speeds for viscous computations as well. They are as follows: (1) the choice of the entropy correction parameter δ_1 for non-entropy conserving methods, (2) the choice of the dependent variables on which the limiters are applied (related to proper scaling of the eigenvectors for high-speed flows) and (3) the prevention of nonphysical solutions during the initial transient stage. Our study indicated that these elements can also improve the stability of unsteady as well as steady hypersonic flows. Here, we use the same notation as in [21,22] for the TVD and MUSCL schemes entropy fix parameter. Their finding by the TVD and MUSCL schemes using Roe's approximate Riemann solver and implicit LMM time discretization are discussed as follows. It is remarked that for all of our later computations using high-order ENO and WENO methods, an analog entropy fix is needed if the local Lax–Friedrich flux formulation is used.

1. For Mach numbers ranging from 1.2 to 15, numerical experiments for one and higher dimensional unsteady flows containing unsteady shocks show that the second-order explicit TVD schemes are insensitive to the entropy correction for $0 \leq \delta_1 \leq 0.1$. In most cases, $\delta_1 = 0$ was used. For $0.1 \leq \delta_1 \leq 0.25$, there is a possibility of improving stability in the sense of allowing a higher CFL number at the expense of a slight smearing of the discontinuities. However, for unsteady complex shock wave interactions, a small positive δ_1 or a variable δ_1 can help stabilize the time-accurate implicit algorithm.

For subsonic to low supersonic steady-state NACA 0012 airfoil computations, the resolution of the shock waves was found to be quite insensitive to $0.1 \leq \delta_1 \leq 0.25$ and a constant value seems to be sufficient. However, for hypersonic flows, especially for blunt-body flows, a constant δ_1 or a variable δ suggested by Harten and Hyman [145] was found to be insufficient, but a variable δ_1 depending on the spectral radius of the Jacobian matrices of the fluxes is very helpful in terms of stability and convergence rate. For multi-D, a multi-D entropy fix is needed. In fact, a proper choice of the entropy parameter δ_1 for higher Mach number flows not only helps in preventing nonphysical solutions but can act as a control of the convergence rate and of the sharpness of shocks and slip surfaces (or shear layer in viscous flows). The smaller the δ_1 that is used, the slower the convergence rate. The larger the $\delta_1 \leq 1$ that is used, the larger the numerical dissipation being added. For the present blunt-body steady-state calculations with Mach numbers $M > 4$, the initial flow conditions at the wall are obtained using the known wall temperature in conjunction with pressures computed from a modified Newtonian expression. Also, for implicit methods, a slow start-up procedure from initial conditions is necessary. See [21,22] for additional details.

2. Higher order TVD-type schemes in general involve limiter functions. However, there are options in choosing the types of dependent variables when applying limiters for systems

of hyperbolic conservation law, particularly for systems in generalized coordinates. The choice of the dependent variables on which limiters are applied can affect the stability and convergence process. Due to the non-uniqueness of the eigenvectors, the choice of the characteristic variables on which the limiters are applied play an important role in the stability and convergence rate as the Mach number increases. For example, the path to arrive to the steady states might get trapped into a spurious limit cycle or spurious oscillations. This is directly related to proper scaling of the eigenvectors for high-speed flows. For low and moderate Mach numbers, the different choices of the eigenvectors have less effect on the stability and convergence rate. However, for large Mach number cases, the magnitudes of all the variables at the jump of the bow shock are not the same. In general, the jumps are much larger for the pressures than for the densities or total energy. Studies have indicated that employing the form of the eigenvectors such that the variation of the jump of the characteristic variables in transformed coordinates are of the same order of magnitude as the jump in the pressure would be a good choice for hypersonic flows.

3. The entropy fix for multi-D case for curvilinear grids should use the transformed variables, and the entropy variable parameter should include all dimensions' effects. All of our simulations for blunt body hypersonic simulations [21,22] use the multi-D entropy fix in the transformed variables.

4. A less known property of Roe's average state is that it allows the square of the average sound speed $c^2{}_{j+1/2}$ to lie outside the interval between $c^2{}_j$ and $c^2{}_{j+1}$ for equilibrium real gases. Roe's average state $c_{j+1/2}$ might be negative even though c_j and c_{j+1} are positive during the transient stage when the initial conditions are far from the steady-state physical solution. In this case, we replace $c^2{}_{j+1/2}$ by $\max\left(c^2{}_{j+1/2}, \min\left(c^2{}_j, c^2{}_{j+1}\right)\right)$. This latter safety check is particularly helpful for the symmetric TVD algorithm but not necessary for the upwind algorithm. Here, $c^2{}_{j+1/2}$ is the square of the sound speed evaluated at Roe's average state. In addition, due to the large gradients and to the fact that the initial conditions are far from the steady-state physical solution, the path used by the implicit method can go through states with negative pressures if a large time step is employed. A convenient way to overcome this difficulty is to fix a minimum non-negative allowed value for the density and the pressure. With this safety check, the scheme allows a much larger time step and converges several times faster.

Choice of Limiters: Unlike flows with transonic and low supersonic shock waves, problems containing strong hypersonic shock waves are more sensitive to the treatment of limiters. Using the more diffusive limiter turns out to be more stable than other more compressive limiters. The more compressive limiters have a very low stability and slow convergence rate for steady flows. The same conclusion applies for unsteady flows where the more compressive limiters have a very restricted time step limit. Using a different limiter that is more appropriate for different linear and nonlinear characteristic fields would help. See [21,22] for more details. For over four decades, different designs of flux limiters to improve the time-marching to the steady states have been ongoing; see, e.g., two recent works [94,95,147].

Below, hypersonic blunt body simulations from [21,22] have been selected to illustrate our work in the 1980s to avoid spurious numerics and to enhance stability and convergence rates for hypersonic blunt body simulations. In [21,22], many types of blunt body test cases were conducted and all types of Edney shock-impingement on the blunt body [146] were considered. They include inviscid, perfect and real gas, non-interfering blunt-body steady and unsteady flows. In addition, test cases also include steady and unsteady inviscid, perfect gas blunt-body flow with an impinging shock.

8.2. Inviscid Blunt Body Steady Computations for a Real Gas

The freestream conditions for the current illustration are $M_\infty = 25$, $p_\infty = 1.22 \times 10^3$ N/m^2, $\rho_\infty = 1.88 \times 10^{-2}$ kg/m^3 and $T_\infty = 226$ K. Figure 21 shows half of the 61×33 grid used for the blunt-body problem. The shock standoff distance is at approximately 14

points from the wall on the symmetry axis. See [21,22] for details of the numerical method and simulations.

Figure 22 shows the Mach number, density, pressure and κ contours for Mach number $M_\infty = 25$. Here, $\kappa = (\partial p/\partial \overline{\epsilon})_\rho$, where $\overline{\epsilon} = \rho\epsilon$ and ϵ is the specific internal energy.

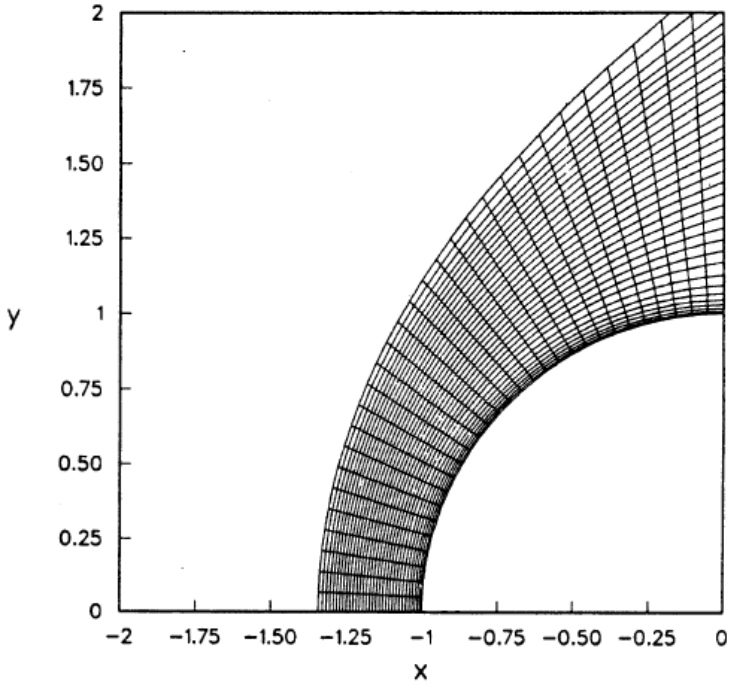

Figure 21. Blunt body grid: 31 × 33 grid points.

8.3. Inviscid Blunt Body with an Impinging Shock Steady Computations for a Perfect Gas

Take an example of a 2D inviscid steady blunt-body flow with an impinging shock for a perfect gas with $M_\infty = 4.6$ computation. The freestream conditions for this flow field are the freestream temperature $T_\infty = 167$K and $\gamma = 1.4$ for a perfect gas. This flow field is typical of what may be experienced by the inlet cowl of a hypersonic aerodynamics vehicle. Figures 23 and 24 show the schematic of the computational domain, the Mach contours and the L2-norm residual of an inviscid shock-on-shock interaction on a blunt body with radius R_l and thickness $D = 2R_l$. An oblique shock with an angle of 20.9° relative to the free stream impinges on the bow shock. Various types of interactions occur depending on where the impingement point is located on the bow shock. As shown by the Mach contours ranging from 0 to 4.55 in increments of 0.05, the impinging shock has caused the stagnation point to move away from its undisturbed location at the symmetry line. The surface pressures at the new stagnation point can be several times larger than those at the undisturbed location of the stagnation point. In addition, a slip surface emanates from the bow shock and impinging shock intersection point and is intercepted by a shock wave that starts at the upper kink of the bow shock. The interacting shock waves and slip surfaces are confined to a very small region and must be captured accurately by the numerical scheme if the proper surface pressures are to be predicted correctly. The 77 × 77 grid used and the convergence rate computed by the implicit TVD scheme are shown in Figure 24. Though the pattern of the flow is significantly more complicated than for the previous cases, the convergence rate remains quite satisfactory.

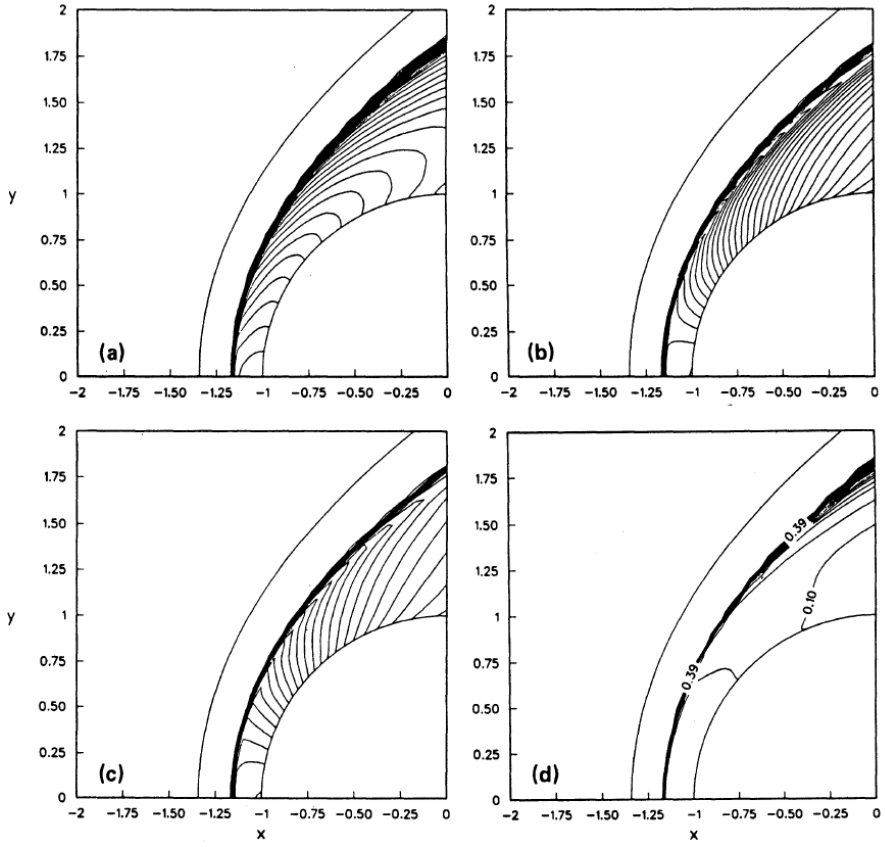

Figure 22. Blunt body steady computation with $M_\infty = 25$: the Mach contours (**a**), density contours (**b**), pressure contours (**c**) and (**d**) κ computed by an implicit scheme for an equilibrium real gas.

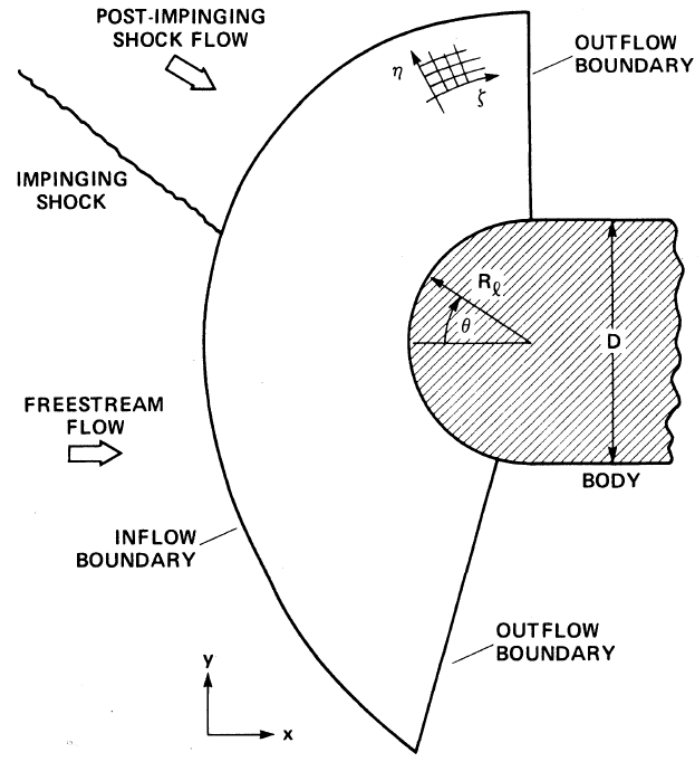

Figure 23. Schematic of the computational domain for a blunt-body flow with an impinging shock.

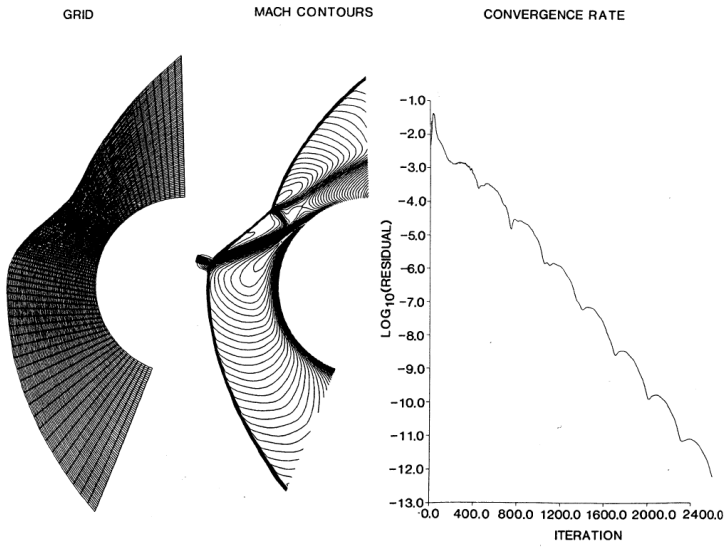

Figure 24. Two-dimensional inviscid steady blunt-body flow with an impinging shock for a perfect gas with $M_\infty = 4.6$.

8.4. Viscous Steady and Unsteady $M_\infty = 15$ Hypersonic Perfect Gas Computations with Impinging Shock

Figure 25 illustrates the shock resolution of unsteady and steady thin-layer Navier–Stokes computations by a second-order implicit time-accurate TVD scheme. The steady test case is similar to the previous impinging shock study except that the freestream Mach number is 15, the impingement shock angle is 22.75°, the free stream temperature is $T_\infty = 255.6$ K and the Reynolds number based on the diameter is 186,000. Shown are the Mach contours from 0 to 15 in increments of 0.1. For the unsteady computation, the impingement shock at the same angle relative to the freestream moves downward across the bow-shock of the blunt body. The impingement shock velocity is 10% of the freestream velocity ($M_\infty = 15$). Although the impingement shock locations for the unsteady and steady computations are similar, the shock patterns are very different. A 241 × 141 non-adaptive grid is used for both computations. A time step of 0.002 (equivalent to a maximum CFL of 48) is used for steady-state computations, whereas a time step of 0.0005 (equivalent to a maximum CFL of 10–12 at the vicinity of the boundary layer and a CFL of 1 for the rest of the flow field) is used for the unsteady computations. The steady-state solution can be reached in 1200 steps with a three order of magnitude drop in the L2-norm residual. Extra iterations are needed to bring the residual to a lower level; however, no change in the contour plots or surface pressures at least to within 3–4 digits of accuracy is observed.

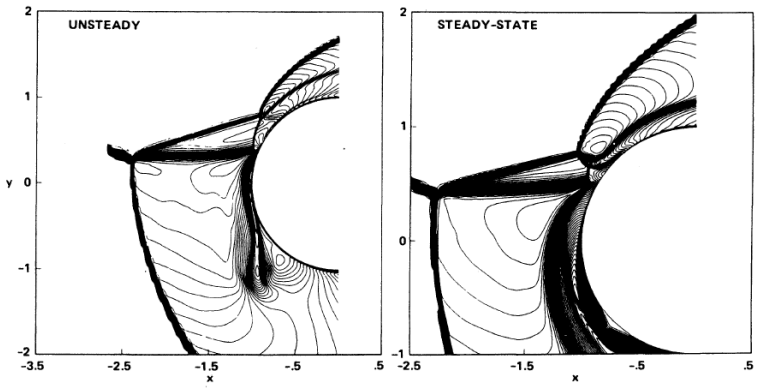

Figure 25. The Mach contours of a 2D viscous steady and unsteady hypersonic perfect gas with $M_\infty = 15$ and Re_0 = 186,000.

9. Numerical Examples: Spurious Numerics Related to Problems with Stiff Source Terms and Methods to Overcome the Issues

For nearly four decades, the wrong speed phenomenon has attracted a large volume of research work; see, e.g., [2,6–8,18–20,40,42,148–155]. In combustion and reacting flows, various strategies have been proposed to overcome this wrong speed difficulty for one to two species cases with a single reaction. Since numerical dissipation that spreads the discontinuity front is the cause of the wrong propagation speed of discontinuities, a natural strategy is to avoid any numerical dissipation in the scheme. In combustion, level set and front tracking methods were used to track the wave front to minimize this spurious behavior [149,152,153]; see Wang et al. [20] for a comprehensive overview of the last two decades of development. Wang et al. also proposed a new high-order finite difference method with subcell resolution for advection equations with stiff source terms for a single species to overcome the difficulty. For a subcell resolution method for multi-species, see Wang et al. [41]. See [18–20,40–42] for various examples in our effort to minimize the wrong propagation speed of discontinuities. For various project methods to minimize the wrong propagation speed of discontinuities, see [125–128] and the references cited therein.

9.1. One-Dimensional Scalar Reaction-Convection Test Case

This numerical phenomenon was first observed by Colella et al. [156] in 1986, who considered both the reactive Euler equations and a simplified system obtained by coupling the inviscid Burgers equation with a single convection/reaction equation. LeVeque and Yee (1990) [8] showed that a similar spurious propagation phenomenon can be observed even with scalar equations, by properly defining a model problem with a stiff source term. They introduced and studied the simple one-dimensional (1D) scalar conservation law with an added inhomogeneous parameter-dependent source term

$$u_t + u_x = S(u), \tag{11}$$

$$S(u) = -\mu u(u - \frac{1}{2})(u - 1). \tag{12}$$

Between the time frame of 2010–2013, the authors revisited the LeVeque and Yee test case, and combustion and nonequilibrium reacting flows coupled system cases [18–20,40,42]. Here, we include the study of the LeVeque–Yee scalar test case using the subcell-resolution method reported in [42]. Figure 26 shows the shock location error as a function of the CFL number using 128 discrete CFL values between $(0.001, 8)$ with $6.291338583 \times 10^{-3}$ equal increment by WENO5 and WENO5/SR. WENO5/SR is the original Shu and Jiang fifth-order WENO using Wang et al.'s subcell-resolution method. Three grid refinements using $50, 150, 300$ uniform grid points and for three stiffness coefficients of the source term $\mu = 1, 100, 1000$ are compared. "Err" represents number of grid points away from the reference solution on the figure. Figure 26 indicates a general trend of the scheme behavior by WENO5/SR for the 1D scalar test case conducted by LeVeque and Yee (1990) [8]. In this case, WENO5 behaves differently from the system test case. In this case, all the nonlinearity and stiffness contained in the governing equation are due to the source term as the convection term in the LeVeque and Yee's scalar model PDE is linear. It appears that the nonlinearity due to the convection terms does not alter the general spurious behavior pattern.

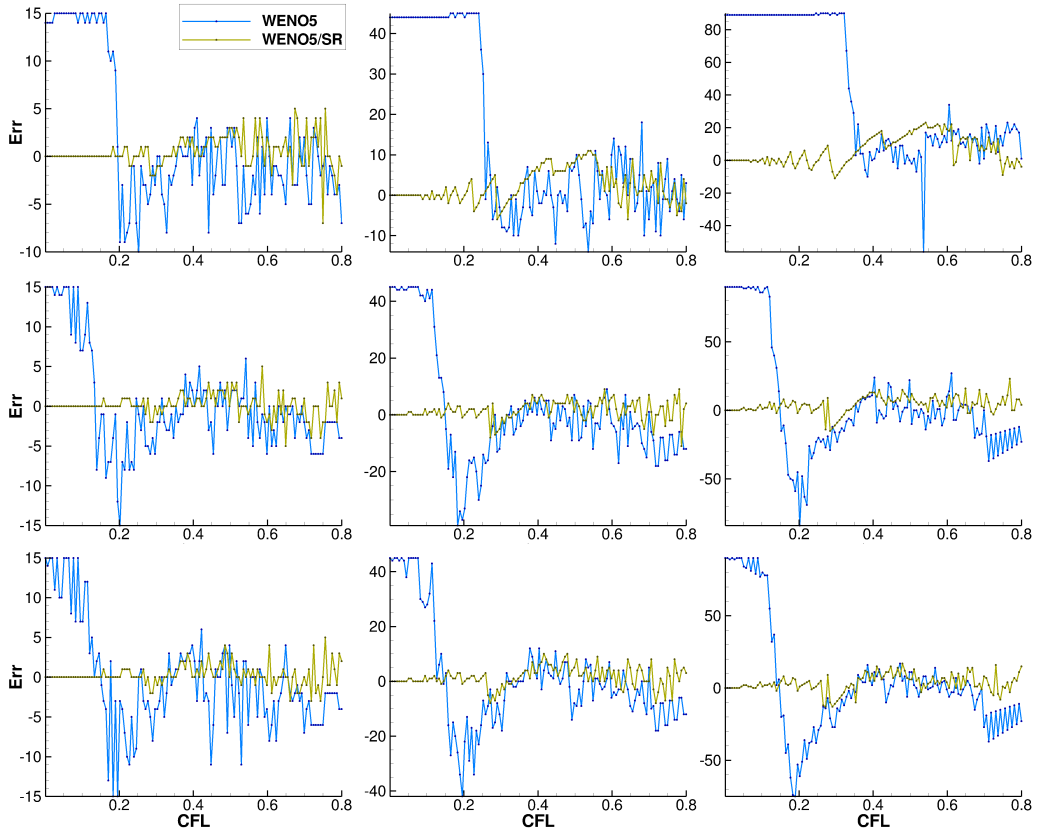

Figure 26. LeVeque and Yee linear advection and nonlinear stiff source term test case [8]. Number of grid points away from the reference shock solution (Err) as a function of the CFL number (128 discrete CFL values between $(0.001, 8)$ with $6.291338583 \times 10^{-3}$ equal increment) by WENO5 and WENO5/SR using $50, 150, 300$ uniform grid points (across) and for stiffness coefficients $\mu = 1, 100, 1000$ (top to bottom).

When the parameter μ is very large, a wrong propagation speed of discontinuity phenomenon by dissipative numerical methods is observed in coarse grids. In reacting flows, $\frac{1}{\mu}$ can be described as the reaction time. In order to isolate the problem, LeVeque and Yee solved (11) and (12) by the fractional step method using Strang splitting [157]. For this particular source term, the reaction (ODE) step of the fractional step method can be solved exactly. In their study using pointwise evaluation of the source term ($S(u)$ is evaluated at the j grid point index, i.e., $S(u_j)$ for each time evolution, the phenomenon of wrong propagation speed of discontinuities is connected with the smearing of the discontinuity caused by the spatial discretization of the advection term. They found that the propagation error is due to the numerical dissipation contained in the scheme, which smears the discontinuity front and activates the source term in a nonphysical manner. The smearing introduces a nonequilibrium state into the calculation. Thus, as soon as a nonequilibrium value is introduced in this manner, the source term turns on and immediately restores equilibrium, while at the same time shifting the discontinuity to a cell boundary. By increasing the spatial resolution by an order of magnitude, they were able to improve towards the correct propagation speed. It is remarked here that in a general stiff source term problem, a sufficient spatial resolution is as important as temporal resolution when the reaction step of the fractional step method cannot be solved exactly. Moreover, employing finite time steps and grid spacings that are below the standard Courant–Friedrich–Levy (CFL) limit on shock-capturing methods for compressible Euler and Navier–Stokes equations containing stiff reacting source terms and discontinuities reveals surprising counter-intuitive results.

9.2. Minimization of Wrong Propagation Speed of Discontinuities for Problems Containing Stiff Source and Discontinuities

Our studies in [42] found that using the Strang form of the operator splitting between the homogeneous part of the system of governing equations (without the source term) and the nonlinear stiff source terms is more stable than solving the fully coupled fluid-reaction equations. Here, Strang operator splitting is different from the skew-symmetric splitting of the inviscid flux derivatives. Strang operator splitting is commonly used in the combustion community to solve reacting flow problems. Figure 27 shows the schematic of Strang operator splitting. For the subcell resolution method, the subsequent two Figures 28 and 29 show the schematic of subcell-resolution methods. For problems with source terms employing any higher than first-order methods, we need to use methods that are well-balanced. See [18,19] for a well-balanced WENO method for chemical reacting flows.

On the Strang operator splitting approach, all of the aforementioned numerical methods (physics-preserving methods, shock-capturing methods and blending of more than one method) can be used to solve the reacting equations portion without the source terms first. Then, the source term is solved using an ODE (ordinary differential equations) solver, as indicated in Figures 28 and 29.

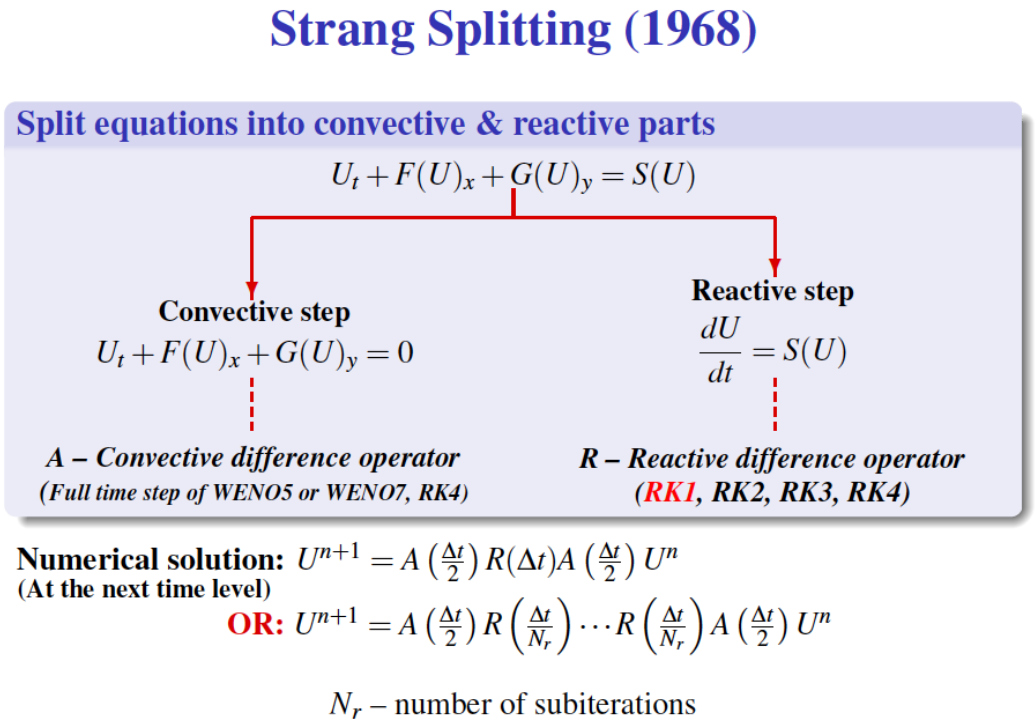

Figure 27. Schematic of Strang operator splitting on the homogeneous portion and the source term portion of the governing equations.

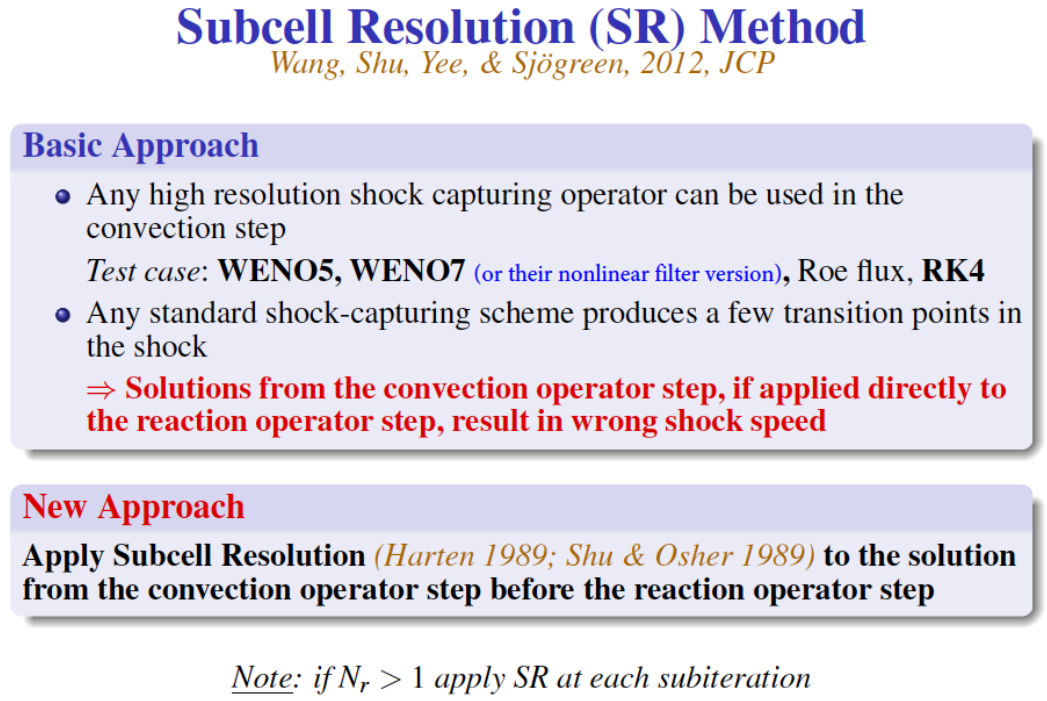

Figure 28. Subcell- resolution method in solving equations containing nonlinear source terms.

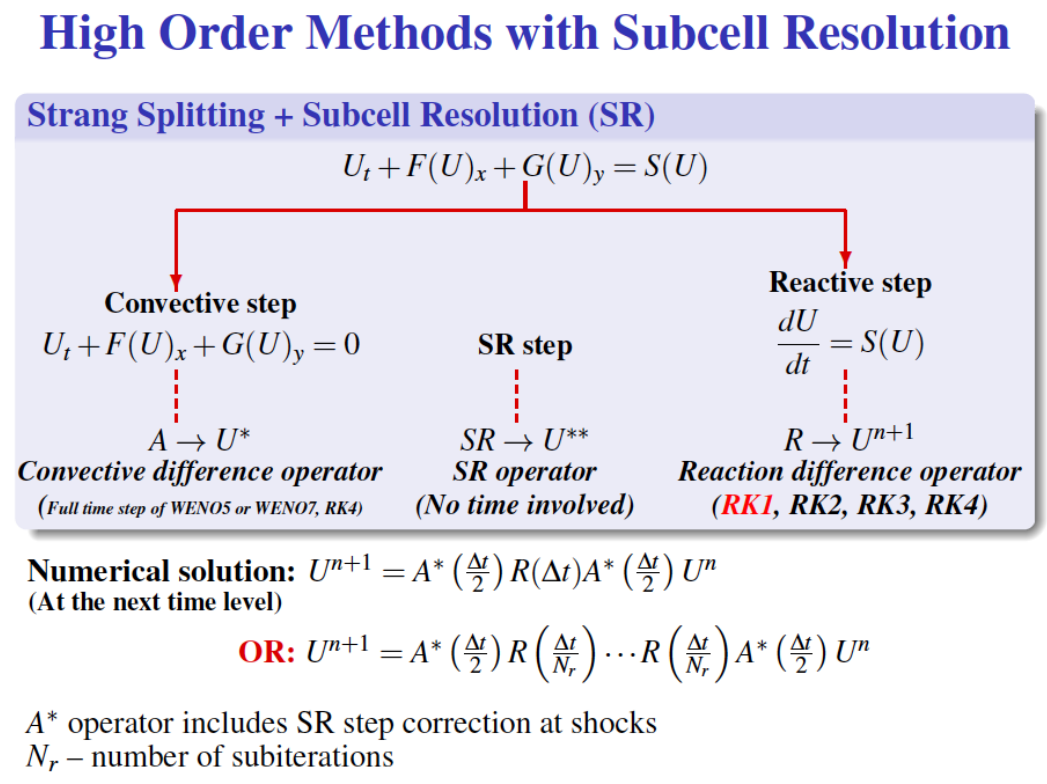

Figure 29. Subcell resolution using three staggered steps.

9.3. One-Dimensional Chapman–Joguet (C-J) Detonation Containing Stiff Source Terms and Discontinuities

The second example illustrates the effect of numerical dissipation on the propagation speed of a discontinuity for a 1D system in the presence of a stiff source term. We compute a 1D

C-J detonation for a one-reaction Arrhenius source term. This example, which was considered in [20], has been extensively studied, e.g., in [20,40,42,151,155]. See [20,42,151,155] for the initial flow conditions and additional results.

Figure 30 shows the 1D problem setup. Figure 31 shows a comparison of four high-order accurate shock-capturing schemes WENO5, WENO5fi, WENO5fi+split and our high-order subcell resolution version of WENO5 [20,42] (WENO5/SR). The new WENO5/SR method uses the Strang form of the splitting between the homogeneous part of the system of governing equations (without the source term) and the nonlinear stiff source terms. For each time integration, the first step is to solve the homogeneous system of governing equations. Then, a subcell resolution detector is used to correct the wrong numerical speed of propagation of discontinuities before solving the next step of the nonlinear stiff source term. It is remarked that the Strang splitting is not to be confused with the skew-symmetric splitting of the inviscid flux derivative as in Ducros et al.'s splitting [158]. The reference solution is computed by the WENO5 scheme on a uniform grid with 10,000 points. Here, WENO5fi+split denotes the use of sixth-order classical central spatial discretization together with the dissipative portion of WENO5. The term "split" here denotes the use of the Strang form of the splitting between the homogeneous part of the system of governing equations (without the source term) and the nonlinear stiff source terms in solving the governing equations.

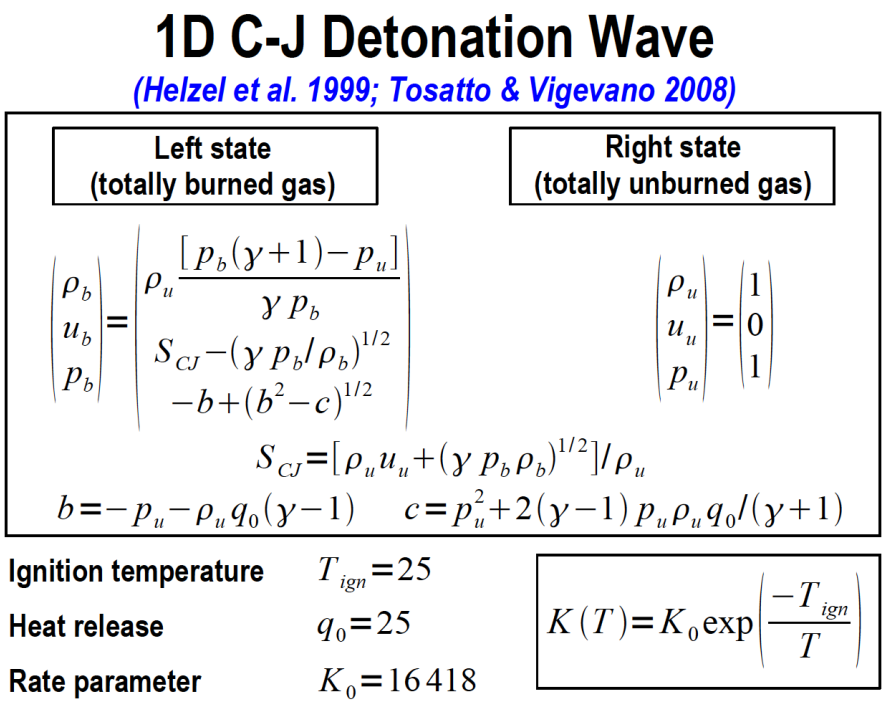

Figure 30. One-dimensional C-J detonation problem setup.

Figure 32 shows the number of grid points away from the reference shock solution (Err) as a function of the CFL number (128 discrete CFL values between $(0.001, 8)$ with $6.291338583 \times 10^{-3}$ equal increment) for three low dissipative shock-capturing methods WENO5/SR, WENO5fi+split and WENO5fi/SR+split using three 50, 150 and 300 uniform grid points and for three stiffness $K_0, 100K_0, 1000K_0$. Err is highly dependent on the grid, method and stiffness coefficient. The two subcell-resolution methods exhibit the least Err error.

Figure 33 shows the number of grid points away from the reference shock solution (Err) as a function of the CFL number (128 discrete CFL values between $(0.001, 8)$ with $6.291338583 \times 10^{-3}$ equal increment) for three low dissipative shock-capturing methods

WENO5/SR, WENO5fi+split and WENO5fi/SR+split, RK3 and RK4 time discretizations using two 150 and 300 uniform grid points, and stiffness K_0.

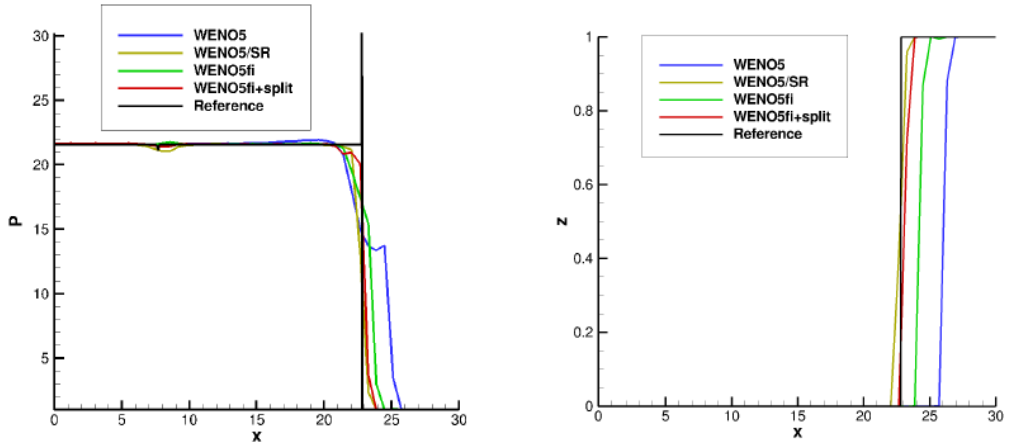

Figure 31. Pressure (**left**) and mass fraction of unburnt gas (**right**). Comparison among four high-order shock-capturing methods for a 1D C-J detonation problem. One reaction, Arrhenius model, using 50 uniformly distributed grid points.

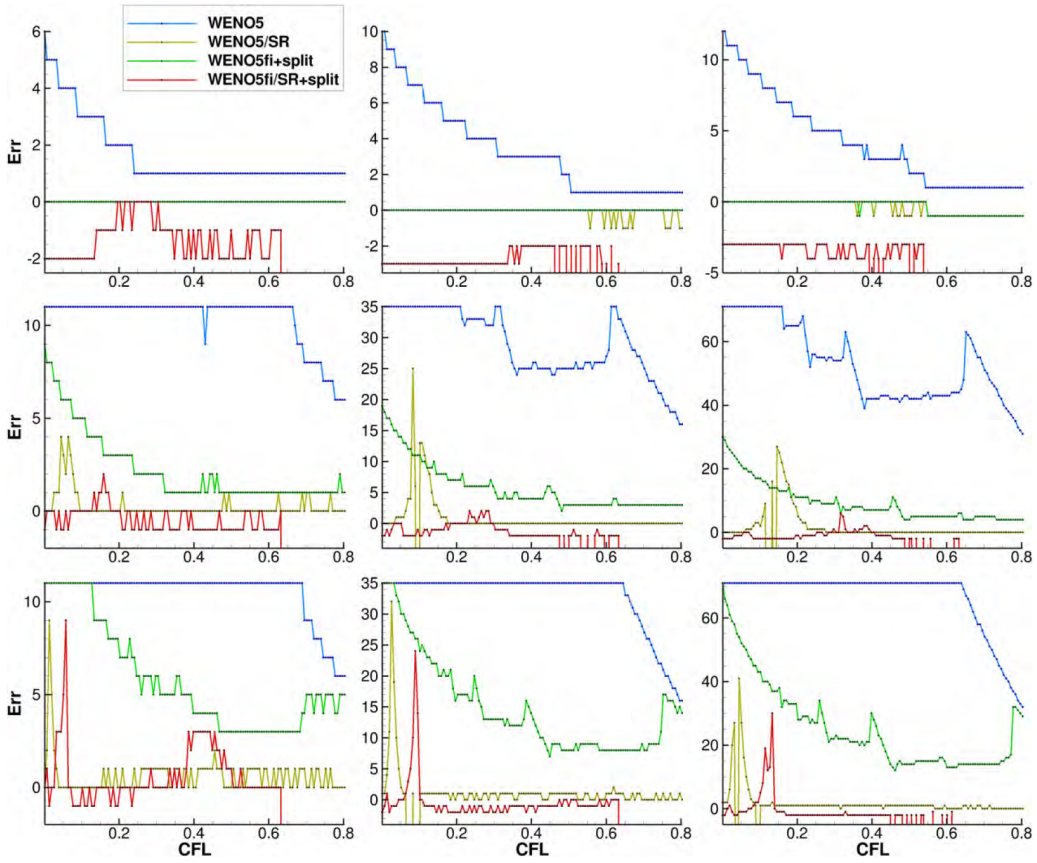

Figure 32. One-dimensional C-J detonation problem: Number of grid points away from the reference shock solution (Err) as a function of the CFL number (128 discrete CFL values between $(0.001, 8)$ with $6.291338583 \times 10^{-3}$ equal increment) for three low dissipative shock-capturing methods using 50, 150 and 300 uniform grid points (across) and for stiffness $K_0, 100K_0, 1000K_0$ (top to bottom).

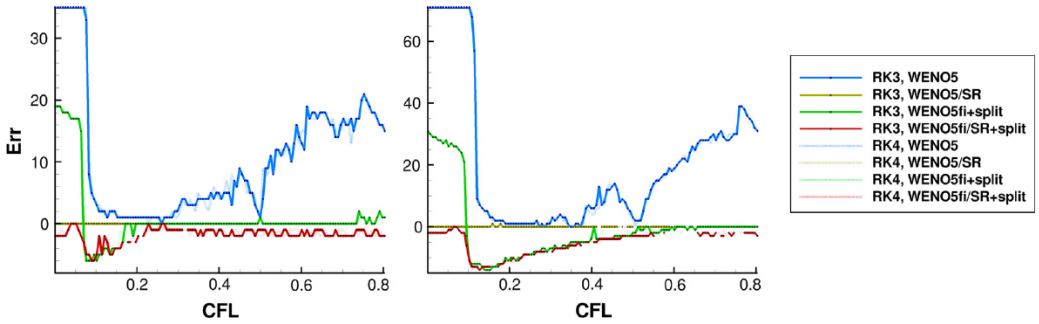

Figure 33. One-dimensional C-J detonation problem, Arrhenius case at $t = 1.8$. Comparison of the same three spatial discretizations with RK4 and RK3 temporal discretization using two 150, 300 uniform grid points (across) and stiffness K_0. Number of grid points away from the reference shock solution (Err) as a function of the CFL number (128 discrete CFL values between $(0.001, 8)$ with $6.291338583 \times 10^{-3}$ equal increment).

9.4. Two-Dimensional Chapman–Joguet (C-J) Detonation Containing Stiff Source Terms and Discontinuities [42]

Figure 34 shows a 2D C-J detonation problem setup. Figure 35 shows the density comparison by three methods comparing with the reference solution by WENO5 using 4000×800 uniform grid points. One important feature of this solution is the appearance of triple points, which travel in the transverse direction and reflect from the upper and lower walls. A discussion of the mechanisms driving this solution is given in [159]. Again, a pointwise evaluation of the source is employed for the 2D test case. Scheme behavior as a function of CFL, grid refinement and stiffness of the source terms was performed in Yee et al. (2013) [42]. WENO5/SR and WENO5fi+split are able to obtain the correct shock speed with similar accuracy compared to the reference solution. WENO5fi gives a slightly oscillatory solution near $x = 0.004$. WENO5 and WENO5/SR produce no oscillations at the same location. Further improvement of the flow sensor of the filter scheme is needed in order to remove the spurious oscillations. Furthermore, for the 500×100 grid, WENO5fi also obtained the correct shock speed. For $CFL = 0.05$, however, WENO5fi/SR+split is not able to obtain the correct shock speed for the stiff coefficient K_0. The WENO5fi+split method is the nonlinear filter approach using WENO5 on the entropy split form of the classical fourth-order central spatial discretization. Section X includes a brief introduction on the WENO5fi+split method and for any WENO order. Details can be found in [11–16,26,29,30].

Figure 36 shows a 1D cross-section of density at $t = 1.7 \times 10^{-7}$ by the same four methods as the 1D case on a uniform coarse grid of 200×40. The CFL=0.05 and $K_0 = 0.5825 \times 10^{10}$. The right figure is a close up of the vicinity of the discontinuity. The reference solution is by WENO5 using 4000×800 uniform grid points. WENO5 is more dissipative and also gives the largest error in the location of the discontinuity. WENO5fi performs better and is less dissipative because the WENO5 dissipation is not used everywhere in the computational domain. WENO5/SR gives the most accurate propagation speed but WENO5fi+split compares very well with WENO5/SR for this particular problem and grid size. The probable reason is that because of the stabilizing effect of the splitting, less dissipation is needed to keep WENO5fi+split stable. WENO5/SR and WENO5fi+split capture the correct structure using fewer grid points than in Helzel et al. [151] and in Tosatto and Vigevano [155].

Figure 37 shows the 2D detonation problem at $t = 1.7 \times 10^{-7}$ and $K_0 = 0.5825 \times 10^{10}$. The figure indicates the number of grid points away from the reference shock solution (Err) as a function of the CFL number (128 discrete CFL values between $(0.001, 8)$ with $6.291338583 \times 10^{-3}$ equal increment) for three low dissipative shock-capturing methods using 200×40 and 500×100 uniform grid points (across) and for stiffness $K_0, 100K_0, 1000K_0$ (top to bottom).

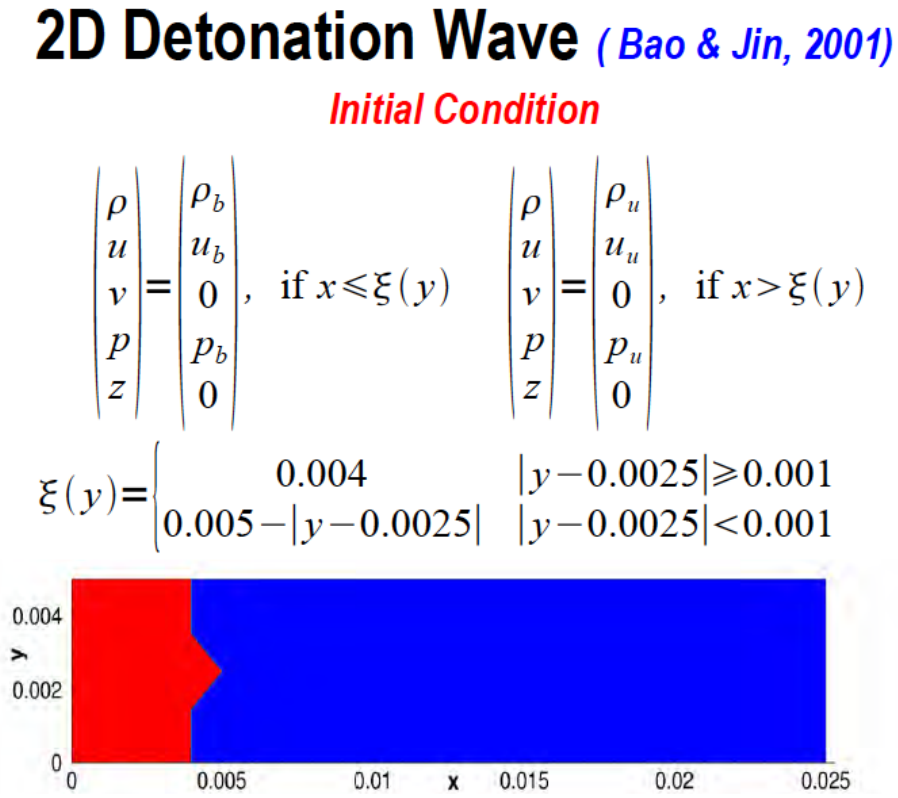

Figure 34. Two-dimensional C-J detonation problem setup.

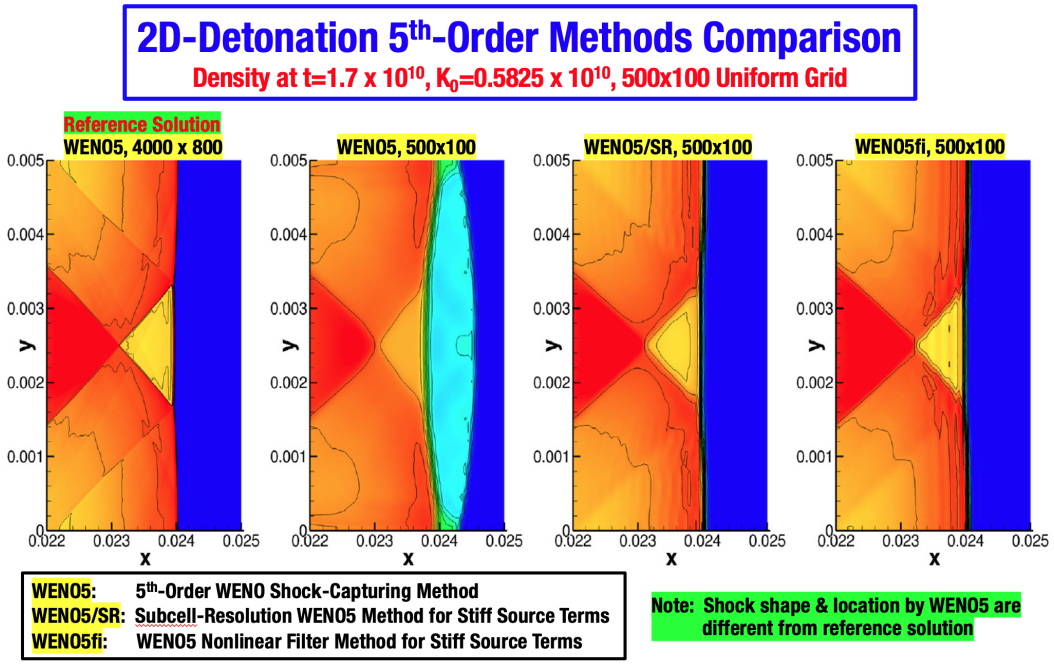

Figure 35. Two-dimensional detonation problem at $t = 1.7 \times 10^{-7}$ and $K_0 = 0.5825 \times 10^{10}$: Density computed by different methods. From left to right: reference solution by the standard WENO5 method using 4000×800 uniform grid points; WENO5, WENO5/SR and WENO5fi+split using 500×100 uniform grid points with $CFL = 0.05$.

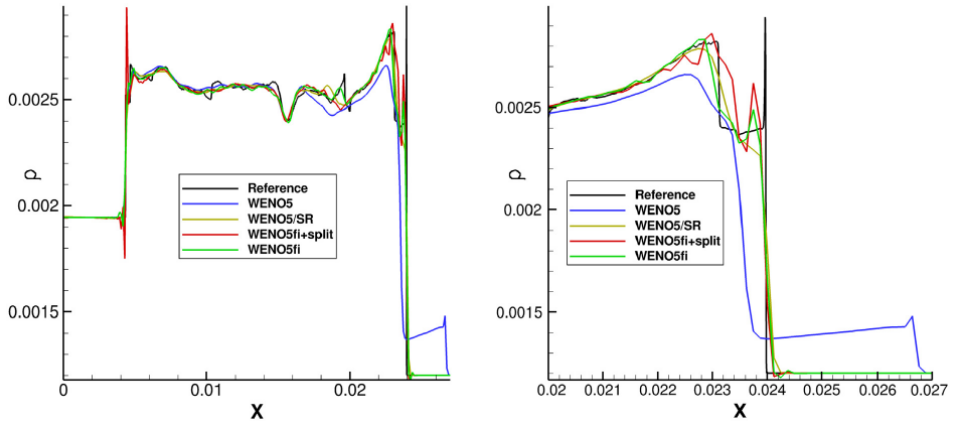

Figure 36. Two-dimensional C-J detonation comparison: 1D cross-section of density at $t = 1.7 \times 10^{-7}$ by the same four methods as the 1D case on a uniform coarse grid of 200×40. The CFL=0.05 and $K_0 = 0.5825 \times 10^{10}$. The right figure is a close up of the vicinity of the discontinuity. Note that there is an enlargement of the x domain in order to illustrate the wrong shock location. The reference solution is by WENO5 using 4000×800 uniform grid points.

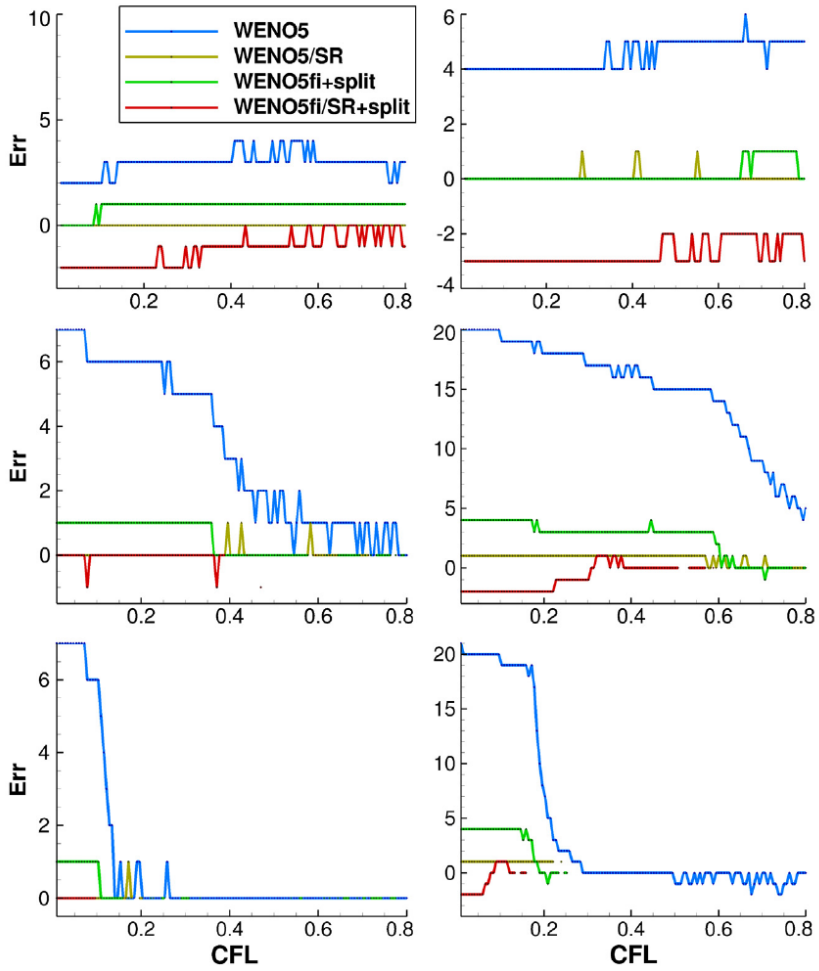

Figure 37. Two-dimensional detonation problem at $t = 1.7 \times 10^{-7}$ and $K_0 = 0.5825 \times 10^{10}$: Number of grid points away from the reference shock solution (Err) as a function of the CFL number (128 discrete CFL values between $(0.001, 8)$ with $6.291338583 \times 10^{-3}$ equal increment) for three low dissipative shock-capturing methods using 200×40 and 500×100 uniform grid points (across) and for stiffness $K_0, 100K_0, 1000K_0$ (top to bottom).

9.5. One-Dimensional and Two-Dimensional 13 Species EAST Simulations

The next two examples show the computations of a 1D and 2D 13-species chemical reacting flow by Kotov et al. and Yee et al. [4,42].

These 1D and 2D simulations consist of a 13-species chemical reacting flow, which is a simplified problem related to the NASA Electric Arc Shock Tube (EAST) experiment. Figure 38 shows the schematic of the EAST experiment. Figure 39 shows the EAST model governing equations in 1D, 2D and 3D. See [4,42] for flow notations. Figures 40 and 41 show the 1D and 2D problem setup. Figure 42 shows the comparison of three grids using the same WENO5fi method (left) and the comparison of five methods with the reference solution (right). The left subfigure of Figure 42 indicates how the shock/shear locations are dependent on the grid size using the same high-order method. The relative width between the shock and shear are the function of the grid spacing compared with the reference solution. The right subfigure indicates how the shock/shear locations are dependent on five different numerical methods (TVD, TVDafi+split, WENO5-llf, WENO5Pafi+split and TVD/SR). See [4] for the description of the five methods.

Figure 43 shows the temperature and pressure evolution of the 2D 13-species test case. Figure 44 shows the comparison of methods indicating how the shock/shear locations are dependent on the three methods. Different boundary layers are predicted by the three different methods as well. Here, WENO5-LLF denotes WENO5 using the local Lax–Friedrichs flux (LLF), and WENO5P-LLF denotes a positivity-preserving WENO5 of Zhang and Shu [160] using the LLF. The relative width between the shock and shear is a function of the methods.

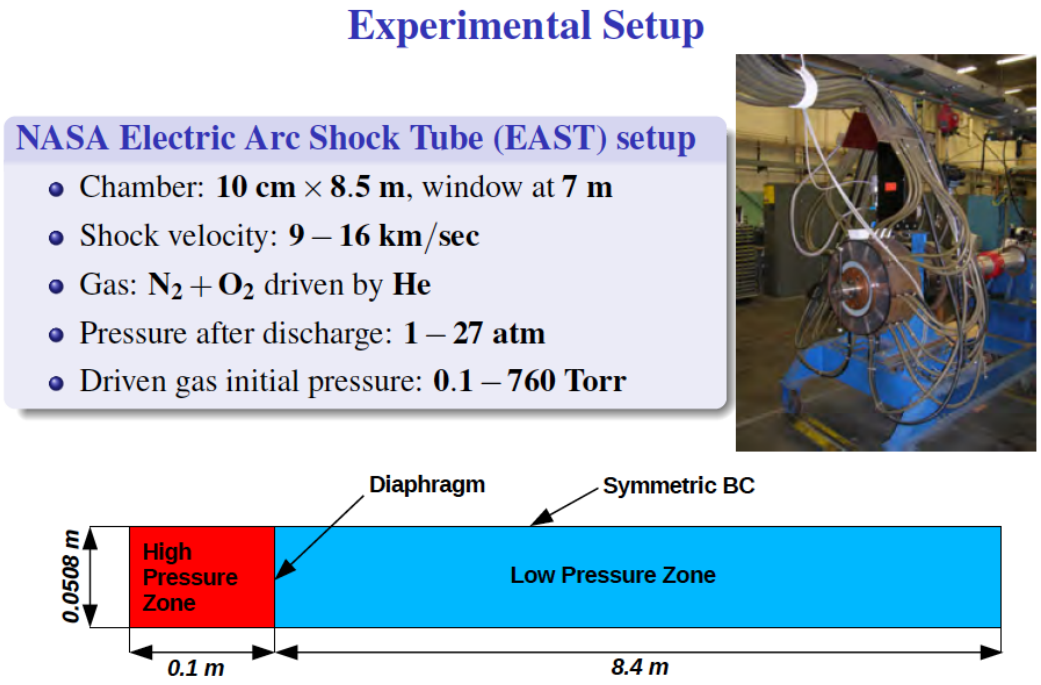

Figure 38. The EAST experiment.

EAST Problem. Governing equations

NS equations for 2D (i=1,2) or 3D (i=1,2,3) chemically non-equilibrium flow:

$$\frac{\partial \rho_s}{\partial t}+\frac{\partial}{\partial x_j}(\rho_s u_j+\rho_s d_{sj}) = \Omega_s$$

$$\frac{\partial}{\partial t}(\rho u_i)+\frac{\partial}{\partial x_j}(\rho u_i u_j+p\delta_{ij}-\tau_{ij}) = 0$$

$$\frac{\partial}{\partial t}(\rho E)+\frac{\partial}{\partial x_j}(u_j(E+p)+q_j+\sum_s \rho_s d_{sj} h_s-u_i\tau_{ij}) = 0$$

$$\rho=\sum_s \rho_s \qquad p=RT\sum_{s=1}^{N_s}\frac{\rho_s}{M_s} \qquad \rho E=\sum_{s=1}^{N_s}\rho_s\left(e_s(T)+h_s^0\right)+\frac{1}{2}\rho v^2$$

$$\tau_{ij}=\mu\left(\frac{\partial u_i}{\partial x_j}+\frac{\partial u_j}{\partial x_i}\right)-\mu\frac{2}{3}\frac{\partial u_k}{\partial x_k}\delta_{ij} \qquad d_{sj}=-D_s\frac{\partial X_s}{\partial x_j} \qquad q_j=-\lambda\frac{\partial T}{\partial x_j}$$

$$\Omega_s=M_s\sum_{r=1}^{N_r}\left(b_{s,r}-a_{s,r}\right)\left[k_{f,r}\prod_{m=1}^{N_s}\left(\frac{\rho_m}{M_m}\right)^{a_{m,r}}-k_{b,r}\prod_{m=1}^{N_s}\left(\frac{\rho_m}{M_m}\right)^{b_{m,r}}\right]$$

Figure 39. The EAST model governing equations in 1D, 2D and 3D. See [4,42] for flow notations.

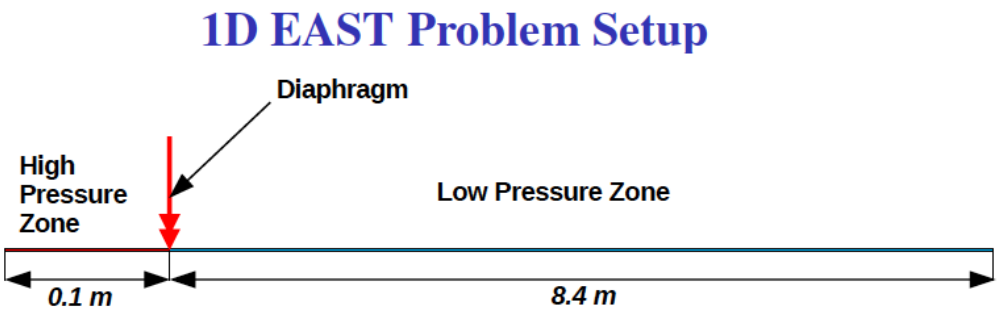

13 species mixture:

$e^-, He, N, O, N_2, NO, O_2, N_2^+, NO^+, N^+, O_2^+, O^+, He^+.$

High Pressure Zone

ρ	$1.10546\ kg/m^3$
T	$6000\ K$
p	$12.7116\ MPa$
Y_{He}	0.9856
Y_{N_2}	0.0144

Low Pressure Zone

ρ	$3.0964\times10^{-4} kg/m^3$
T	$300\ K$
p	$26.771\ Pa$
Y_{O_2}	0.21
Y_{N_2}	0.79

Figure 40. One-dimensional 13-species problem setup related to the EAST experiment.

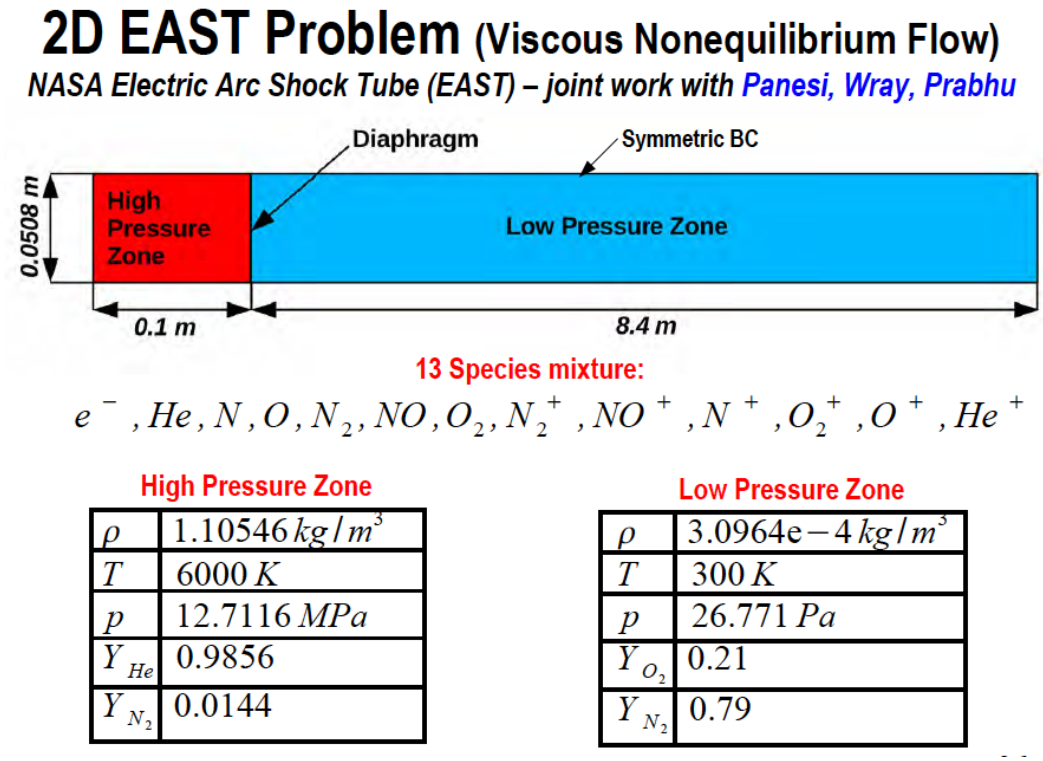

Figure 41. Two-dimensional 13-species problem setup related to the EAST experiment.

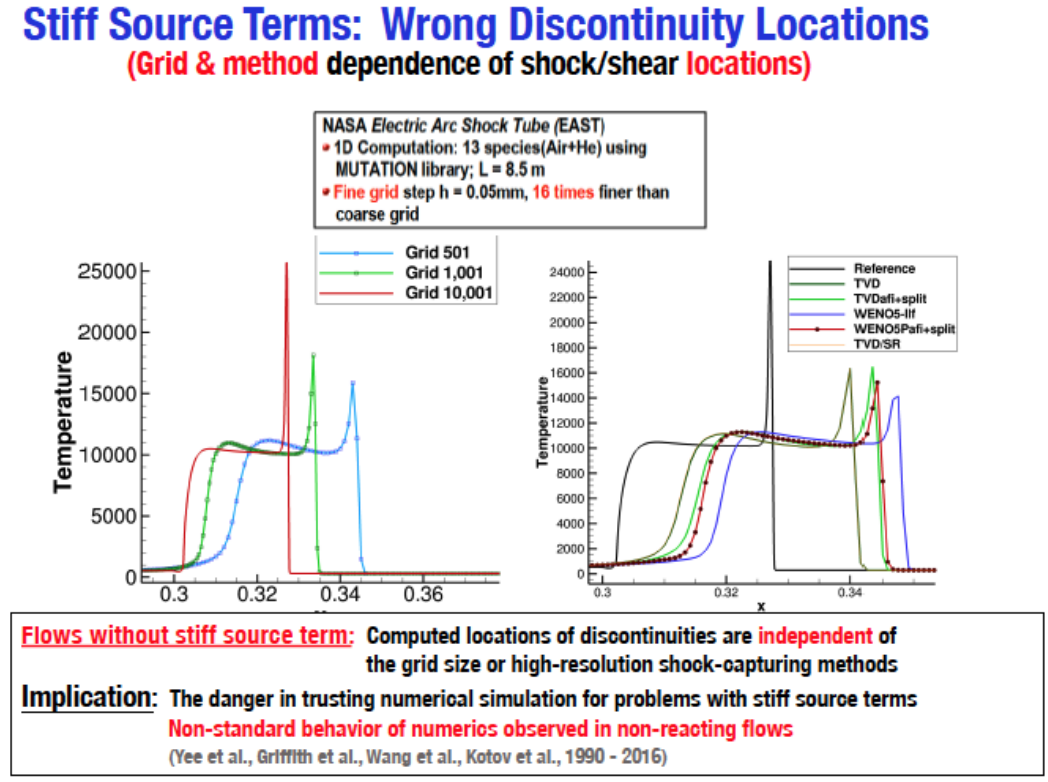

Figure 42. Temperature comparison using three grids and comparison among five high-order shock-capturing methods for 1D 13-species chemical reacting flows.

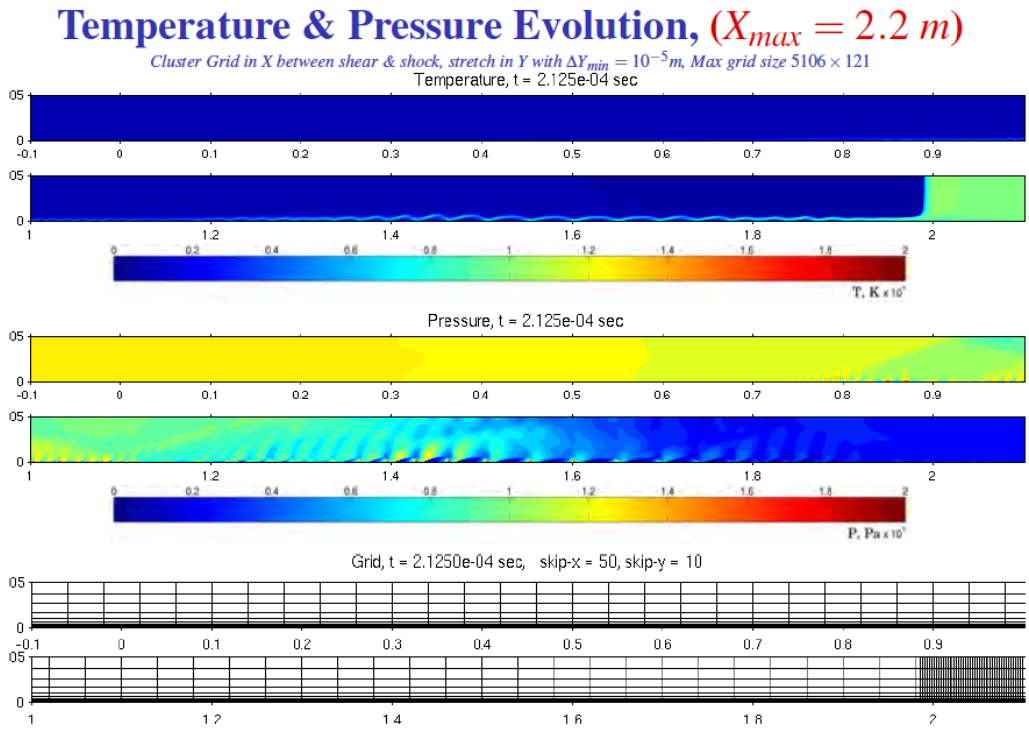

Figure 43. Temperature and pressure evolution of the 2D 13 species chemical reacting flows.

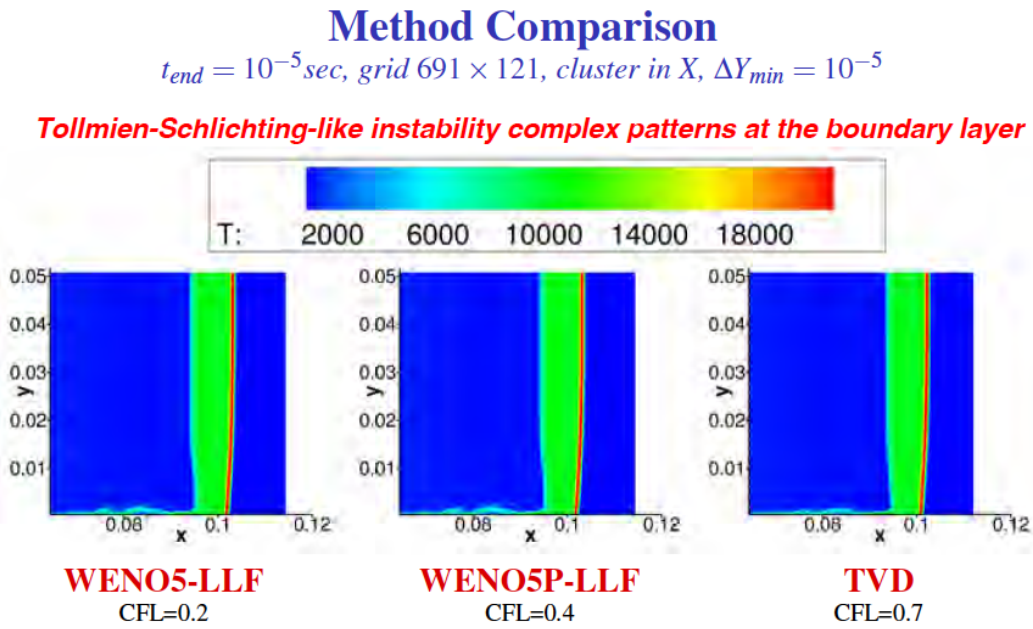

Figure 44. Temperature comparison among three high-order shock-capturing methods for the same 2D 13-species chemical reacting flows.

10. How Numerical Dissipation Affects the Predictability and Reliability of Simulation of Compressible Turbulence with Shock Waves

This section show how numerical dissipation affects PAR of compressible turbulence with shock waves. A short historical perspective and a brief description of the high-order methods being heavily used are included in this section.

ENO and WENO methods utilizing the shock resolving capability of TVD schemes together with higher order accuracy were developed in the late 1980s and early 1990s. In the past two decades, many variants of ENO and WENO methods were derived, yet they were still too dissipative away from shock waves for long-time integration of turbulent flows. For this reason, straightforward application of these original and recently developed high-order variants of ENO and WENO methods alone appear to not be a preferred choice for highly resolved turbulence simulations that push the resolution to the limit without resorting to using an extremely fine grid. From now on, the terms TVD, ENO and WENO refer to their original formulations and their variants. In other words, using one single method during the entire flow evolution usually posted shortcomings for complex turbulence flow development. A blending of more than one method to cater to the particular flow regions or different stages of turbulence development guided by a smart flow sensor at each time step on the type and amount of numerical dissipation is needed and would help to improve the overall stability, accuracy and reliability of simulations.

Since the late 1990s, blending of more than one method basically concentrated on two categories of such development: (a) the hybrid method, which switches between high-order non-dissipative methods and high-order shock-capturing methods (e.g., high-order WENO or ENO) guided by a flow sensor on the computed data; (b) the high-order nonlinear filter method of Yee et al., Sjögreen and Yee, and Yee and Sjögreen [4,10,13,25,27,28,40,161]. For our nonlinear filter methods, after the completion of a full time step of the primary high-order non-dissipative linear scheme, a smart local flow sensor would examine the computed data by flagging the locations and the amount of numerical dissipations that are needed. Then, the computed data would be filtered by a dissipative portion of high-order shock-capturing methods according to the flagged locations and the percentage amount of shock-capturing dissipation. More sophisticated forms with more than one type of numerical dissipation and local sensors are reported in [4,5,27,28]. For the performance of the nonlinear filter methods using high-order non-dissipative Padé (compact) spatial methods as the primary (base) methods, see [11,14,162]. For performance of the nonlinear filter methods using the high-order dispersion relation preserving (DRP) methods for aeroacoustic application, see Many of the recent developers of more complex variants of ENO and WENO are considering the aforementioned hybridized approach with their own flow sensors.

The majority of existing high-order methods, including hybrid or high-order nonlinear filter methods, might not discretely preserve the desirable physics-preserving properties (e.g., entropy conserving, momentum conserving and or kinetic energy preserving with added mechanism). To further minimize the use of numerical dissipation and to preserve some of the key physical properties, the current trend in turbulence/shock numerical simulations uses adaptive blending of a high-order **skew-symmetric form of physics-preserving non-dissipative methods** with the desired high-order shock-capturing methods guided by a smart flow sensor in a manner to further minimize the aid of added numerical dissipation. Here, the non-dissipative classical central, Padé (compact) or dispersion relation preserving (DRP) spatial discretization is applied to the skew-symmetric form of the inviscid flux derivatives. High-order skew-symmetric forms of physics-preserving methods blended with high-order shock-capturing methods can be found in [11–16,26,29,30]. Our studies indicated that the nonlinear filter approach provides similar accuracy but is more efficient than the hybrid approach in conjunction with higher than one stage of time discretization, e.g., higher than the first order of Runge–Kutta methods.

10.1. Short Overview of Hybrid Methods

Consider a 1D hyperbolic conservation law, where $\mathbf{U}$ is the vector of flow variables, $\mathbf{F}_x$ is the inviscid flux derivative, and t and x represent time and the computational space in x in a computational domain

$$\mathbf{U}_t + \mathbf{F}_x = 0.$$

For simplicity, we assume the semi-discrete form uses a uniform finite difference method (FDM) grid $x_j = (j-1)\Delta x$, $j = 1, \ldots, N$, where Δx is the grid spacing. Denote $\mathbf{U}_j$ and $\mathbf{F}_j$ as the approximation of $\mathbf{U}$ and $\mathbf{F}$ at grid spacing j. A semi-discrete form of a chosen method is

$$\frac{d\mathbf{U}_j}{dt} + \frac{\mathbf{H}_{j+1/2} - \mathbf{H}_{j-1/2}}{\Delta x} = \mathbf{0}, \tag{13}$$

where $\mathbf{H}_{j+1/2}$ denotes numerical fluxes consistent with $\mathbf{F}$. A simple hybrid method switching between two methods can be written as

$$\mathbf{H}_{j+1/2} = (1 - \nu_{j+1/2})\mathbf{H}^C_{j+1/2} + \nu_{j+1/2}\mathbf{H}^S_{j+1/2},$$

where $\mathbf{H}^C_{j+1/2}$ is a high-order non-dissipative numerical flux and $\mathbf{H}^S_{j+1/2}$ is a high-order shock-capturing numerical flux. $\nu_{j+1/2}$ is a local flow sensor. For a 1D system of hyperbolic conservation laws using a complete set of characteristic waves, the high-order shock-capturing methods are preferred to discretize locally each of the characteristic waves by a complete set of Riemann solvers [17,21,25,26,163]. If a multidimensional method is not used, it is very common to apply a 1D Riemann solver method dimension-by-dimension for a multi-dimensional system of hyperbolic conservation laws [4,5,10,17,27,28,163]. See some recent related development [164–166].

10.2. Overview of Nonlinear Filter

The nonlinear filter approach is less known in the aerodynamics CFD application community as it has not been described in CFD references or textbooks. This section gives a longer overview than the hybrid method approach, including test cases from our extensive work [10,12,13,15,16,27,28,65,161,167].

In a nutshell, a nonlinear filter approach consists of a base scheme step and a post-processing nonlinear filter step.

10.2.1. Base Scheme Step

A full time step is advanced using a high-order non-dissipative spatially central scheme (classical central, Padé or DRP method). A summation-by-parts (SBP) boundary operator [56,57] and a matching order conservative high-order freestream metric evaluation for curvilinear grids [17] are used. A high-order temporal discretization such as the third-order TVD Runge–Kutta or fourth-order Runge–Kutta (RK3 or RK4) method is used.

10.2.2. Nonlinear Filter Step—A Post-Processing Step

Instead of the hybrid approaches, to further improve nonlinear stability and accuracy from the non-dissipative spatial base scheme, the computed data are nonlinearly filtered by a dissipative portion of a high-order shock-capturing scheme with a local smart flow sensor. At each grid point, the local flow sensor(s) is employed to analyze the regularity of the computed flow field from the base scheme step. Only strong discontinuity locations would receive the full amount of shock-capturing dissipation. In smooth regions, no dissipation is added unless high-frequency oscillations are detected. In regions with strong turbulence, if needed, a small fraction of the shock-capturing dissipation can be added to improve stability. Note that the nonlinear filter numerical fluxes only involve the inviscid flux derivatives regardless of whether the flow is viscous or inviscid. If viscous terms are present, for ease of the SBP boundary closure implementation for the viscous flux derivatives, the same inviscid central difference operator used for the first derivative is employed twice for the viscous flux derivatives. For a variety of local flow sensors with automatic selection of different flow types, see [28].

The nonlinear filter idea was first introduced and tested by Yee et al. [25,26], using an artificial compression method (ACM) of Harten [168] as the flow sensor. Later, smart flow sensors were developed by Sjögreen and Yee, Yee and Sjögreen, and Kotov et al. [4,5,10,27,28]. Unlike the hybrid approach, in the presence of physical viscosity, the primary high-order

non-dissipative scheme includes the discretizations on both the inviscid and viscous portion of the governing equation before the nonlinear filtering post-processing step. This is opposed to the hybrid method. It examines the computed flow data from the previous time step information. In addition, switching between two methods that can create instability during frequent switching between two methods is opposed to the nonlinear filter methods that do not switch among methods. The high-order base scheme again can be a standard central, Padé or DRP method, depending on the flow type in question.

Denote the computed solution by the base scheme step by $U^*_{j,k,l}$ of 3D Euler equations of gas dynamics. After the completion of a full time step of the spatial base scheme step at time n, the final update of the solution after the filter step at time $n+1$ (with the numerical fluxes in the y- and z-directions suppressed as well as their corresponding y- and z-direction indices on the x inviscid flux suppressed) is

$$U^{n+1}_{j,k,l} = U^*_{j,k,l} - \frac{\Delta t}{\Delta x}[H^*_{j+1/2} - H^*_{j-1/2}], \tag{14}$$

$$H^*_{j+1/2} = R_{j+1/2}\overline{H}_{j+1/2}. \tag{15}$$

The nonlinear filter numerical fluxes usually involve the use of field-by-field approximate Riemann solvers. If the Roe type of approximate Riemann solver [169] is employed, for example, the x-filter numerical flux vector $H^*_{j+1/2}$ is evaluated at the $U^*_{j,k,l}$ solution from the base scheme step. $R_{j+1/2}$ is the matrix of right eigenvectors of the Jacobian of the inviscid flux vector in terms of Roe's average states based on U^*. $H^*_{j+1/2}$ and $H^*_{j-1/2}$ are "filter" numerical fluxes in terms of Roe's average states based on $U^*_{j,k,l}$. Denote the elements of the filter numerical flux vector $\overline{H}_{j+1/2}$ by $\overline{h}^m_{j+1/2}, m = 1, 2, ..., 5$. The element of the filter numerical flux $\overline{h}^m_{j+1/2}$ has the form

$$\overline{h}^m_{j+1/2} = \frac{\kappa^m_{j+1/2}}{2} w^m_{j+1/2}\phi^m_{j+1/2}. \tag{16}$$

where $w^m_{j+1/2}$ is a flow sensor to activate the nonlinear numerical dissipation portion of a high-order shock-capturing scheme $\frac{1}{2}\phi^m_{j+1/2}$. The term $\kappa^m_{j+1/2}$ represents a locally determined positive parameter that is less than or equal to one, based on the regularity of the computed data. The choice of the parameter κ can be different for different flow types and is automatically chosen by using the local $\kappa^m_{j+1/2}$ described in [28]. However, if the computation used the Ducros et al. flow sensor, we set $\kappa^m_{j+1/2} = 1$ [170].

Figure 45 shows the nonlinear filter procedure for a system of 1D hyperbolic conservation laws. Figure 46 shows the nonlinear filter procedure using a combination of more than one flow sensor. Figure 46 also shows how to obtain, e.g., the dissipative portion of a seventh-order WENO (WENO7) denoted by $\phi^m_{j+1/2} = g^m_{j+1/2} - b^m_{j+1/2}$. The term $g^m_{j+1/2}$ represents the mth characteristic term of WENO7 and $b^m_{j+1/2}$ represents the mth characteristic term of the eighth-order central method. The nonlinear filter approach using WENO7 is denoted by WENO7fi on some of the later numerical test result presentations.

10.2.3. A Historical Note on Nonlinear Filter Approaches

The original idea of the nonlinear filter approach of Yee et al. (2000) [25] was based on shock-capturing methods that are written into a central discretization portion and a nonlinear shock-capturing portion (dissipative portion). All variants of TVD schemes are already written in this form by design. In order to obtain the dissipative portion of other high-order shock-capturing methods, the dissipative portion of the considered shock-capturing $\phi^m_{j+1/2} = g^m_{j+1/2} - b^m_{j+1/2}$ can be obtained in a similar manner as WENO7fi.

Nonlinear Filter Step $(U_t + F_x(U) = 0)$

- **Denote the solution by the base scheme (e.g. 6^{th} order central, $4th$ order RK)**

$$U^* = L^*(U^n)$$

- **Solution by a nonlinear filter step**

$$U_j^{n+1} = U_j^* - \frac{\Delta t}{\Delta x}\left[H_{j+1/2} - H_{j-1/2}\right]$$
$$H_{j+1/2} = R_{j+1/2}\overline{H}_{j+1/2}$$

$\overline{H}_{j+1/2}$ **- numerical flux,** $R_{j+1/2}$ **- right eigenvector, evaluated at the Roe-type averaged state of** U_j^*

- **Elements of** $\overline{H}_{j+1/2}$**:**

$$\overline{h}_{j+1/2} = \frac{\kappa^m_{j+1/2}}{2}\left(s^m_{j+1/2}\right)\left(\phi^m_{j+1/2}\right)$$

$\phi^m_{j+1/2}$ - ***Dissipative portion of a shock-capturing scheme***
$s^m_{j+1/2}$ - ***Local flow sensor*** *(indicates location where dissipation needed)*
$\kappa^m_{j+1/2}$ - ***Controls the amount of*** $\phi^m_{j+1/2}$

Figure 45. Nonlinear filter procedure.

Improved High Order Filter Method

Form of nonlinear filter

$$\overline{h}_{j+1/2} = \frac{\kappa^m_{j+1/2}}{2}\left(s^m_{j+1/2}\right)\left(g^m_{j+1/2} - b^m_{j+1/2}\right)$$

Control amount of dissipation based on local flow condition

Local flow sensor (*Shock Sensor, ACM (Harten), Ducros et al, Multiresolution wavelet, etc.*)

Any High Order Shock capturing numerical flux (*e.g. WENO7*)

High order central numerical flux (*e.g.* 8^{th} *order central*)

2007 – κ = global constant
2009 – $\kappa_{j+1/2}$ = local, evaluated at each grid point
Simple modification of κ *(Yee & Sjögreen, 2009)*

$$\kappa = f(M)\cdot\kappa_0$$
$$f(M) = min\left(\frac{M^2}{2}\frac{\sqrt{4+(1-M^2)^2}}{1+M^2}, 1\right)$$

For other forms of $\kappa_{j+1/2}, s_{j+1/2}$, see *(Yee & Sjögreen, 2009)*

Figure 46. Nonlinear filter procedure with local flow sensors.

It is noted that the nonlinear filter step described above should not be confused with the LES filtering operation. For extension of the blending of more than one numerical method to the ideal MHD, see [12,13,15,16,27,28,65,161,167].

As mentioned briefly above, the nonlinear filter schemes are efficient by construction. The total computational cost for a given error tolerance is significantly lower than for standard shock-capturing schemes or their hybrid cousins of the same order. One important reason for their efficiency is that the nonlinear shock-capturing filter dissipation is applied after each full time step of the base scheme, whereas a standard shock-capturing/hybrid method evaluates the shock-capturing method at each stage of the, e.g, m stage Runge–Kutta (R-K) time stepping scheme. Hence, the nonlinear filter approach requires only one shock-capturing method evaluation per time step per grid point per dimension, independent of the time discretization involved. Hybrid schemes, which switch between the high-order non-dissipative method and high-order shock-capturing method, require m Riemann solvers for each m stages of the R-K time discretization. Therefore, the hybrid methods are less efficient than the nonlinear filter methods. The hybrid method also can encounter numerical instability as well as conservation issues related to switching between schemes at the switch locations.

In addition, if the computation considers the dimension-by-dimension and a complete set of characteristic waves Riemann solver approach, only **ONE** CPU intensive evaluation of a dissipative portion of a chosen high-order shock-capturing method in local characteristic variables is need per dimension, per time step and per grid spacing for the nonlinear filter approach, regardless of the time integrator. Contrary to the nonlinear filter method, for the hybrid method, the number of high-order shock-capturing methods using the same Riemann solver approach evaluations per dimension, per time step and per grid spacing would be four times by a four-stage Runge–Kutta time integrator.

Figure 47 shows a 3D isotropic turbulence with shocklets problem setup. Figure 48 shows the accuracy of our nonlinear filter method for the isotropic turbulence simulation with the smart flow sensor built-in. Comparing the resolution by the hybrid method reported in Johnson et al. [171], one can see that they produce the same accuracy. For the same 3D isotropic problem setup as in Johnson et al. [171] and performance of our nonlinear filter method, see [5].

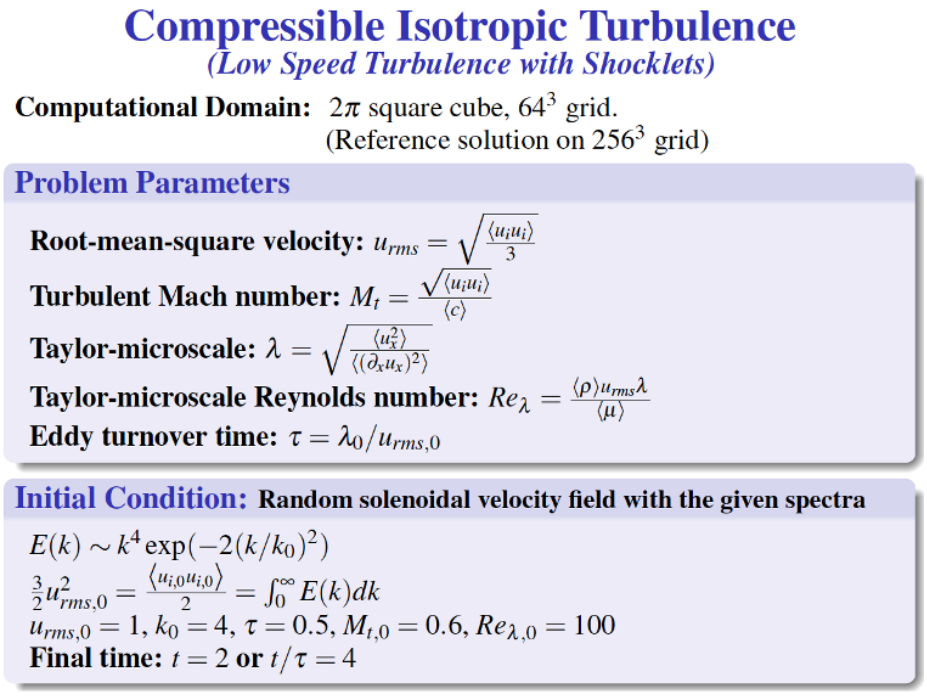

Figure 47. Three-dimensional isotropic turbulence with shocklets problem setup.

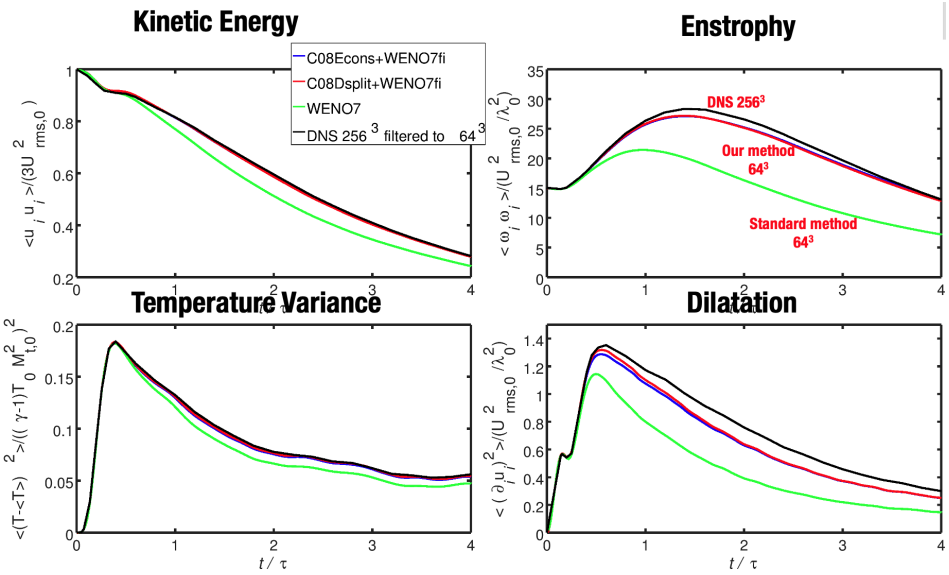

Figure 48. Three-dimensional Isotropic turbulence with shocklets: Comparison among standard 7th-order WENO method (WENO7) and our two 7th-order nonlinear filter methods (C08Econs+WENO7fi and C08Dsplit+WENO7fi) using a very coarse 64^3 grid with the filtered DNS computation on a 256^3 grid. Kinetic energy (**top left**), Enstrophy (**top right**), Temperature Variance (**bottom left**) and Dilatation (**bottom right**). C08Econs denotes the 8th-order classical central applied to the entropy split form, and C08Dsplit denotes the 8th-order classical central applied to the Ducros et al. split form of the Euler inviscid flux derivative.

10.3. The Need for Efficient High-Order Physics-Preserving Methods Blending with High-Order Shock-Capturing Methods

In classical mechanics, temporal, spatial or both finite difference discretizations that conserve a certain physical property (or combination of physical properties) of the governing equations are most often referred to, in a broad sense, as structure-preserving numerical methods. See e.g., [172]. In the literature, structure-preserving methods are also denoted as **physics-preserving methods**. Here, we use these terms interchangeably. Temporal and spatially finite difference discretizations that discretely conserve fundamental properties of the chosen governing equations are hereafter are denoted as **structure-preserving methods (SPMs)**. SPMs have been gaining more attention in long-time integration of turbulent flows. A combination of these SPMs can further increase the reliability, stability and accurate simulation of fluid flows, especially for turbulent flows. It is noted that the majority of existing high-order methods, including hybrid or high-order nonlinear filter methods, might not discretely preserve the desirable physical-preserving properties (NOT SPM).

In the applied mathematics CFD community, entropy-conserving and entropy-stable methods have been flourishing for the last two decades [3,12,13,15,16,26,173–175]. Symplectic time integrators are used to prevent phase distortion, e.g., Hamiltonian systems or the Korteweg–deVries equations [176]. In the applied mechanics and CFD community, the importance of developing SPMs that conserve one or more fundamental properties of the governing equations (mass, minimizing phase distortion, momentum and physical entropy conserving, positivity of density and pressure, and kinetic energy preserving, etc.) has been ongoing for the last four decades. See e.g., [3,12,13,15,16,26,65,158,174,177,178] for some of the developments. Combinations of more than one SPM is also be possible. See [14,30] or the next section for formulations. Formulations using the DRP and Padé high-order SPM non-dissipative linear methods are presented in [11,14].

10.4. SPM Finite Difference Formulation in Split Form: Skew-Symmetric Splittings of the Compressible Euler Flux Derivatives

When the high-order non-dissipative spatial method discussed previously discretized a class of the skew-symmetric form of the inviscid Euler flux derivative (instead of the unsplit flux derivative), it was shown that the appearance of instabilities or aliasing errors in long-time integration of turbulence flows can be delayed. The splitting can be performed for certain flow variables or the entire convective flux derivative system. They are written in a special split form which is equivalent to the unsplit version, i.e., the split and unsplit governing equations are equivalent. However, after finite difference discretizations, certain different split forms can maintain a discrete entropy conservation, momentum conservation, kinetic energy preservation property or can provide a stable L2-like energy norm estimate for smooth solutions. See articles [3,12,13,15,16,26,30,45,65,158,174,177,179,180] for discussions of the performance of various skew-symmetric splitting approaches in DNS and LES applications. See Sjögreen et al. [13] for the extension of these skew-symmetric splittings to any even-order split approximation formulation for the Euler and MHD equations.

In the simplest form, a split approximation starts from rewriting the derivative of the product $(ab)_x$ as

$$(ab)_x = \alpha(ab)_x + \gamma a b_x + \beta a_x b, \tag{17}$$

before discretization, where a and b are functions of x. The parameters α, γ and β are so chosen to be still equivalent to the original $(ab)_x$ before discretization. A common split derivative is found by setting $\alpha = \gamma = \beta = 1/2$, which results in the form

$$(ab)_x = \frac{1}{2}(ab)_x + \frac{1}{2}ab_x + \frac{1}{2}a_x b. \tag{18}$$

The Ducros et al. splitting [158] starts with this particular non-conservative split form using the classical central discretization operator on the derivative terms. They then apply mathematical manipulations on the difference operators to make the final discretization into a conservative difference method. Their construction will be discussed shortly.

A split approximation for the derivative of the product of three functions $(abc)_x$ starts with rewriting the derivative as

$$\begin{aligned}(abc)_x \quad &= \alpha(abc)_x + \gamma[a(bc)_x + bca_x] + \beta[b(ac)_x + acb_x] \\ &\quad +\kappa[c(ab)_x + abc_x] + \delta[bca_x + acb_x + abc_x]\end{aligned} \tag{19}$$

before discretization, where a, b and c are functions of x. The parameters $\alpha, \gamma, \beta, \kappa$ and δ are chosen to be still equivalent to the original $(abc)_x$ before discretization. A well-known split derivative that can be written in conservative form and can improve nonlinear stability is the Kennedy and Gruber [45] splitting, which is kinetic energy preserving for the Euler equation by setting the first four parameters to be $1/4$ and $\delta = 0$ for the triple product derivative. See [45,179,180] for details.

For the nonlinear Euler equation of gas dynamics, a less known splitting of the inviscid flux derivative is the entropy splitting method of [26,178,181]. The key mathematical idea of the entropy splitting is that their split formulas can be used to estimate the L^2-norm-like or the energy norm of the computed solution for periodic and non-periodic boundary conditions. In the recent terminology, it is entropy stable (in the sense of possessing an energy estimate) for the Euler equations using high-order classical central or DRP central schemes in conjunction with summation-by-parts boundary operators [11,26,64,178,181–183]. See [64] for a follow on study of the subject. The next two subsections give a short overview of the Ducros et al. and entropy splitting methods.

10.5. Ducros et al. Type Conservative Splitting

The Ducros et al. split approximation [158] for the Euler equations of gas dynamics starts with (18) the terms of the split form approximated by

$$\frac{1}{2}D(ab) + \frac{1}{2}D(a)b + \frac{1}{2}aD(b), \tag{20}$$

where D is a centered finite difference operator, and a and b are functions of x. For this split approximation by a central, Padé or DRP discretization, after mathematical manipulations, the resulting method conserves momentum (see below). However, it is not obvious how to obtain a norm estimate for nonlinear systems.

The key step in the Ducros et al. [158] split approximation is to rewrite (20) in conservation form. For the second-order operator $Du_j = (u_{j+1} - u_{j-1})/(2\Delta x)$, we have

$$\frac{1}{2}D(ab) + \frac{1}{2}D(a)b + \frac{1}{2}aD(b) = \frac{1}{4\Delta x}\Delta_+[(a_j + a_{j-1})(b_j + b_{j-1})], \tag{21}$$

where $\Delta_+ q_j = (q_{j+1} - q_j)$.

The beauty is that Equation (21) can be generalized to standard centered difference operators of $2p$th-order of accuracy,

$$D_p u_j = \frac{1}{\Delta x}\sum_{k=1}^{p} \alpha_k^{(p)}(u_{j+k} - u_{j-k}). \tag{22}$$

The coefficients $\alpha_k^{(p)}$ satisfy

$$\sum_{k=1}^{p} k\alpha_k^{(p)} = \frac{1}{2} \qquad \sum_{k=1}^{p} \alpha_k^{(p)} k^{2n+1} = 0, \;\; n = 1, \ldots, p-1. \tag{23}$$

The right-hand side of the algebraic identity

$$a_{j+k}b_{j+k} - a_{j-k}b_{j-k} + (a_{j+k} - a_{j-k})b_j + a_j(b_{j+k} - b_{j-k}) = (a_{j+k} + a_j)(b_{j+k} + b_j) - (a_j + a_{j-k})(b_j + b_{j-k}) \tag{24}$$

is written on conservative form by

$$(a_{j+k} + a_j)(b_{j+k} + b_j) - (a_j + a_{j-k})(b_j + b_{j-k}) = \sum_{m=0}^{k-1}(a_{j-m} + a_{j+k-m})(b_{j-m} + b_{j+k-m}) - \sum_{m=0}^{k-1}(a_{j-1-m} + a_{j-1+k-m})(b_{j-1-m} + b_{j-1+k-m}). \tag{25}$$

The conservative form of the split approximation becomes

$$\begin{aligned}\frac{1}{2}D_p(ab) + \frac{1}{2}D_p(a)b + \frac{1}{2}aD_p(b) = \\ \frac{1}{\Delta x}\sum_{k=1}^{p}\frac{1}{2}\alpha_k^{(p)}\Big((a_{j+k}b_{j+k} - a_{j-k}b_{j-k}) + a_j(b_{j+k} - b_{j-k}) + (a_{j+k} - a_{j-k})b_j\Big) \\ = \frac{1}{\Delta x}\sum_{k=1}^{p}\frac{\alpha_k^{(p)}}{2}\Bigg(\sum_{m=0}^{k-1}(a_{j-m} + a_{j+k-m})(b_{j-m} + b_{j+k-m}) \\ - \sum_{m=0}^{k-1}(a_{j-1-m} + a_{j-1+k-m})(b_{j-1-m} + b_{j-1+k-m})\Bigg) = \frac{1}{\Delta x}(h_{j+1/2} - h_{j-1/2}),\end{aligned} \tag{26}$$

where the numerical flux is defined by

$$h_{j+1/2} = \sum_{k=1}^{p} \frac{1}{2}\alpha_k^{(p)} \sum_{m=0}^{k-1} (a_{j-m} + a_{j+k-m})(b_{j-m} + b_{j+k-m}). \tag{27}$$

Define

$$\Theta_{j+1/2}^{(p)}(a,b) = \sum_{k=1}^{p} \frac{1}{2}\alpha_k^{(p)} \sum_{m=0}^{k-1} (a_{j-m} + a_{j+k-m})(b_{j-m} + b_{j+k-m}). \tag{28}$$

Consider the x-direction inviscid flux for 3D Euler equations of gas dynamics equations

$$\mathbf{F} = [\rho u, \rho u^2 + p, \rho uv, \rho uw, (e+p)u]^T,$$

where the inviscid flux $\mathbf{F} = \mathbf{F}(\mathbf{U})$; the velocity vector $\mathbf{u} = [u(x,y,z), v(x,y,z), w(x,y,z)]^T$ in the x-, y- and z-directions; ρ denotes the density; p is the pressure; and e is the total energy. Denote $\mathbf{u}_j = (u_j, v_j, w_j)^T$ as the discretization at the j grid location with the y and z discretizations indices suppressed for simplicity. The flux components can be written as products of two factors in many different ways, leading to different split approximations. One Ducros et al. split-type approximation of the gas dynamics flux derivative that will be used in this study is given by

$$\mathbf{F}_x|_{x=x_j} \approx \begin{pmatrix} \frac{1}{2}D\rho_j u_j + \frac{1}{2}\rho_j Du_j + \frac{1}{2}u_j D\rho_j \\ \frac{1}{2}D\rho_j u_j^2 + \frac{1}{2}\rho_j u_j Du_j + \frac{1}{2}u_j D\rho_j u_j + Dp_j \\ \frac{1}{2}D\rho_j u_j v_j + \frac{1}{2}\rho_j v_j Du_j + \frac{1}{2}u_j D\rho_j v_j \\ \frac{1}{2}D\rho_j u_j w_j + \frac{1}{2}\rho_j w_j Du_j + \frac{1}{2}u_j D\rho_j w_j \\ \frac{1}{2}Du_j(e_j + p_j) + \frac{1}{2}u_j D(e_j + p_j) + \frac{1}{2}(e_j + p_j)Du_j \end{pmatrix}, \tag{29}$$

which, by (27), can be written in conservative form with numerical flux function

$$\mathbf{H}_{j+1/2} = \frac{1}{2}\sum_{k=1}^{p} \alpha_k^{(p)} \sum_{m=1}^{k-1} \begin{pmatrix} (\rho_{j-m} + \rho_{j+k-m})(u_{j-m} + u_{j+k-m}) \\ (\rho_{j-m}u_{j-m} + \rho_{j+k-m}u_{j+k-m})(u_{j-m} + u_{j+k-m}) + p_{j-m} + p_{j+k-m} \\ (\rho_{j-m}v_{j-m} + \rho_{j+k-m}v_{j+k-m})(u_{j-m} + u_{j+k-m}) \\ (\rho_{j-m}w_{j-m} + \rho_{j+k-m}w_{j+k-m})(u_{j-m} + u_{j+k-m}) \\ (e_{j-m} + p_{j-m} + e_{j+k-m} + p_{j+k-m})(u_{j-m} + u_{j+k-m}) \end{pmatrix}. \tag{30}$$

The more compact notation introduced in (28) allows (30) to be rewritten as

$$\mathbf{H}_{j+1/2} = \begin{pmatrix} \Theta_{j+1/2}^{(p)}(\rho, u) \\ \Theta_{j+1/2}^{(p)}(\rho u, u) + \Theta_{j+1/2}^{(p)}(p, 1) \\ \Theta_{j+1/2}^{(p)}(\rho v, u) \\ \Theta_{j+1/2}^{(p)}(\rho w, u) \\ \Theta_{j+1/2}^{(p)}(e+p, u) \end{pmatrix}. \tag{31}$$

Unlike the linearized and symmetrized system of Euler equations, where the split approximations lead to a stability estimate, there is no such stability estimate for the $2p$th-order accurate conservative Ducros et al. splitting. However, since the Ducros et al. splitting results in a conservative scheme, it is applicable for problems containing discontinuities.

10.6. Special Class of Entropy Conserving SPM—Entropy Split Method (Entropy Splitting Approach)

One class of SPM that the authors have been developing is the entropy split method for the compressible Euler flux derivatives. The entropy split method was originally denoted as the **"Entropy Spitting Approach"** [17,26]. This is a less-known skew-symmetric splitting for the Euler equation of gas dynamics [26,178,181]. This skew-symmetric splitting made use of Harten's symmetrizable form of the Euler equations in terms of the entropy variables [174]

to obtain a semi-discrete splitting of the Euler equations with a discrete entropy stability (in space) by the summation-by-parts approach. The entropy splitting is written in terms of the sum of a conservative portion and a nonconservative portion. If central (classical central, Padé or DRP) discretizations are used for the interior scheme (interior grid points) and a summation-by-parts boundary scheme (boundary points), it can be proved that the resulting split method is entropy conservative and entropy stable. See the recent result by Sjögreen and Yee [3,11,12,14,15,29,30,64,65]. During the entropy splitting development, the Harten [174] and the Gerritsen and Olsson entropy splitting forms incorrectly selected the un-physical branch of the inequality and were later corrected by Yee et al., hereafter referred to as the entropy splitting of the Euler equations. It is considered to be a semi-conservative splitting except at the boundary grid points. The entropy splitting of Olsson and Oliger, Gerritsen and Olsson, and Yee et al. [26,178,181] is a splitting of a form that is more suitable for the discrete stable energy norm estimate technique, including boundary scheme estimate for arbitrary order of central spatial schemes. See Yee et al. [26] for the formulation.

Consider the 1D Euler equations with inviscid flux derivative $\mathbf{F}(\mathbf{U})_x$ for a perfect gas. For extension to multi-D in a time-varying deforming grid, see [17,26,184]. The inviscid flux derivative is split into the following via the entropy variables W discussed in Harten [174].

$$\mathbf{F}_x = \frac{\beta}{\beta+1}\mathbf{F}_x + \frac{1}{\beta+1}\mathbf{F}_W W_x, \ \ \beta \neq -1 \tag{32}$$

$$W = [w_1, \ w_2, \ w_3, \ w_4, \ w_5]^T = \frac{p^*}{p}[e + \frac{\alpha-1}{\gamma-1}p, \ -\rho u, \ -\rho v, \ -\rho w, \ \rho]^T, \tag{33}$$

where

$$p^* = -(p\rho^{-\gamma})^{\frac{1}{\alpha+\gamma}} \tag{34}$$

and

$$\beta = \frac{\alpha+\gamma}{1-\gamma}, \ \ \alpha > 0 \ \text{ or } \ \alpha < -\gamma. \tag{35}$$

See Yee et al. [9,25,26] for the formulation, the choice for β and early numerical examples.

In the original entropy splitting method, the (**Entropy Splitting Approach**), the Euler flux derivatives approximation as a sum of a conservative portion and a non-conservative portion in conjunction with summation-by-parts (SBP) difference boundary closure [58] of Olsson and Oliger, Gerritsen and Olsson, and Yee et al. [26,178,181] are not written in the usual numerical flux form. Yee at al. and Vinokur and Yee [17,26] re-examined the split form of the Euler flux derivative by Harten, Olsson and Oliger, and Gerritsen and Olsson [174,178,181], to select the physical relevant branch of the split parameter β. They extended the entropy split form to include a thermally perfect gas for moving curvilinear grids [17,26,184]. In addition, they performed a detailed study that applied high-order spatial central discretization on the entropy splitting form of the Euler flux derivatives and compared it with the un-split form. It was shown that the split form of the Euler flux derivatives is more stable than the unsplit form for longer time integration without the need of added numerical dissipation. In [11], DRP (dispersion relation-preserving) finite discretizations [182,185–188] were also applied to the entropy split form of the Euler flux derivatives and with a similar gain in numerical stability. Here, the various high-order methods resulting from applying classical spatial central, DRP and Padé methods to the split form of the Euler flux derivative are referred to as entropy split methods as a function of the splitting parameter β. These entropy split methods are entropy conserving and stable but they are usually not conservative numerical methods without additional reformulation, as proposed in, e.g., Sjögreen and Yee [3,12,13,15,16,30,189].

The entropy split methods and other SPM high-order skew-symmetric splitting of the inviscid Euler or ideal MHD flux derivative formulation of any even order can be found in [12,13,15]. Most of the skew symmetric splittings are not entropy conserving numerically. Some of them are momentum conserving or kinetic energy preserving numerically, see [45,

158,179,180]. See [3,12,13,15,16,30,189] for additional development for the compressible Euler and ideal MHD equations.

Other Entropy Conserving Methods for the Compressible Euler and Ideal MHD Equations

The entropy-conserving method by Tadmor [175,190] is the method of choice for rapidly developing unsteady flows, especially in development of unstructured grid methods (e.g., DG method). Our work on typical test cases using the FDM formulation found that the Tadmor entropy conserving method [175,190] of the same order requires twice the arithmetic operations than the entropy split methods. In addition, Harten's entropy function can be part of a Tadmor-type entropy conserving method family [12,65] with similar accuracy and stability. Comparisons among the methods can be found in [3,11,12,30,65].

10.7. Newer Class of Entropy Split Methods in Numerical Flux Form: Not Relying on Homogeneous Property of the Inviscid Flux and Symmetrizable Inviscid Flux Derivatives

In 2019, Sjögreen and Yee [15] derived a high-order conservative numerical flux for the non-conservative portion of the entropy splitting of the Euler flux derivatives by taking advantage of the homogeneity property of the inviscid flux and symmetrizable inviscid flux derivatives. Due to the construction, this conservative numerical flux requires more arithmetic operations and is less stable than the original entropy split method (not fully conservative). An alternative simple approach for problems containing shock waves is to use a shock detector to switch the entropy split discretization to a standard centered approximation in the neighborhood of shock waves to avoid wrong shock speed.

Instead of taking advantage of the homogeneity property of the inviscid flux and symmetrizable inviscid flux derivatives, a wider class of entropy split methods that do not require the homogeneous property were developed, see our 2022 paper [16]. The formulation is written in standard numerical flux form. This wider class of entropy split method was extended for the equations of ideal MHD by the authors in [16].

It is our assessment that employing high-order SPM non-dissipative methods in conjunction with the nonlinear filter approach should be a method of choice for high-resolution simulations involving compressible turbulence up to mildly supersonic regimes. For turbulence with shocks, there is an even larger gain both in the accuracy and CPU time of the nonlinear filter schemes over their standard WENO counterparts.

Forms of the structure-preserving (SPM) numerical fluxes that belong to the class of skew-symmetric splitting of the inviscid flux derivatives in curvilinear grids are given in [16,30]. Depending on the type of flow physics, high-order central, DRP or Padé methods are applied to the skew-symmetric split form of the inviscid flux derivative as the baseline method before the post-processing nonlinear filter step, if needed, especially for problems with shocks. Selected methods with multiple structure-preserving properties are given with numerical examples.

10.8. A Complex 3D Supersonic Shock-Turbulence Interaction by a Physics-Preserving Nonlinear Filter Method [4]

The 3D supersonic shock-turbulence interaction is a more challenging test case and is a very CPU intensive computation with long transient simulation before obtaining meaningful turbulent statistics. The 3D test case considered here concerns an initial turbulence disturbance at the inflow boundary interacting with a stationary supersonic planar shock wave. The problem has been studied by previous investigators, mainly related to DNS computations; see e.g., [191–193]. Here, we choose the configuration considered in the DNS study of [192]. Figure 49 shows a schematic of the problem setup. The computational domain is $-2 \leq x \leq -2 + 4\pi$, $0 \leq y \leq 2\pi$ and $0 \leq z \leq 2\pi$. The grid is uniform in all directions with the spacing in x being several times finer than in y and z (see [192] for explanation). We solve the filtered governing equations in a non-dimensional form. The Yee et al. nonlinear filter scheme with the Ducros et al. flow sensor [170] is used for integration of the Ducros et al. [158] split form of the governing equations. The spatial

base scheme is the eighth-order central differencing and the nonlinear filter scheme is the dissipative portion of the seventh-order WENO scheme (WENO7). This nonlinear filter scheme, including the Ducros et al. splitting of the governing equation, is denoted by WENO7fi + split (or WENO7fi for ease of discussion). Since the initial data consist of a planar shock in the x-direction, numerical dissipation should be mainly needed in the x-direction. In order to obtain more accurate results, WENO dissipation is employed only in the x-direction at the postprocessing stage of the Yee et al. nonlinear filter. The inflow and outflow boundary conditions are applied in the streamwise direction and periodic boundary conditions are applied in the transverse directions.

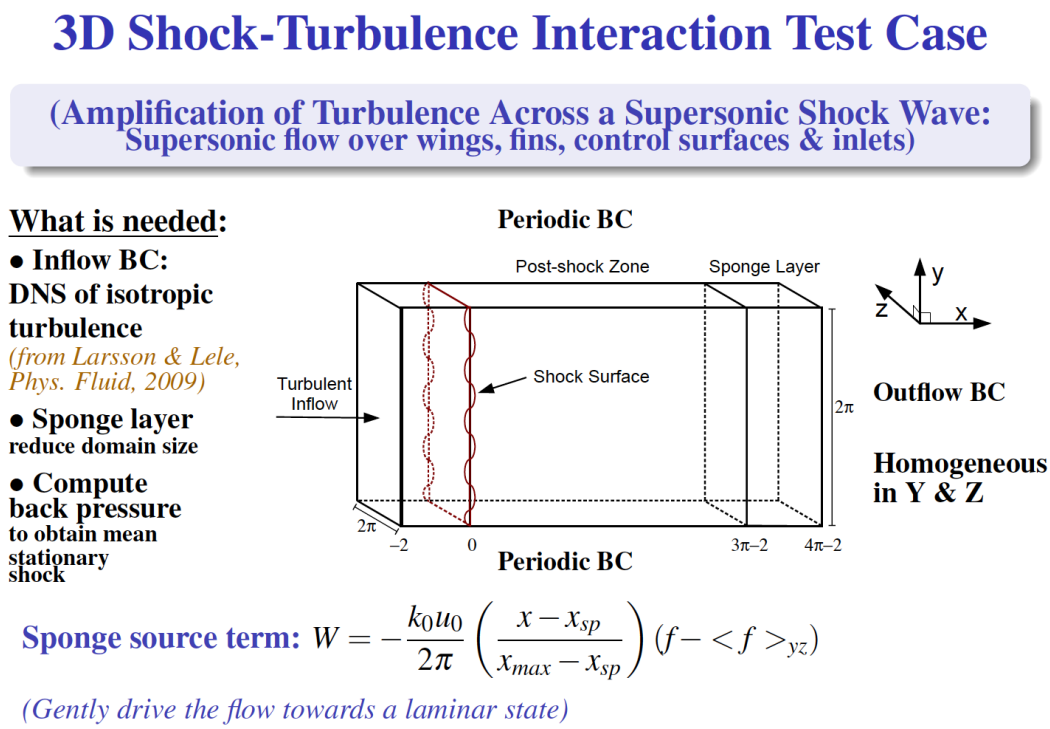

Figure 49. Three-dimensional supersonic shock-turbulence interaction test case.

Inflow boundary condition. A fully developed turbulent inflow condition is applied using a turbulent database. This database is generated as follows. First, an initial isotropic turbulent field with the energy spectrum $E(k) \sim k^4 \exp(-2k^2/k_0^2)$ and microscale Reynolds number $Re_\lambda = \rho\lambda u'_{rms}/\mu = 140$ is generated using the methodology described in Ristorcelli and Blaisdell [194]. Here, the energy peak wavenumber $k_0 = 4$ is used. Next, the decay of this field in a periodic box is simulated for approximately three eddy turnover times $\tau = \lambda/u'_{rms}$ to ensure fully developed turbulence. After the decay, the Reynolds number $Re_\lambda = 40$ and the turbulent Mach number $M_t = \overline{u'_i u'_i}^{1/2}/c_0 = 0.16$. Here, c_0 is the mean speed of sound. The generated isotropic turbulence is introduced at the inflow boundary with constant mean velocity u_0. We consider two cases with mean flow Mach numbers $M = 1.5$ and $M = 3.0$. In order to compare the DNS results, we use the inflow database from [192].

Outflow boundary condition. In order to avoid acoustic reflections of subsonic flow from the outflow boundary, a non-reflective sponge layer is employed on the region near the outflow. The length of this layer is $x_{max} - x_{sp} = \pi$. The sponge layer is implemented by introducing the following source term into the equations:

$$\Omega = -\frac{k_0 u_0}{2\pi}\left(\frac{x - x_{sp}}{x_{max} - x_{sp}}\right)(f - < f >_{yz}), \tag{36}$$

where $f = \rho, \rho u_i, \rho E$ and $\langle \cdot \rangle_{yz}$ denotes averaging in the y- and z-directions.

The outflow pressure p_∞ is chosen such that the mean shock location is stationary. For laminar flow, Rankine–Hugoniot conditions give

$$\frac{p_\infty}{p_0} = 1 + \frac{2\gamma}{\gamma+1}\left[\frac{(u_0 - U_s)^2}{c_0^2} - 1\right], \tag{37}$$

where p_0 is the inflow mean pressure, u_0 is the mean inflow velocity, c_0 is the mean inflow speed of sound and U_s is the shock velocity. As the inflow condition is turbulent, the Rankine–Hugoniot conditions are valid only instantaneously but not on average. After an initial guess based on (37), the outflow pressure is refined by an iteration procedure, integrating the governing equations on a coarse grid and updating the pressure according to the formula

$$p'_\infty = p_\infty + 4U_s\rho_u u_0/(\gamma+1). \tag{38}$$

See [192] for more details.

To illustrate an instantaneous turbulent pattern, Figure 50 shows the instantaneous velocity field u_x (top) and u_y (bottom) at a slice where z = const, obtained with DNS on a grid of 1553×256^2 points. A turbulent flow enters over the left boundary at Mach 1.5. The turbulence interacts with a quasi-steady shock wave near the inflow boundary. The figure shows the x- and y-directions velocity field in a $z = const.$ slice of the three-dimensional computational domain. See [4] for details of the problem set up and method comparisons. The numerical method is an eighth-order accurate non-dissipative method together with an adaptive nonlinear filter by a dissipation portion of the seventh-order positivity preserving WENO7 of Zhang and Shu [160] (WENO7Pfi). The Ducros et al. skew-symmetric splitting is the structure-preserving eighth-order central spatial discretization. The turbulent Mach number is 0.16. The incoming turbulence causes wrinkles in the shock front. The classical fourth-order Runge–Kutta method (RK4) is used as temporal discretization. Grid refinement and comparison of standard high-order shock-capturing methods with the high-order structure-preserving nonlinear filter method were performed in [4].

The comparison between the filtered DNS data and the results obtained with different numerical schemes on the coarse grid with 389×64^2 points and $M = 3$ is shown in Figure 51. Here, we compare the results obtained by the fifth-order WENO (WENO5) and WENO7 with the results obtained by the filter counterpart of WENO7 with Ducros et al. splitting of the governing equations (WENO7fi+split). The comparison of WENO5, WENO7 and WENO7fi+split is shown in Figure 52. For Figure 52, each of the considered schemes is employed in all three directions. The solution by WENO7fi is closer to the filtered DNS solution than WENO5 and WENO7. WENO5 is far too dissipative for DNS computation with this coarse grid. Figure 53 shows the velocity spectrum of DNS by WENO7fi with $M = 3$, sliced at $x = 0$: four-level DNS grid refinement study on grids with 389×64^2, 777×128^2, 1553×256^2 and 2329×256^2 points.

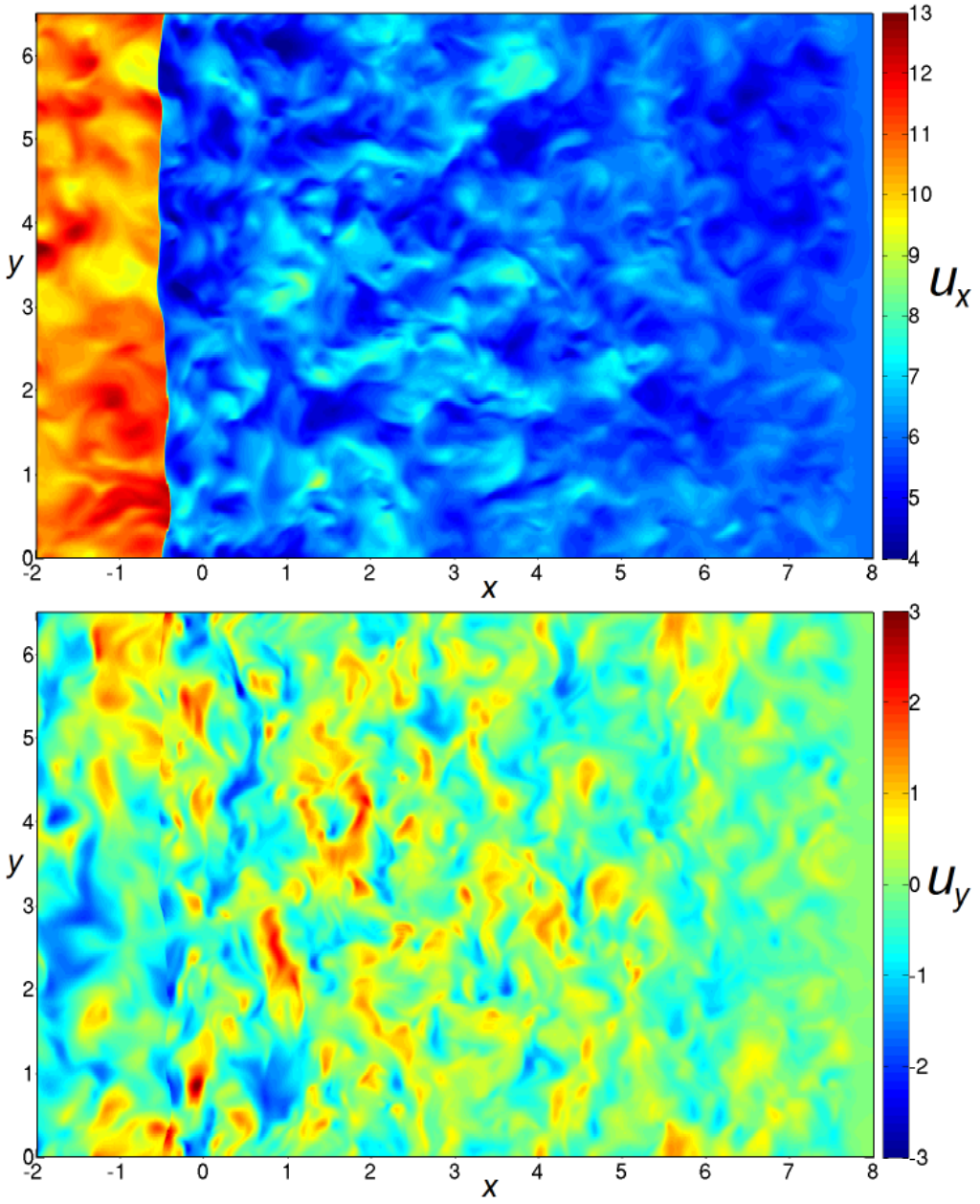

Figure 50. Instantaneous velocity field u_x (top) and u_y (bottom) obtained with DNS on grid of 1553×256^2 points. Slice $z = \text{const}$.

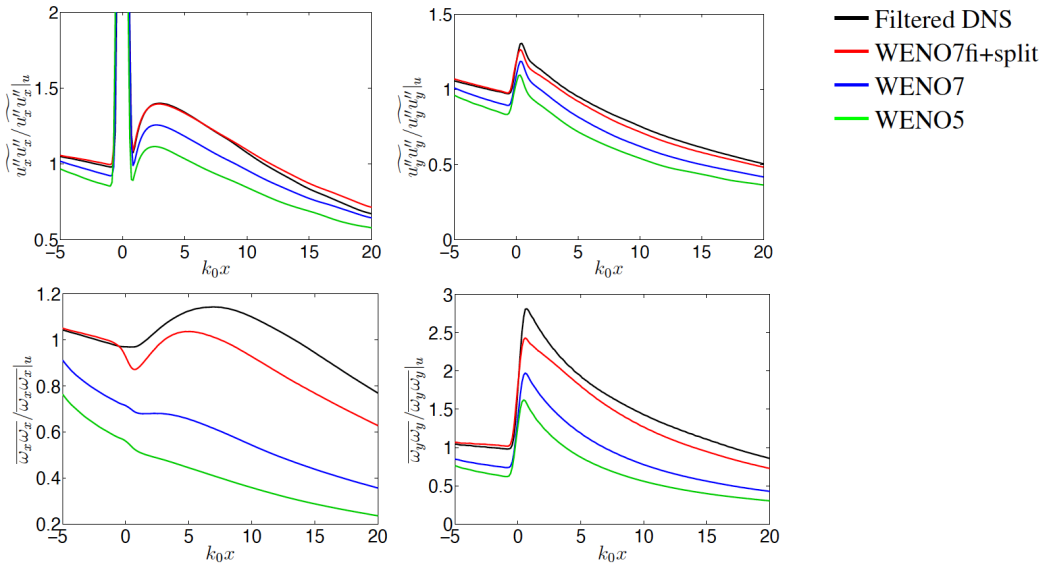

Figure 51. DNS, WENO5, WENO7 and WENO7fi method comparison: Comparison to filtered DNS data of the statistics obtained by the different numerical schemes on grid 389×64^2, $M = 1.5$. Top row: streamwise (**left**) and transverse (**right**) Reynolds stress components. Bottom row: streamwise (**left**) and transverse (**right**) vorticity components.

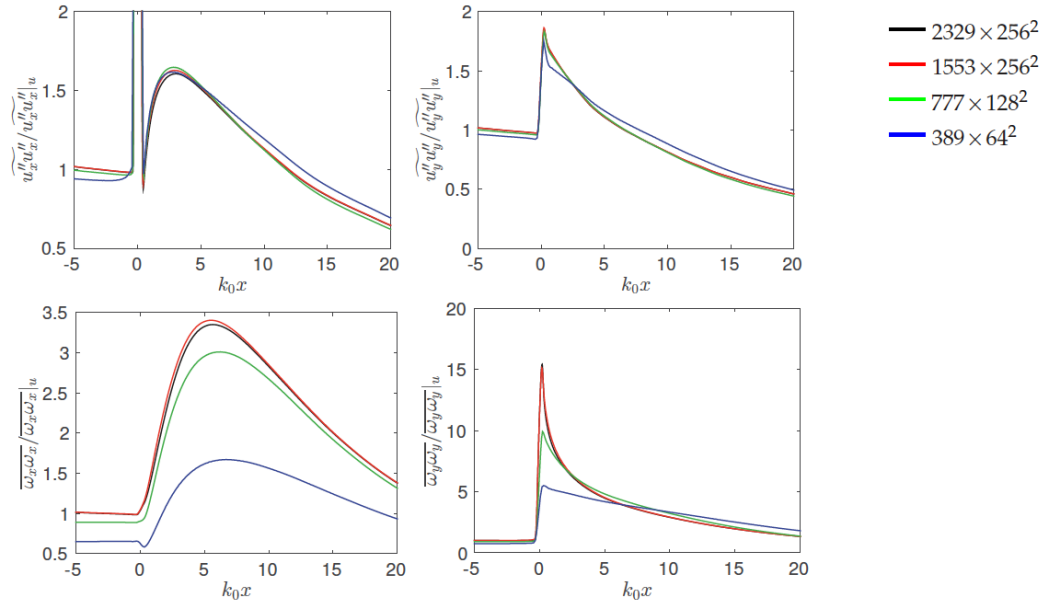

Figure 52. DNS, WENO7fi, M = 3: Four-level DNS grid refinement study on grids with 389×64^2, 777×128^2, 1553×256^2 and 2329×256^2 points. Top row: streamwise (**left**) and transverse (**right**) Reynolds stress components. Bottom row: streamwise (**left**) and transverse (**right**) vorticity components.

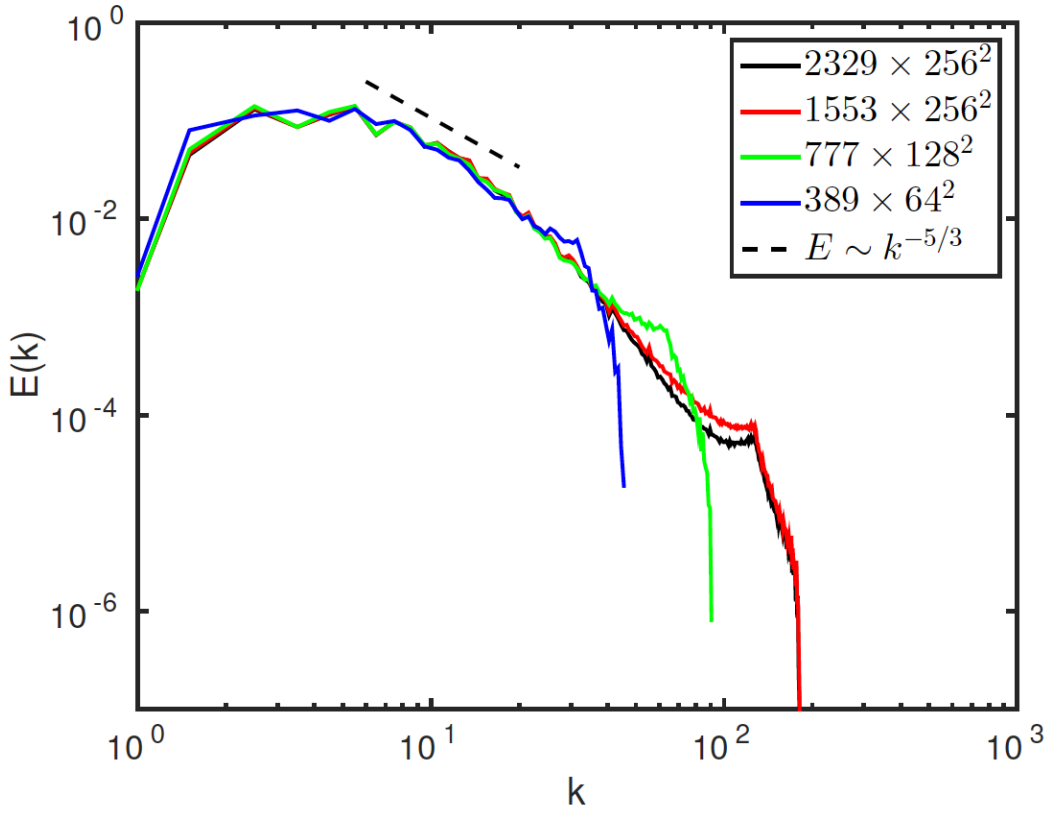

Figure 53. DNS, WENO7fi, $M = 3$, velocity spectrum, slice at $x = 0$: four-level DNS grid refinement study on grids with 389×64^2, 777×128^2, 1553×256^2 and 2329×256^2 points.

11. High-Order Skew-Symmetric Physical-Preserving Methods (SPM) Comparison for Gas Dynamics

For MHD computation and using the extension of our new entropy split method for the equation of ideal MHD, see [16,30]. Here, some test cases comparing a set of high-order structure-preserving methods for compressible gas dynamics will be given in this section. Nomenclature for these method comparisons are defined below.

11.1. Various Structure-Preserving Properties Nomenclature

For test cases comparison, the high-order spatial structure-preserving methods considered are as follows:

- ECHKP: Entropy conserving using the Harten class of entropy functions $E_H = -\frac{\gamma+\alpha}{\gamma-1}\rho(p\rho^{-\gamma})^{\frac{1}{\alpha+\gamma}}$ [174,175]. It turned out that this method in its base form also satisfies Ranocha's kinetic energy preservation condition (KEP), so there is only one variant for this method [46,65].
- ECLOG: Tadmor-type entropy-conserving method using the Tadmor entropy function $E_L = -\rho \log(p\rho^{-\gamma})$.
- ES: Skew-symmetric splitting of the inviscid flux derivative that is entropy conserving and stable using the Harten entropy function [174] and the generalized energy norm with summation-by-parts (SBP) [12,26,64].
- DS: Momentum-conserving Ducros et al. skew-symmetric split of the inviscid flux derivative [158].
- KGP: Kennedy–Gruber–Pirozzoli (KGP) skew-symmetric splitting of the inviscid flux derivative that is kinetic energy preserving [45,179,180].
- ESDS: Entropy split with Ducros et al. splitting [12].
- ESSW: Entropy split with Ducros et al. splitting but switch to regular central near discontinuities [15].

- ECLOGKP: Tadmor-type entropy conserving method using the Tadmor entropy function with Ranocha's kinetic energy preserving modification [46].
- DSKP: Ducros split with KEP.

From our previous studies [12,13,15], the Tadmor-type entropy conserving methods EC, ECLOG and ECLOGKP are the most CPU intensive methods among the nine methods. For results by EC, see [12,13,15]. It is approximately twice the CPU per time step than the ES, ESDS and ESSW methods. DS is the least CPU intensive. Comparisons of execution times were given in previous published works.

See [12,13,15] for more test case comparisons, including strong shock waves. Here, only the 2D isotropic vortex convection, 3D Taylor–Green vortex shock free turbulence and the Brio-Wu MHD shock tube test cases are selected for the nine method comparison. The comparison includes the maximum-norm error, mass conservation errors, entropy and kinetic energy vs. time for the eighth-order methods. It is noted that the performance comparison discussed here pertains to the chosen flow type, governing equation set and uniform grid spacings without any grid adaptation. The performance of the entropy split methods as a function of the split parameter β for other test cases can be found in our previous published works indicated above. Just like other current high-order method developments in the literature, the performance of the entropy split method is highly dependent on the grid size, flow type, flow condition, shock-free turbulence, turbulence with shocklets and turbulence with strong shocks. Below, only results by the eighth-order classical spatial discretization are shown. Studies by DRP and compact spatial discretizations were also performed but are not shown here. See [12–15,29] for additional investigations.

11.2. A Smooth Flow Gas Dynamics Test Case: 2D Isotropic Vortex Convection

A standard test case to examine the stability and accuracy of long-time integration for a smooth flow is the 2D isentropic vortex convection with the initial data indicated in Figure 54.

2D Isentropic Vortex Convection

(Inviscid, pure convection of the IC)

Computational Domain: Period BC, $0 \le x \le 18, 0 \le y \le 18$

Initial Condition:

$$\rho(x,y) = ((1 - \frac{(\gamma-1)\beta^2}{8\gamma\pi^2} e^{1-r^2})^{\frac{1}{\gamma-1}}$$

$$u(x,y) = u_\infty - \frac{\beta(y-y_0)}{2\pi} e^{(1-r^2)/2}$$

$$v(x,y) = v_\infty + \frac{\beta(x-x_0)}{2\pi} e^{(1-r^2)/2}$$

$$p(x,y) = \rho(x,y)^\gamma,$$

$$r^2 = x^2 + y^2, \beta = 5, \gamma = 1.4, u_\infty = 1, v_\infty = 0.$$

Figure 54. Two-dimensional isentropic vortex convection problem setup.

The exact solution is the initial data translated, $\mathbf{u}(x,t) = \mathbf{u}_0(x - u_\infty t, y - v_\infty t)$. The computational domain was of size $0 \leq x \leq 18$, $0 \leq y \leq 18$ with periodic boundary conditions. The center of the vortex is $(x_0, y_0) = (9,9)$. We integrate this test case to a final time $T = 800$ for a majority of the comparisons. Two grids 101^2 and 201^2 are considered for the comparison. For $\beta = 2$ and the coarse grid 101^2, we integrate to a final time $T = 1440$, which is more than 100 times longer than reported in the literature and twice as long as most of our previous studies with end time 720. To obtain a better time accuracy, the CFL number is set to 0.4, leading to a fairly small time step.

Investigating the level of maximum-norm error by the eighth-order ES and ESSW methods as a function of β vs. time using the two grids, Figure 55 shows that a lower maximum-norm error can be prolonged for longer time integration using $\beta = 1$ than $\beta = 2$ by the finer grid for both ES and ESSW methods. For the same grid, the maximum-norm error is highly dependent on the value of β. The error remains the same for $\beta = 1$ by both ES and ESSW methods. However, for other $\beta = 2$ and 2.5, the error using the ES method is slightly different from the ESSW method.

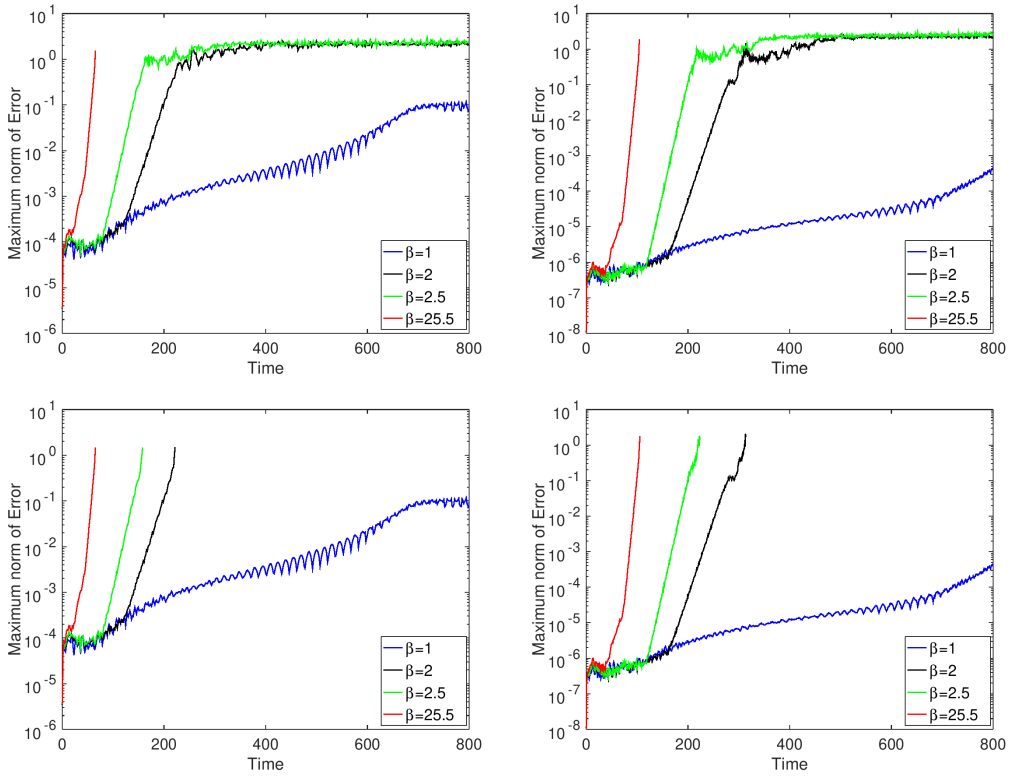

Figure 55. Two-dimensional inviscid isentropic vortex convection: Comparison of maximum-norm error vs. time for different β by eighth-order ES (**top**) and ESSW (**bottom**) using 101^2 (**left**) and 201^2 (**right**) grid points.

Figure 56 shows the maximum-norm error, mass conservation errors, entropy and kinetic energy for the nine eighth-order methods using $\beta = 1$ on the fine grid. Overall, ES performs the best, except the conservation of mass breaks down at around time 680. The kinetic energy and entropy results show the quantity with its value at time zero subtracted, e.g., the kinetic energy ($E_{kin(t)}$) shown is $E_{kin}(t) - E_{kin}(0)$.

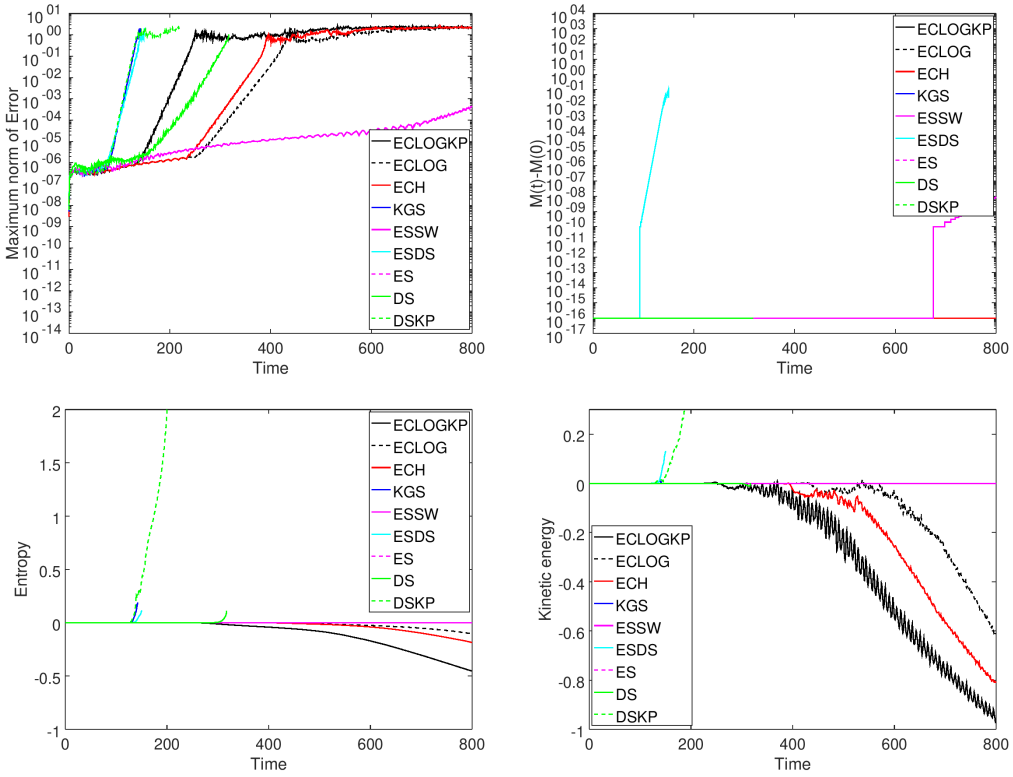

Figure 56. Two-dimensional inviscid isentropic vortex convection: comparison of maximum-norm error, mass conservation error, entropy errors and kinetic energy by E_H vs. time for the nine eighth-order methods using a fine 201^2 grid points and $\beta = 1$.

To show the performance of $\beta = 2$, Figure 57 shows the time-evolution to the final end time of $T = 1440$ using the coarse grid 100^2 in terms of maximum-norm error, the two entropies and the kinetic energy as function of time for eight methods using $\beta = 2$ in the entropy split methods. The performance by the ES method using $\beta = 2$ is very different to using $\beta = 1$ using the same grid.

The entropy E_L shows the quantity with its value at time zero subtracted. The methods KGS, DS and ESDS blow up before time 300, while the four methods that conserve entropy all run to the final time. However, the methods that do not blow up have very large errors after time 300.

From the computed results (not all results are shown here), the entropies are not perfectly conserved for longer times. The likely explanation is that the poor accuracy for long times makes time discretization error significant. This, in turn, destroys the conservation when entropy conservation holds only for the semi-discrete problem. However, as seen from the zoomed-in plots, the entropy and kinetic energy are very close to being constant, up to the time when the errors become large. This is an improvement that we expected to see with the more accurate time integration.

Extensive method comparisons were conducted in [12,13,15,30]. Results by ES and ESDS are highly dependent on the split parameter β. Only comparisons using $\beta = 1$ and $\beta = 2$ based on the study in [12] are shown here. Using $\beta = 1$ with grid refinement, the performance by ES is stable and more accurate for a longer time integration. In summary, for the 2D vortex convection case, ESDS, ESSW and KGP methods conserve entropy in a shorter time integration and are less accurate for longer time integration than the other considered methods. For ESDS and ESSW, modification from the original ES method might interfere with the entropy conservation property.

For the splitting parameter β, even for shock-free long-time integration flows, for physical argument, it is preferred to use $\beta = 1$ or greater as for $\beta < 1$, more than 50% non-conservative portion of the split flux derivative is used.

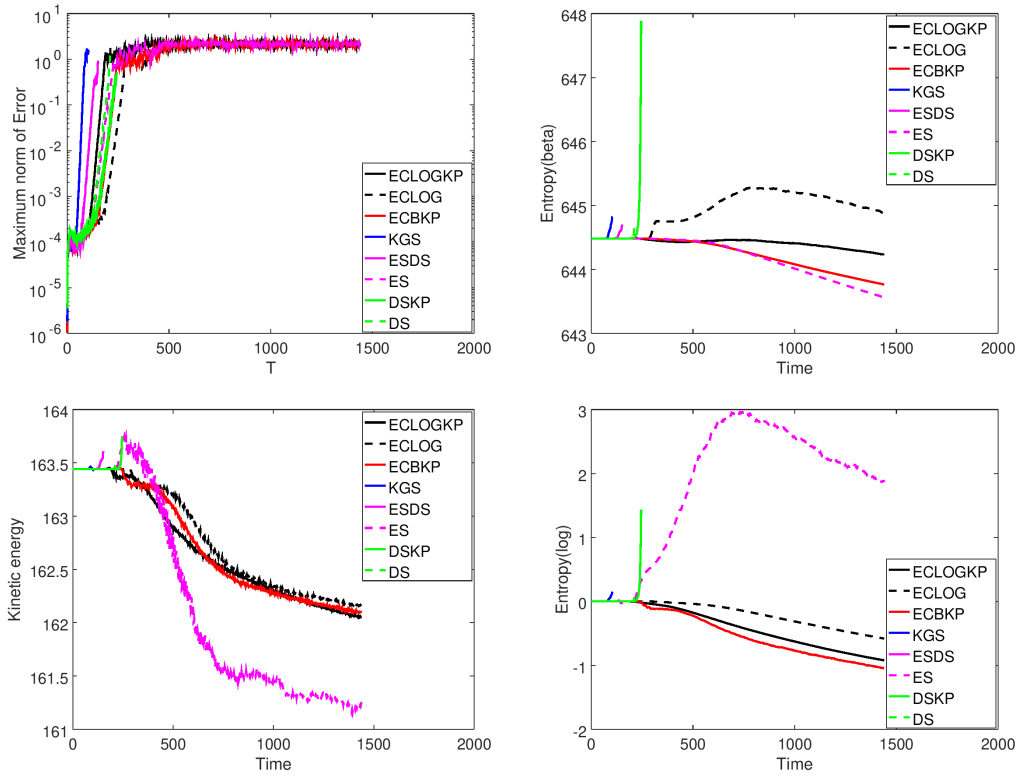

Figure 57. Two-dimensional inviscid isentropic vortex convection: Final end time of $T = 1440$ comparison of maximum-norm error, entropy E_H, entropy E_L and kinetic energy vs. time for the eight eighth-order methods using a 100^2 grid points and $\beta = 2$.

11.3. A Well-Known 3D Shock-Free Compressible Turbulence Gas Dynamics Test Case—3D Taylor–Green Vortex

The well-known shock-free compressible turbulence test case to evaluate the stability and accuracy for gas dynamics is the Taylor–Green vortex [195]. The 3D Euler equations of compressible gas dynamics are solved with $\gamma = 5/3$. The computational domain is a cube with sides of length 2π and with periodic boundary conditions in all three directions. The initial conditions are

$$\rho = 1 \quad p = 100 + \{[\cos(2z) + 2)(\cos(2x) + \cos(2y)] - 2\}/16 \tag{39}$$

$$u = \sin x \cos y \cos z, \quad v = -\cos x \sin y \cos z, \quad w = 0. \tag{40}$$

The problem is solved to time 20. In our previous studies, the uniform coarse grid DNS of 64^3 grid points solutions were compared with the filtered fine grid DNS solutions using a uniform 256^3 grid points. Here, we use the same uniform coarse grid to examine the nonlinear stability and accuracy of the three new eighth-order NEW, ESSW and ESDS methods. The total kinetic energy of the exact solution is constant in time.

Although grid refinement studies were performed and reported in [12,13,15,30], here, we only report the numerical results for a coarse grid DNS comparison among methods. It is noted that for this Taylor–Green inviscid problem, small scales are generated that eventually cause large errors in the solution due to inadequate resolution. This probably occurs around $T = 5$. Another issue is that for very low dissipative or non-dissipative numerical methods for the simulation of turbulent flows, even with extreme grid refinement, grid convergence cannot be obtained as the original inviscid Euler equations are chaotic in nature. With sufficient but not excessive numerical dissipations, one is solving the equivalent of very high Reynolds number Navier–Stokes equations. See Yee and Sjögreen [196] for a study. The end time is 20 instead of the standard end time 10 to observe the solution behavior twice as long using the same RK4 time discretization and CFL number 0.4. Harten's entropy

was used for all schemes except ECLOG and ECLOGKP, where we used the log-entropy. Furthermore, the entropy $E(t)$ is normalized to show deviation from the initial entropy. Thus, $E(t) - E(0)$ is shown in the figures.

Figure 58 shows the comparison of kinetic energy, maximum-norm error and entropy vs. time for the nine eighth-order methods. It is interesting to see the behavior of doubling the time integration duration for such coarse grid DNS computations.

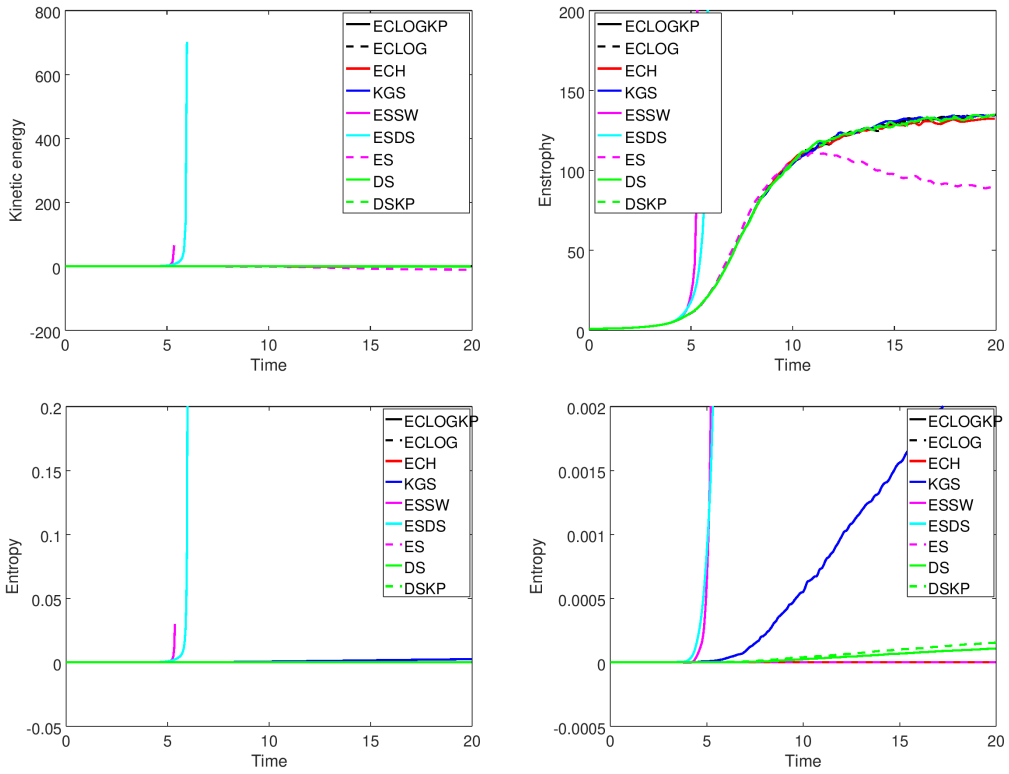

Figure 58. Three-dimensional inviscid Taylor–Green vortex using 64^3 grid points: Comparison of kinetic energy (**top left**), enstrophy (**top right**), entropy (**bottom left**) and entropy (closed up, **bottom right**) vs. time for the nine eighth-order methods using $\beta = 2$.

Method ESDS becomes unstable at around time 6, and method DSKP becomes unstable around time 7. All other schemes ran to completion. Again, the kinetic energy and entropy results show the quantity with its value at time zero subtracted, e.g., the kinetic energy ($E_{kin(t)}$) shown is $E_{kin}(t) - E_{kin}(0)$. The ES method starts to lose some energy at a later time. Otherwise, the stable results are similar. ECLOGKP and KGS are indistinguishable and fall on top of each other in the zoomed-in figure. One surprising result is that method ECBKP is expected to preserve kinetic energy in the same manner but does not. The other stable methods are a little off, but this is only visible in the closeup. Methods ES and ECBKP fall on top of each other, as we would expect, since these two schemes conserve the entropy in a discretized sense. Method ECLOGKP is also on top of ES and ECBKP, making it hard to visualize the differences in the results.

Not included here are studies illustrating that the logarithmic entropy function conserved Harten's entropy almost perfectly. Methods ECLOGKP and ECLOG conserve entropy, as illustrated in the figure, where their solutions are on top of each other. Overall, ECLOGKP, ECLOG, ECBKP, KGS and DS are very similar. One has to zoom in very much in this region to see any differences for this test case. However, differences might be larger for other flow problems. As can be seen for this test case, method ES behaves somewhat different. DSKP and ESDS are not performing well. It is noted again that results by ES and ESDS are highly dependent on β. Only results with $\beta = 2$ are shown based on the study in [12].

Figure 59 compares how well these eighth-order methods conserve mass and momentum in the x-, y- and z-directions. The figures show total mass (or momentum) as a function of time, normalized so that the initial mass (or momentum) is zero. For the mass-conservation plot, all schemes except ES, ESSW and ESDS are perfectly conservative. The normalized $M(t) - M(0)$ is zero as long as the method is stable for all methods except the ES scheme, which is around e^{-9} for most of the time. In addition, these figures are shown in the log-scale, where we artificially set the schemes with zero conservation error to e^{-16}.

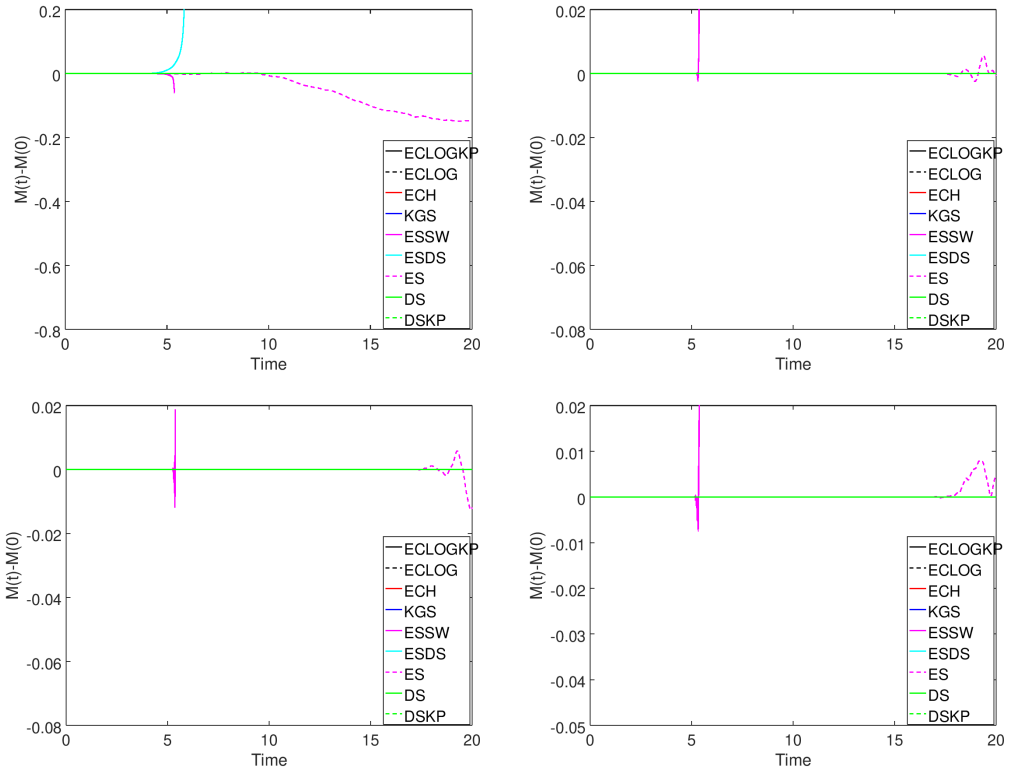

Figure 59. Three-dimensional inviscid Taylor–Green vortex using 64^3 grid points: comparison of mass conservation (**top left**), x-momentum conservation (**top right**), y-momentum conservation (**bottom left**) and z-momentum conservation (**bottom right**) vs. time for the nine eighth-order methods using $\beta = 2$.

The Taylor–Green vortex test case has a similar method comparison conclusion as the vortex convection test case. ESDS, ESSW and KGP methods conserve entropy in a shorter time integration and are less accurate for longer time integration than the other considered methods. For ESDS and ESSW, their modification from the original ES method might interfere with the entropy conservation property.

For the extension of these high-order methods for the ideal MHD in curvilinear grids with method comparisons, see [30].

Only the key numerical results of a very difficult Brio–Wu MHD shock tube problem is briefly discussed here. The Brio–Wu MHD shock tube problem involves two fast rarefaction waves, a slow compound wave, a contact discontinuity and a slow shock wave. According to the Flash code [197,198], standard high-order shock-capturing methods exhibit oscillatory solutions. Examples are PPM (piecewise parabolic method of Collela and Woodward [199]) and third- to fifth-order WENO (WENO3–WENO5). Most researchers resorted to use first order or very diffusive second-order methods with local Lax–Freidrichs (LLF) or variants of the HLL-type numerical fluxes [200,201]. The oscillations increase with an increase in B_y, with the reason being that stronger B_y introduces a more transverse effect that resists shock propagation in the x-direction, causing the shock to move slowly. Our simulation using our

high-order method provides higher accuracy with decreased oscillation at the discontinuity regions than the Flash code results. Details of the test case can be found in [16,30].

11.4. A Short Summary of Comparative Performance of High-Order Skew-Symmetric SPM

In summary, for the chosen test cases, the long-time integration performance of the entropy split methods as a function of the split parameter β is dependent on the flow type, flow condition and the grid spacing. For finer grids, the stability of long-time integration for the same β value can be different. The general guideline is that for very smooth pure convection flows, $\beta = 1$ (50% conservative and 50% non-conservative of the split term) or β between 1 and 2 can improve the stability tremendously without added numerical dissipation. A finer grid in general prolongs stability for longer time integration. The split method conserves mass and entropy. For problems with shock waves, β between 20 and 26 performs well with the NEW and ESSW methods in conjunction with the Yee et al. and Yee and Sjögreen nonlinear filter approach.

The relative stability and accuracy are comparable among the KGP-type, DS-type split methods and the ES and ESSW methods. In certain test cases, ES and ESSW are more stable for longer time integration. KGP-type and DS-type methods are the least CPU intensive for both the gas dynamics and MHD test cases. However, they do not conserve entropy. For the difficult Brio–Wu test case, unlike most published work reported in the literature, the current nonlinear filter approach in conjunction with the various splitting methods indicated that stability and high accuracy were obtained using very high-order spatial discretization and the Roe-type approximate Riemann solver. The numerical instability and highly spurious oscillatory solutions by standard high-order shock-capturing methods are drastically reduced by the ES and ESSW methods. With the current studies and from our previous studies [12,13,15,202], EC, ECLOG and ECLOGKP are the most CPU intensive methods among the nine methods. They have at least twice the CPU usage per time step than the ES, ESDS and ESSW methods and yet exhibit similar resolutions. DS is the least CPU intensive.

For a generalization to a wider class of entropy split methods for compressible ideal MHD using the two-point numerical flux with numerical examples, see [16],

12. Concluding Remark

Some building blocks to ensure a higher level of confidence in PAR of numerical simulations have been discussed. The discussion concentrates only on how well numerical schemes can mimic the solution behavior of the underlying PDEs. The possible discrepancy between the chosen model and the real physics and/or experimental data is set aside. These building blocks are based largely on the author's view, background and integrated experience in computational physics, numerical analysis and the dynamics of numerics. They also represent the end result of the various studies with the author's collaborators indicated in the acknowledgment section. Among many other important building blocks for the PAR of numerical simulations, the author believes the following five building blocks are essential. The first building block is to analyze as much as possible the dynamical behavior of the governing equation. For stability and well-posedness considerations, whenever it is possible, it is also necessary to condition (not pre-condition) the governing PDEs before the application of the appropriate scheme (Yee and Sjögreen [121,122]). The second building block is to understand the nonlinear behavior, limits and barriers and to isolate the spurious behavior of existing numerical schemes. The third building block is to include nonlinear dynamics and bifurcation theories as an integral part of the numerical process whenever it is possible. The fourth building block is to construct appropriate adaptive spatial and temporal discretizations that are suitable for the underlying governing equation. The last building block is to construct appropriate adaptive numerical dissipation/filter controls for long-time integrations, and complex high-speed turbulent and combustion simulations (Sjögreen and Yee 2001 [10], Yee and Sjögreen 2001 [120]).

We have revealed some of the causes of spurious phenomena due to the numerics in an attempt to improve the understanding of the effects of numerical uncertainties in CFD. We have shown that guidelines developed using linearization methods are not always valid for nonlinear problems. We have gained an improved understanding of long-time behavior of nonlinear problems and the nonlinear stability, convergence and reliability of time-marching approaches. We have learned that numerics can introduce and suppress chaos and can also introduce chaotic transients. The danger of relying on DNS to closely bracket the onset of turbulence and chaos is evident.

We have shown that employing theories of nonlinear dynamics to guide the construction of more appropriate, stable and accurate numerical methods could help (a) delineate solutions of the discretized counterparts but not solutions of the governing equations; (b) prevent numerical chaos/turbulence leading to FALSE predication of transition to turbulence; (c) provide reliable numerical simulations of nonlinear fluid dynamical systems, especially by direction numerical simulations (DNS), large eddy simulations (LES) and implicit large eddy simulations (ILES) simulations; and (d) prevent incorrect computed shock speeds for problems containing stiff nonlinear source terms, if present.

From the wide varieties of test cases for compressible gas dynamics and MHD performed in [1–3], the performance of the blending of more than one method is highly dependent on the flow physics. Regardless of the choice of these blendings of high-order methods, these test cases illustrate the improved stability and accuracy over the standalone single high-order method approach. Nine eighth-order structure-preserving methods were compared for a wide range of test cases in order to illustrate the effectiveness of the blending of selected numerical method approaches. These current trends of adaptive blending of high-order, structure-preserving non-dissipative methods with high-resolution, high-order shock-capturing methods are also applicable to discontinuous Galerkin method, and finite element methods and spectral element methods. In addition, our studies indicated that these current approaches can also improved stability and accuracy in rapidly developed unsteady flows containing steep gradients, and shear and shock waves with the benefit of minimizing added numerical dissipations.

Our future work is planned to develop newer methods catering to some of the aforementioned disciplines with the knowledge gained from these nonlinear studies.

Funding: Financial support from the DOE/SciDAC program and the NASA TTT/RCA program for the first author is gratefully acknowledged. The authors are grateful to Murray Tobak, Marcel Vinokur, Karim Shariff, Dinesh Prabhu, Jasim Ahmad and Alan Wray of NASA Ames Research Center for the numerous invaluable discussions throughout the course of this work. Special thanks to W.L. Oberkampf of his support of our work in the early 2000s and all of the collaborators—A. Harten, R. F. Warming, D.V. Kotov, C.-W. Shu, P.L. Roe, A. Lafon, W. Wang, R.J. LeVeque, N.D. Sandham, J.M. Djomehri, D.F. Grififfths, A.M. Stuart, M. Vinokur, L. Keefe, J.R. Torczynski, P. Fischer, R.D. Henderson, M. Poliashenko, J.-L. Montagn'e, A.A. Wray, A. Hadjadj, A. Kritsuk, T. Magin, and M. Panesi, D.K. Prabhu, G.H. Klopfer, M.F. Barone, S.A. Morton and M.R. Visbal—during the various stages of research development. The 2nd and 3rd of this research received no external funding.

Conflicts of Interest: Author Björn Sjogreen was employed by the company MultiD Analyses AB. The work done on this work is not supported by MultiD Analyses AB, but on his own time. All authors declare that the research was conducted in the absence of any commercial or financial relationships that could be construed as a potential conflict of interest.

References

1. Yee, H.C.; Sweby, P.K. *Dynamics of Numerics & Spurious Behaviors in CFD Computations*; RIACS Technical Report 97.06; NASA AMES Research Center: Mountain View, CA, USA, 1997.
2. Yee, H.C. Building Blocks for Reliable Complex Nonlinear Numerical Simulations. In *Turbulent Flow Computation*; Drikakis, D., Geurts, B., Eds.; Springer: New York, NY, USA, 2002.
3. Yee, H.C.; Sjögreen, B.; Kotov, D.V. Numerical Dissipation Control in High Order Methods for Compressible Turbulence: Recent Development. *Fluids* **2024**, *9*, 127. [CrossRef]

4. Kotov, D.V.; Yee, H.C.; Wray, A.A.; Hadjadj, A.; Sjögreen, B. High Order Numerical Methods for the Dynamic SGS Model of Turbulent Flows with Shocks. *Commun. Comput. Phys.* **2016**, *19*, 273–300. [CrossRef]
5. Kotov, D.V.; Yee, H.C.; Wray, A.A.; Sjögreen, B.; Kritsuk, A.G. Numerical dissipation control in high order shock-capturing schemes for LES of low speed flows. *J. Comput. Phys.* **2016**, *307*, 189–202. [CrossRef]
6. Lafon, A.; Yee, H.C. Dynamical Approach Study of Spurious Steady-State Numerical Solutions for Nonlinear Differential Equations, Part III: The Effects of Nonlinear Source Terms in Reaction-Convection Equations. *Comp. Fluid Dyn.* **1996**, *6*, 1–36. [CrossRef]
7. Lafon, A.; Yee, H.C. Dynamical Approach Study of Spurious Steady-State Numerical Solutions of Nonlinear Differential Equations, Part IV: Stability vs. Numerical Treatment of Nonlinear Source Terms. *Comput. Fluid Dyn.* **1996**, *6*, 89–123. [CrossRef]
8. LeVeque, R.J.; Yee, H.C. A Study of Numerical Methods for Hyperbolic Conservation Laws with Stiff Source Terms. *J. Comp. Phys.* **1990**, *86*, 187–210. [CrossRef]
9. Sandham, N.D.; Li, Q.; Yee, H.C. Entropy Splitting for High-Order Numerical Simulation of Compressible Turbulence. *J. Comput. Phys.* **2002**, *23*, 307–322.
10. Sjögreen, B.; Yee, H.C. Multiresolution Wavelet Based Adaptive Numerical Dissipation Control for Shock-Turbulence Computation. *J. Sci. Comput.* **2004**, *20*, 211–255. [CrossRef]
11. Sjögreen, B.; Yee, H.C. Accuracy Consideration by DRP Schemes for DNS and LES of Compressible Flow Computations. *Comput. Fluids* **2017**, *159*, 123–136. [CrossRef]
12. Sjögreen, B.; Yee, H.C. Entropy Stable Method for the Euler Equations Revisited: Central Differencing via Entropy Splitting and SBP. *Sci. Comput.* **2019**, *81*, 1359–1385. [CrossRef]
13. Sjögreen, B.; Yee, H.C.; Kotov, D.V.; AKritsuk, A.G. Skew-Symmetric Splitting for Multiscale Gas Dynamics and MHD Turbulence Flows. *Sci. Comput.* **2020**, *83*, 43. [CrossRef]
14. Sjögreen, B.; Yee, H.C. High Order Compact Central Spatial Discretization Under the Framework of Entropy Split Methods. In Proceedings of the ICOSAHOM21, Vienna, Austria, 12–16 July 2021.
15. Sjögreen, B.; Yee, H.C. Construction of Conservative Numerical Fluxes for the Entropy Split Method. *Comm. Appl. Math. Comput.* **2021**, *5*, 653–678. [CrossRef]
16. Sjögreen, B.; Yee, H.C. Generalization to a Wider Class of Entropy Split Methods for Compressible Ideal MHD. *Comput. Fluids* **2024**, *268*, 106087. [CrossRef]
17. Vinokur, M.; Yee, H.C. Extension of Efficient Low Dissipation High-Order Schemes for 3D Curvilinear Moving Grids. In *Frontiers of Computational Fluid Dynamics, Proceedings of the Robert MacCormack 60th Birthday Conference, 26–28 June 2000*; NASA/TM-2000-209598; World Scientific: Half Moon Bay, CA, USA, 2002.
18. Wang, W.; Yee, H.C.; Shu, C.-W.; Yee, H.C.; Sjögreen, B. High-Order well-balanced schemes and applications to non-equilibrium flow. *J. Comput. Phys.* **2009**, *228*, 6682–6702 [CrossRef]
19. Wang, W.; Yee, H.C.; Sjögreen, B.; Magin, T.; Shu, C.W. Construction of Low Dissipative High-Order Well-Balanced Filter Schemes for Nonequilibrium Flows. *J. Comput. Phys.* **2011**, *230*, 4316–4335. [CrossRef]
20. Wang, W.; Shu, C.W.; Yee, H.C.; Sjögreen, B. High Order Finite Difference Methods with Subcell Resolution for Advection Equations with Stiff Source Terms. *J. Comput. Phys.* **2012**, *231*, 190–214. [CrossRef]
21. Yee, H.C. *A Class of High-Resolution Explicit and Implicit Shock-Capturing Methods*; VKI Lecture Series 1989-04; NASA: Washington, DC, USA, 1989.
22. Yee, H.C.; Klopfer, G.H.; Mongtagné, J.-L. High-Resolution Shock-Capturing Schemes for Inviscid and Viscous Hypersonic Flows. *J. Comput. Phys.* **1990**, *88*, 31–61. [CrossRef]
23. Yee, H.C.; Sweby, P.K.; Griffiths, D.F. Dynamical Approach Study of Spurious Steady-State Numerical Solutions for Nonlinear Differential Equations, Part I: The Dynamics of Time Discretizations and Its Implications for Algorithm Development in Computational Fluid Dynamics, NASA TM-102820, April 1990. *J. Comput. Phys.* **1991**, *97*, 249–310.
24. Yee, H.C.; Sweby, P.K. Dynamical Approach Study of Spurious Steady-State Numerical Solutions for Nonlinear Differential Equations, Part II: Global Asymptotic Behavior of Time Discretizations. *Int. J. Fluid Dyn.* **1995**, *4*, 219–283. [CrossRef]
25. Yee, H.C.; Sandham, N.D.; Djomehri, M.J. Low-Dissipative High Order Shock-Capturing Methods Using Characteristic-Based Filters. *J. Comput. Phys.* **1999**, *150*, 199–238. [CrossRef]
26. Yee, H.C.; Vinokur, M.; Djomehri, M.J. Entropy Splitting and Numerical Dissipation. *J. Comp. Phys.* **2000**, *162*, 33–81. [CrossRef]
27. Yee, H.C.; Sjögreen, B. Development of Low Dissipative High Order Filter Schemes for Multiscale Navier-Stokes and MHD Systems. *J. Comput. Phys.* **2007**, *225*, 910–934. [CrossRef]
28. Yee, H.C.; Sjögreen, B. High Order Filter Methods for Wide Range of Compressible Flow Speeds. In Proceedings of the ICOSAHOM09, Trondheim, Norway, 22–26 June 2009.
29. Yee, H.C.; Sjögreen, B. Comparative Study on a Variety of Structure-Preserving High Order Spatial Discretizations with the Entropy Split Methods for MHD. In Proceedings of the ICOSAHOM21, Virtual, 12–16 July 2021.
30. Yee, H.C.; Sjögreen, B. Recent Advancement of Entropy Split Methods for Compressible Gas Dynamics and MHD. *J. Appl. Math. Comput.* **2023**, *463*, 127545. [CrossRef]
31. Glimm, J.; Cheng, B.; Sharp, D.H.; Kaman, T. A Crisis for the Verification and Validation of Turbulence Simulations. *Phys. D Nonlinear Phenom.* **2020** *404*, 132346. [CrossRef]

32. Doedel, E.J.; Beyn, W.-J. Stability and Multiplicity of Solutions to Discretizations of Nonlinear Ordinary Differential Equations. *SIAM J. Sci. Stat. Comput.* **1981**, *2*, 107–120.
33. Ehrenstein, U.; Koch, W. Nonlinear bifurcation study of plane Poiseuille flow. *J. Fluid Mech.* **1991**, *228*, 111–148.
34. Feigenbaum, M.J. Quantitative Universality for a Class of Nonlinear Transformations. *J. Stat. Phys.* **1978**, *19*, 25–52. [CrossRef]
35. Griffiths, D.G.; Stuart, A.M.; Yee, H.C. Numerical Wave Propagation in Hyperbolic Problems with Nonlinear Source Terms. *SIAM J. Numer. Anal.* **1992**, *29*, 1244–1260. [CrossRef]
36. Jackson, E.A. *Perspectives of Nonlinear Dynamics*; Cambridge University Press: New York, NY, USA, 1989; Volume I.
37. Mitchell, A.R.; Griffiths, D.F. *Beyond the Linearized Stability Limit in Non Linear Problems*; Report NA/88; Department of Mathematical Sciences, University of Dundee: Scotland, UK, 1985.
38. Stewart, I. Bifurcation Theory Old and New. In Proceedings of the IMA Conferences on Dynamics of Numerics and Numerics of Dynamics, Bristol, UK, 31 July–2 August 1990.
39. Stuart, A.M. *Numerical Analysis of Dynamical Systems*; Cambridge University Press: Cambridge, UK, 1994.
40. Kotov, D.V.; Yee, H.C.; Pansei, M.; Prabhu, D.K.; Wray, A.A. Computational Challenges for Simulations Related to the NASA Electric Arc Shock Tube (EAST) Experiments. *J. Comput. Phys.* **2014**, *269*, 215–233. [CrossRef]
41. Wang, W.; Shu, C.W.; Yee, H.C.; Kotov, D.V.; Sjögreen, B. High order finite difference methods with subcell resolution for stiff multispecies detonation capturing. *Comm. Comput. Phys.* **2015**, *17*, 317–336. [CrossRef]
42. Yee, H.C.; Kotov, D.V.; Wang, W.; Shu, C.H. Spurious behavior of shock-capturing methods by the fractional step approach: Problems containing stiff source terms and discontinuities. *J. Comput. Phys.* **2013**, *241*, 266–291. [CrossRef]
43. Azevedo, J.; Ramalho, M.; Azevedo, J. An Investigation into the Origin of the Carbuncle Phenomenon in High Speed CFD Calculations. In Proceedings of the COBEM, Natal, RN, Brazil, 24–28 October 2011.
44. Humphries, A.R. Numerical Analysis of Dynamical Systems. Ph.D. Thesis, University of Bath, Bath, UK, 1993.
45. Kennedy, C.A.; Gruber, A. Reduced Aliasing Formulations of the Convective Terms Within the Navier-Stokes Equations. *J. Comput. Phys.* **2008**, *227*, 1676–1700. [CrossRef]
46. Ranocha, H. Entropy Conserving and Kinetic Energy Preserving Numerical Methods for the Euler Equations Using Summation-by-Parts Operators. In Proceedings of the ICOSAHOM-2018, Imperial College, London, UK, 9–13 July 2018.
47. Yee, H.C.; Shinn, J.L. Semi-Implicit and Fully Implicit Shock-Capturing Methods for Nonequilibrium Flows. In Proceedings of the A/AA 8th Computational Fluid Dynamics Conference, Honolulu, HI, USA, 9–11 June 1987; McCroskey, W.J., Ed.; AIAA-87-1116-CP; AIAA: Washington, DC, USA, 1987; p. 159.
48. Quirk, J.J. A contribution to the great Riemann solver debate, Intern. *J. Num. Meth. Fluids* **1994**, *18*, 55–574.
49. Sanders, R.; Morano, E.; Druguet, M.-C. Multidimensional Dissipation for Upwind Schemes: Stability and Applications to Gas Dynamics. *J. Comput. Phys.* **1998**, *145*, 511–537. [CrossRef]
50. Fleischmann, N.; Adami, S.; Hu, X.Y.; Adams, N.A. A low dissipation method to cure the grid-aligned shock instability. *J. Comput. Phys.* **2020**, *401*, 109004. [CrossRef]
51. Hu, L.; Feng, Z. Development of a Carbuncle-free and low-dissipation Roe-type Scheme: Applications to Multidimensional Euler Flows. *Commun. Nonlinear Sci. Num. Simul.* **2023**, *116*, 106798. [CrossRef]
52. Kemm, F. Heuristical and Numerical Considerations for the Carbuncle Phenomenon. *arXiv* **2017**, arXiv:1507.00666v2. [CrossRef]
53. Montagne, J.-L.; Yee, H.C.; Klopfer, G.H.; Vinokur, M. Hypersonic blunt body computations including real gas effects. In *Nonlinear Hyperbolic Equations—Theory, Computation Methods, and Applications, Proceedings of the 2nd International Conference in Hyperbolic Problems, Aachen, Germany, 14–18 March 1988*; Ballmann, J., Jeltsch, R., Eds.; Vieweg+Teubner Verlag: Wiesbaden, Germany, 1989.
54. Shearer, M.; Schaeffer, D.G.; Marchesin, D.; Paes-Leme, P. Solution of the Riemann Problem for a Prototype 2 × 2 System of Non-Strictly Hyperbolic Conservation Laws. *Arch. Rat. Mech. Anal.* **1987**,*97*, 299–320. [CrossRef]
55. Sullivan, P.P.; Banner, M.L.; Morison, R.P. Turbulent Flow over Steep Steady and Unseady Waves under Strong Wind Forcing. *J. Phys. Ocean.* **2018**, *48*, 3–27. [CrossRef]
56. Olsson, P. Summation by Parts, Projections, and Stability. I. *Math. Comp.* **1995**, *64*, 1035–1065. [CrossRef]
57. Sjögreen, B.; Yee, H.C. On Tenth-Order Central Spatial Schemes. In Proceedings of the TSFP-5, Munich, Germany, 27–29 August 2007.
58. Strand, B. Summation by Parts for Finite Difference Approximations for d/dx. *J. Comput. Phys.* **1996**, 110, 47–97. [CrossRef]
59. Sweby, P.K.; Yee, H.C. On the Dynamics of Some Grid Adaptation Schemes. In Proceedings of the 4th International Conference on Numerical Grid Generation in CFD and Related Fields, Swansea, UK, 6–8 April 1994; RIACS Technical Report 94.02; University College of Swansea: Swansea, UK, 1994.
60. Sweby, P.K.; Lafon, A.; Yee, H.C. On the Dynamics of Computing a Chemically Relaxed Nonequilibrium Flow. In Proceedings of the ICFD Conference on Numerical Methods for Fluid Dynamics, Oxford, UK, 3–6 April 1995.
61. Yee, H.C.; Sweby, P.K. *Global Asymptotic Behavior of Iterative Implicit Schemes*; RIACS Technical Report 93.11; NASA AMES Research Center: Mountain View, CA, USA, 1994.
62. Yee, H.C.; Sweby, P.K. *Dynamical Approach Study of Spurious Steady-State Numerical Solutions for Nonlinear Differential Equations, II. The Dynamics of Numerics of Systems of 2 × 2 ODEs and Its Connection to Finite Discretizations of Nonlinear PDEs*; RNR-92-008; NASA Ames Research Center: Mountain View, CA, USA, 1992.

63. Yee, H.C.; Torczynski, J.R.; Morton, S.A.; Visbal, M.R. ; Sweby, P.K. On Spurious Behavior of CFD Simulations, AIAA 97-1869. In Proceedings of the 13th AIAA Computational Fluid Dynamics Conference, Snowmass, CO, USA, 29 June–2 July 1997. *Int. J. Num. Meth. Fluids* **1999**, *30*, 675–711. [CrossRef]
64. Sjögreen, B.; Yee, H.C. An entropy stable method revisited: Central differencing via entropy splitting and SBP. In Proceedings of the ICOSAHOM-2018, London, UK, 9–13 July 2018.
65. Sjögreen, B.; Yee, H.C. High order entropy conservative central schemes for wide ranges of compressible gas dynamics and MHD flows. *J. Comput. Phys.* **2018**, *364*, 153–185. [CrossRef]
66. Yee, H.C.; Sweby, P.K. On Spurious Behavior of Super-Stable Implicit Methods. *Intern. J. CFD* **1997**, *8*, 265–286. [CrossRef]
67. Oberkampf, W.L.; Roy, C.J. *Verification and Validation in Scientific Computing*; Cambridge University Press: Cambridge, UK, 2010.
68. Beyn, W.-J.; Lorenz, J. Spurious Solutions for Discrete Superlinear Boundary Value Problems. *Computing* **1982**, *28*, 43–51. [CrossRef]
69. Doedel, E. *AUTO: Software for Continuation and Bifurcation Problems in Ordinary Differential Equations*; California Institute of Technology: Pasadena, CA, USA, 1986.
70. Doedel, E. *AUTO: Software for Continuation and Bifurcation Problems in Ordinary Differential Equations*; Concordia University: Montreal, QC, Canada; California Institute of Technology: Pasadena, CA, USA, 2000.
71. Kellogg, R.B.; Shubin, G.R.; Stephens, A.B. Uniqueness and the Cell Reynolds Number. *SIAM J. Numer. Anal.* **1980**, *17*, 733–739. [CrossRef]
72. Peitgen, H.-O.; Saupe, D.; Schmitt, K. Nonlinear Elliptic Boundary Value Problems versus Their Finite Difference Approximations: Numerically Irrelevant Solutions. *J. Reine Angew. Mathematik* **1981**, *322*, 74–117.
73. Schreiber, R.; Keller, H.B. Spurious Solution in Driven Cavity Calculations. *J. Comput. Phys.* **1983**, *49*, 310–333. [CrossRef]
74. Shubin, G.R.; Stephens, A.B.; Glaz, H.M. Steady Shock Tracking and Newton's Method Applied to One-Dimensional Duct Flow. *J. Comput. Phys.* **1981**, *39*, 364–374. [CrossRef]
75. Griffiths, D.F.; Mitchell, A.R. *Stable Periodic Solutions of a Nonlinear Partial Difference Equation in Reaction Diffusion*; Report NA/113; Department of Mathematics and Computer Science, University of Dundee: Scotland, UK, 1988.
76. Iserles, A. *Stability and Dynamics of Numerical Methods for Nonlinear Ordinary Differential Equations*; DAMTP 1988/NAI; University of Cambridge: Cambridge, UK, 1988.
77. Lorenz, E.N. Computational Chaos—A Prelude to Computational Instability. *Physica D* **1989**, *35*, 299–317. [CrossRef]
78. Prüfer, M. Turbulence in Multistep Methods for Initial Value Problems. *SIAM J. Appl. Math.*, **1985**, *45*, 32–69. [CrossRef]
79. Sanz-Serna, J.M.; Vadillo, F. *Nonlinear Instability, the Dynamic Approach*; Watson, G.A., Griffiths, D.F., Eds.; Pitman: London, UK, 1985.
80. Sanz-Serna, J.M. Studies in Numerical Nonlinear Instability I: Why do leapfrog schemes go unstable? *SIAM J. Sci. Stat. Comput.* **1985**, *6*, 923–938. [CrossRef]
81. Sanz-Serna, J.M. *Numerical Ordinary Differential Equations vs. Dynamical Systems*; Applied Mathematics and Computation Report 1990/3; Universidad de Valladolid: Valladolid, Spain, 1990.
82. Aves, M.A.; Griffiths, D.F.; Higham, D.J. Does Error Control Suppress Spuriosity? *SIAM J. Num. Anal.* **1995**, *34*, 756–778. [CrossRef]
83. Corless, R.M. Error Backward. *Contemp. Math.* **1994**, *172*, 31–62.
84. Corless, R.M. What Good Are Numerical Simulations of Chaotic Dynamical Systems? *Comput. Math. Appl.* **1994**, *28*, 107–121. [CrossRef]
85. Dieci, L.; Estep, D. Some Stability Aspects of Schemes for the Adaptive Integration of Stiff Initial Value Problems. *SIAM J. Sci. Stat. Comput.* **1991**, *12*, 1284–1303. [CrossRef]
86. Hairer, E.; Iserles, A.; Sanz-Serna, J.M. Equilibria of Runge-Kutta Methods. *Numer. Math.* **1989**, *58*, 243–254. [CrossRef]
87. Poloashenko, M.; Aidun, C.K. A direct method for computation of simple bifurcations. *J. Comput. Phys.* **1995**, *121*, 246–260. [CrossRef]
88. Stuart, A.M. Probabilistic and Deterministic Convergence Proofs for Software for Initial Value Problems. *Numer. Algorithms* **1997**, *14*, 227–260. [CrossRef]
89. Butcher, J.C. *Numerical Analysis of Ordinary Differential Equations*; John Wiley & Son: Chichester, UK, 1987.
90. Yee, H.C.; Sweby, P.K. *Nonlinear Dynamics & Numerical Uncertainties in CFD*; NASA Technical Memorandum; NASA Ames Research Center: Mountain View, CA, USA, 1996; p. 110398.
91. Bhattacharyya, B. Uncertainty qantification of dynamical systems by a POD-Kriging surrogate model. *J. Comput. Sci.* **2022**, *60*, 101602. [CrossRef]
92. Frohlich, B.; Hose, D.; Dieterich, O.; Hanss, M.; Eberhard, P. Uncertainty quantification of large-scale dynamical systems using parametric model order reducion. *Mech. Syst. Signal Process.* **2022**, *171*, 108855. [CrossRef]
93. Engquist, B.; Sjögreen, B. High Order Shock Capturing Methods. In *CFD Reviews*; Hafez, M., Oshima, K.; Eds.; John Wiley: New York, NY, USA, 1995; pp. 210–233.
94. Moujaes, P.; Kuzmin, D. Monolithic convex limiting and implicit pseudo-time stepping for calculating stead-state solutions of the Euler Equations. *arXiv* **2024**, arXiv:2407.03746v1.
95. Zhu, J.; Shu, C.-W.; Qiu, J. RKDG Methods with Multi-resolution WENO Limiters for Solving Steady-State Problems on Triangular Meshes. *Comm. Appl. Math. Comput.* **2023**, *6*, 1575-1599. [CrossRef]

96. Toro, E.F.; Hidalgo, A. ADER finite volume schemes for nonlinear reaction-diffusion equations. *Appl. Numer. Math.* **2009**, *59*, 73–100. [CrossRef]
97. Toro, E.F. *Riemann Solver & Numerical Methods for Fluid Dynamics*; Springer: Berlin/Heidelberg, Germany, 1997; ISBN 978-3-662-03492-7.
98. Crocco, L. A Suggestion for the Numerical Solution of the Steady Navier-Stokes Equations. *AIAA J.* **1965**, *3*, 1824–1832. [CrossRef]
99. Moretti, G.; Abbett, M. A Time-Dependent Computational Method for Blunt Body Flows. *AIAA J.* **1966**, *4*, 2136–2141. [CrossRef]
100. MacCormack, R.W. *The Effect of Viscosity in Hypervelocity Impact Cratering*; AIAA Paper No. 69–354; American Institute of Aeronautics and Astronautics (AIAA): Cincinnati, OH, USA, 1969.
101. Beam, R.M.; Warming, R.F. An implicit Factored Scheme for the Compressible Navier-Stokes Equations. *AIAA J.* **1978**, *16*, 293–402. [CrossRef]
102. Briley, W.R.; McDonald, H. Solution of the multidimensional compressible Navier-Stokes equations by a generalized implicit method. *J. Comp. Phys.* **1977**, *24*, 372–397. [CrossRef]
103. Steger, J. Implicit Finite-Difference Simulation of Flow about Arbitrary Two Dimensional Geometries. *AIAA J.* **1978**, *16*, 679–686. [CrossRef]
104. Yee, H.C.; Sweby, P.K. On Super-Stable Implicit Methods and Time-Marching Approaches; RIACS Technical Report 95.12; NASA AMES Research Center: Mountain View, CA, USA, 1995; also, Proceedings of the Conference on Numerical Methods for Euler and Navier-Stokes Equations, Montreal, QC, Canada, 14–16 September 1995. *Int. J. Comput. Fluid Dyn.* **1997**, *8*, 265–286.
105. Gimperlain, H.; Grinfeld, M.; Knops, R.J.; Slemrod, M. Non-Uniqueness in Plan Fluid Flows. *arXiv* **2023**, arXiv:2301.09122v2.
106. Keller, H.B. Numerical Solution of Bifurcation and Nonlinear Eigenvalue Problems. In *Applications of Bifurcation Theory*; Rabinowitz, P.H., Ed.; Academic Press: Cambridge, MA, USA, 1977; pp. 359–384.
107. Shroff, G.M.; Keller, H.B. Stabilisation of unstable procedures: The RPM. *SIAM J. Numer. Analy.* **1993**, *30*, 1099–1120. [CrossRef]
108. Davidson, B. Large Scale Continuation and Numerical Bifurcation for PDE's. *SIAM J. Numer. Anal.* **1997**, *34*, 2008–2027. [CrossRef]
109. Stephens, A.B.; Shubin, G.R. Multiple Solutions and Bifurcation of Finite Difference Approximations to Some Steady Problems of Fluid Dynamics. *SIAM J. Sci. Stat. Comput.* **1981**, *2*, 404–415. [CrossRef]
110. Fortin, A.; Jardak, M.; Gervais, J.J.; Pierre, R. Localization of Hopf Bifurcations in Fluid Flow Problems. *Intern. J. Numer. Meth. Fluids* **1997**, *24*, 1185–1210. [CrossRef]
111. Thompson, J.M.T. and Stewart, H.B. *Nonlinear Dynamics and Chaos*; John Wiley: Hoboken, NJ, USA, 1986.
112. Hoppensteadt, F.C. *Analysis and Simulation of Chaotic Systems*; Springer: New York, NY, USA, 1993.
113. De Markus, A.S.; Mickens, R.E. Suppression of Numerically Induced Chaos with Nonstandard Finite Difference Schemes. *J. Comput. Appl. Math.* **1999**, *106*, 317–324. [CrossRef]
114. de Markus, A.S.; Mickens, R.E. Reduction of Computational Errors Using Nonstandard Finite Difference Models. *Differ. Eqn. Appl.* **2005**, *1*, 83–91. [CrossRef]
115. Seydel, R. *From Equilibrium to Chaos*; Elsevier: New York, NY, USA, 1988.
116. Hsu, C.S. *Cell-to-Cell Mapping*; Springer: New York, NY, USA, 1987.
117. Friedman, M. On Computing Connecting Orbits. In Proceedings of the Conference on Dynamical Numerical Analysis, Atlanta, GA, USA, 14–16 December 1995; Georgia Institute of Technology: Atlanta, GA, USA, 1995.
118. Higham, D.J.; Stuart, A.M. Analysis of the Dynamics of Local Error Control via a Piecewise Continuous Residual. *BIT Numer. Math.* **1998**, *38*, 44–57. [CrossRef]
119. Yee, H.C.; Sweby, P.K. *Dynamics of Numerics & Spurious Behaviors in CFD Computations, Proceedings of the 7th ISCFD Conference, Beijing, China, 15–19 September 1997*; RIACS Technical Report 97.06; NASA: Washington, DC, USA, 1997.
120. Sjögreen, B.; Yee, H.C. On Entropy Splitting, Linear and Nonlinear Numerical Dissipations and Long-Time Integrations. In Proceedings of the 5th Internattional Conference on Spectral and High Order Methods, Uppsala, Sweden, 11–15 June 2001.
121. Yee, H.C.; Sjögreen, B. Adaptive Numerical-Dissipation/Filter Controls for High Order Numerical Methods. In Proceedings of the 3rd International Conference on DNS/LES, Arlington, TX, USA, 4–9 August 2001.
122. Yee, H.C.; Sjögreen, B. Designing Adaptive Low Dissipative High Order Schemes for Long-Time Integrations. In *Turbulent Flow Computation*; Drikakis, D., Geurts, B., Eds.; Springer: New York, NY, USA, 2001; also RIACS Technical Report, Dec. (2001).
123. Pirozzoli, S. Numerical Methods for High-Speed Flows. *Annu. Rev. Fluid Mech.* **2011**, *43*, 163–194. [CrossRef]
124. Griffiths, D.F.; Sweby, P.K.; Yee, H.C. On Spurious Asymptotes Numerical Solutions of Explicit Runge-Kutta Schemes. *IMA J. Numer. Anal.* **1992**, *12*, 319–338. [CrossRef]
125. Bao, W.; Jin, S. The random projection method for hyperbolic conservation laws with stiff reaction terms. *J. Comput. Phys.* **2000**, *163*, 216–248. [CrossRef]
126. Bao, W.; Jin, S. The random projection method for stiff detonation capturing. *SIAM J. Sci. Comput.* **2001**, *23*, 1000–1026. [CrossRef]
127. Bao, W.; Jin, S. The random projection method for stiff multispecies detonation capturing. *J. Comput. Phys.* **2002**, *178*, 37–57. [CrossRef]
128. Chertock, A.; Chu, A.; Kurganov, A. Accurate Deterministic Projection Methods for Stiff Detonation Waves. *Commun. Math. Sci.* **2024**, *22*, 871–910. [CrossRef]
129. Keefe, L.; Moin, P.; Kim, J. The Dimension of Attractors Underlying Periodic Turbulent Poiseuille Flow. *J. Fluid Mech.* **1992**, *242*, 1–29. [CrossRef]
130. Keefe, L. Private communication, 1997. *unpublished*.

131. Moura, A.F.; Gibbons, N.; Wheatley, V.; McIntyre, T.; Jahn, I. Characterization of Supersonic Turbulent Combustion in a Mach-10 Scramjet Combustor. *AIAA J.* **2020**, *58*, 2180–2196. [CrossRef]
132. Grebogi, C.; Ott, E.; Yorke, J.A. Crises, Sudden Changes in Chaotic Attractors, and Transient Chaos. *Physica D* **1983**, *7*, 181–200. [CrossRef]
133. Moore, D.R.; Weiss, N.O.; Wilkins, J.M. The Reliability of Numerical Experiments: Transitions to Chaos in Thermo solutal Convection. *Nonlinearity* **1990**, *3*, 997–1014. [CrossRef]
134. Spalart, P.R.; Moser, R.D.; Rogers, M.M. Spectral methods for the Navier-Stokes equations with one infinite and two periodic directions. *J. Comput. Phys.* **1991**, *96*, 297. [CrossRef]
135. Orszag, S. Accurate solution of the Orr-Sommerfeld stability equation. *J. Fluid Mech.* **1971**, *50*, 689–703. [CrossRef]
136. Herbert, T. *Lecture Notes in Physics 59*; Springer: Berlin/Heidelberg, Germany, 1976; p. 235.
137. Kim, J.; Moin, P.; Moser, R. Turbulence statistics in fully developed channel flow at low Reynolds number. *J. Fluid Mech.* **1987**, *177*, 133–166. [CrossRef]
138. Gresho, P.M.; Gartling, D.K.; Torczynski, J.R.; Cliffe, K.A.; Winters, K.H.; Garratt, T.J.; Spence, A.; Goodrich, J.W. Is the Steady Viscous Incompressible Two?Dimensional Flow Over a Backward-Facing Step at Re = 800 Stable? *Intern. J. Numer. Meth. Fluids* **1993**, *17*, 501–541. [CrossRef]
139. Kaiktsis, L.; Karniadakis, G.E.; Orszag, S.A. Onset of Three-Dimensionality, Equilibria, and Early Transition in Flow Over a Backward-Facing Step. *J. Fluid Mech.* **1991**, *231*, 501–528. [CrossRef]
140. Torczynski, J.R. *A Grid Refinement Study of Two-Dimensional Transient Flow Over a Backward-Facing Step Using a Spectral-Element Method*; Separated Flows; Dutton, J.C., Purtell, L.P., Eds.; ASME: New York, NY, USA, 1993; Volume 149.
141. Kaiktsis, L.; Karniadakis, G.E.; Orszag, S.A. Unsteadiness and Convective Instabilities in Two-Dimensional Flow Over a Backward-Facing Step. *J. Fluid Mech.* **1996**, *321*, 157–187. [CrossRef]
142. Henderson, R.D. Adaptive Spectral Element Methods for Turbulence and Transition. In *High-Order Methods for Computational Physics*; Barth, T.J., Deconinck, H., Eds.; Springer: Berlin/Heidelberg, Germany, 1999.
143. Fischer, P.F.; Mullen, J.S. Filter-Based Stabilization of Spectral Element Methods. *C. R. L'AcadéMie Sci. Ser. I Math.* **2001**, *332*, 265–270. [CrossRef]
144. Maday, Y.; Patera, T.; Rønquist, E.M. An operator-integration-factor splitting method for time-dependent problems: Application to incompressible fluid flow. *J. Sci. Comput.* **1990**, *5*, 263–292. [CrossRef]
145. Harten, A.; Hyman, J.M. Gui-Qiang Chen1 and Philippe G. LeFloch2. *J. Comput. Phys.* **1983**, *50*, 235. [CrossRef]
146. Edney, B.E. *FFA Report 115*; The Aeronautical Research Institute of Sweden: Stockholm, Sweden, 1968; *unpublished*.
147. Wei, L.; Xia, Y. Steady-state simulations of Euler equations by the discontinuous Galerkin method with the hybrid limiter. *J. Comput. Phys.* **2024**, *515*, 113288. [CrossRef]
148. Berkenbosch, A.; Kaasschieter, E.; Klein, R. Detonation Capturing for Stiff Combustion Chemistry. *Combust. Theory Model* **1998**, *2*, 313–348. [CrossRef]
149. Bihari, B.; Schwendeman, D. Multiresolution Schemes for the Reactive Euler Equations. *J. Comput. Phys.* **1999**, *154*, 197–230. [CrossRef]
150. Bourlioux, A.; Majda, A.J.; Roytburd, V. Theoretical and Numerical Structure for Unstable One-Dimensional Detonations. *SIAM J. Appl. Math.* **1991**, *51*, 303–343. [CrossRef]
151. Helzel, C.; LeVeque, R.; Warneke, G. A Modified Fractional Step Method for the Accurate Approximation of Detonation Waves. *SIAM J. Sci. Stat. Comp.* **1999**, *22*, 1489–1510. [CrossRef]
152. Jeltsch, R.; Klingenstein, P. Error Estimators for the Position of Discontinuities in Hyperbolic Conservation Laws with Source Term Which are Solved Using Operator Splitting. *Comput. Vis. Sci.* **1999**, *1*, 231–249. [CrossRef]
153. LeVeque, R.J.; Shyue, K.-M. One-Dimensional Front Tracking Based on High Resolution Wave Propagation Methods. *SIAM J. Sci. Comput.* **1995**, *16*, 348–377. [CrossRef]
154. Pember, R. Numerical Methods for Hyperbolic Conservation Laws with Stiff Relaxation, I. Spurious Solutions. *SIAM J. Appl. Math.* **1993**, *53*, 1293–1330. [CrossRef]
155. Tosatto, L.; Vigevano, L. Numerical Solution of Under-Resolved Detonations. *J. Comp. Phys.* **2008**, *227*, 2317–2343. [CrossRef]
156. Colella, P.; Majda, A.; Roytburd, V. Theoretical and Numerical Structure for Numerical Reacting Waves. *SIAM J. Sci. Stat. Comput.* **1986**, *7*, 1059–1080. [CrossRef]
157. Strang, G. On the Construction and Comparison of Difference Schemes. *SIAM J. Numer. Anal.* **1968**, *5*, 506–517. [CrossRef]
158. Ducros, F.; Laporte, F.; Soulères, T.; Guinot, V.; Moinat, P.; Caruelle, B. High-Order Fluxes for Conservative Skew-Symmetric-Like Schemes in Structured Meshes: Application to Compressible. *Flows J. Comput. Phys.* **2000**, *161*, 114–139. [CrossRef]
159. Kailasanath, K.; Oran, E.; Boris, J.; Young, T. A computational method for determining detonation cell size. In Proceedings of the 23rd Aerospace Sciences Meeting, Reno, NV, USA, 14–17 January 1985.
160. Zhang, X.; Shu, C.-W. Positivity-Preserving High Order Finite Difference WENO Schemes for Compressible Euler Equations. *J. Comput. Phys.* **2012**, *231*, 2245–2258. [CrossRef]
161. Yee, H.C.; Sjögreen, B. Efficient Low Dissipative High Order Schemes for Multiscale MHD Flows, II: Minimization of div **B** Numerical Error. *J. Sci. Comput.* **2006**, *29*, 115–164. [CrossRef]
162. Yee, H.C.; Sjögreen, B. Adaptive Filtering and Limiting in Compact High Order Methods for Multiscale Gas Dynamics and MHD Systems. *Comput. Fluid* **2008**, *37*, 593–619. [CrossRef]

163. Yee, H.C.; Warming, R.F.; Harten, A. Implicit total variation diminishing (TVD) schemes for steady-state calculations. *J. Comput. Phys.* **1985**, *57*, 327–360. [CrossRef]
164. Ching, E.J.; Johnson, R.F.; Kercher, A.D. Postitivity-preserving and entropy-bounded discontinuous Galerkin method for the chemically reating, compressible Euler equations. Part I: The one-dimensional case. *J. Comput. Phys.* **2024**, *505*, 112881. [CrossRef]
165. Corcos, L.P.; Saye, R.I.; Sethian, J.A. A hybrid finite difference level set-implicit mesh discontinuous Galerkin method for multi-layer coating flows. *J. Comput. Phys.* **2024**, *507*, 112960. [CrossRef]
166. Maltsev, V.; Yuan, D.; Jenkins, K.W.; Skote, M.; Tsoutscanis, P. Hybrid discontinuous Galerkin-finite volume techniques for compressible flows on unstructured meshes. *J. Comput. Phys.* **2023**, *473*, 111755. [CrossRef]
167. Sjögreen, B.; Yee, H.C.; Kotov, D.V. Skew-symmetric Splitting and Stability of High Order Central Schemes. *J. Phys. Conf. Ser.* **2017**, *837*, 012019. [CrossRef]
168. Harten, A. The Artificial Compression Method for Computation of Shocks and Contact Discontinuities: (III). Self-Adjusting Hybrid Schemes. *Math. Comput.* **1978**, *32*, 363–389.
169. Roe, P.L. Approximate Riemann Solvers, Parameter Vectors, and Difference Schemes. *J. Comput. Phys.* **1981**, *43*, 357–372. [CrossRef]
170. Ducros, F.; Ferrand, V.; Nicoud, F.; Weber, C.; Darracq, D.; Gacherieu, C.; Poinsot, T. Large-Eddy Simulation of the Shock/Turbulence Interaction. *J. Comput. Phys.* **1999**, *152*, 517–549. [CrossRef]
171. Johnsen, E.; Larsson, J.; Bhagatwala, A.; Cabot, W.; Moin, P.; Olson, B.; Rawat, P.; Shankar, S.; Sjgreen, B.; Yee, H.; et al. Assessment of high-resolution methods for numerical simulations of compressible turbulence with shock waves. *J. Comput. Phys.* **2010**, *229*, 1213–1237. [CrossRef]
172. Palha, A.; Gerritsma, M. A Mass Energy, Enstrophy and Vorticity Conserving (MEEVC) Mimetic Spectral Element Discretization for the 2D Incompressible Navier-Stokes Equations. *J. Comput.* **2017**, *328*, 200–220. [CrossRef]
173. Gassner, G.; Winters, A.R. A Novel Robust Strategy for Discontinuous Galerkin Methods in Computational Fluid Mechanics: Why? When? What? Where? *Front. Phys.* **2021**, *8*, 500690. [CrossRef]
174. Harten, A. On the Symmetric Form of Systems for Conservation Laws with Entropy. *J. Comput. Phys.* **1983**, *49*, 151. [CrossRef]
175. Tadmor, E. Entropy Stability Theory for Difference Approximations of Nonlinear Conservation Laws and Related Time-Dependent Problems. *Acta Numer.* **2003**, 12, 451–512. [CrossRef]
176. Cano, B.; Sanz-Serna, M.J. Error growth in the numerical integration of periodic orbits, with application to Hamiltonian and reversible systems. *SIAM J. Numer. Anal.* **1997**, *34*, 1391–1417. [CrossRef]
177. Blaisdell, G.A.; Spyropoulos, E.T.; Qin, J.H. The Effect of the Formulation of Nonlinear Terms on Aliasing Errors in Spectral Methods. *Appl. Num. Math.* **1996**, *21*, 207–219. [CrossRef]
178. Gerritsen, M.; Olsson, P. Designing an Efficient Solution Strategy for Fluid Flows. I. A Stable High Order Finite Difference Scheme and Sharp Shock Resolution for the Euler Equations. *J. Comput. Phys.* **1996**, *129*, 245–262. [CrossRef]
179. Coppola, G.; Capuano, F.; Pirozzoli, S.; de Luca, L. Numerically Stable Formulations of Convective Terms for Turbulent Compressible Flows. *J. Comput. Phys.* **2019**, *382*, 86–104. [CrossRef]
180. Pirozzoli, S. Generalized conservative approximations of split convective derivative operators. *J. Comput. Phys.* **2010**, *219*, 7180–7190. [CrossRef]
181. Olsson, P.; Oliger, J. *Energy and Maximum Norm Estimates for Nonlinear Conservation Laws*; RIACS Technical Report 94.01; NASA: Washington, DC, USA, 1994.
182. Johansson, S. *High Order Summation by Parts Operator Based on a DRP Scheme Applied to 2D*; Technical Report 2004-050; Uppsala University: Uppsala, Sweden, 2004.
183. Yee, H.C.; Sjögreen, B. Recent Developments in Accuracy and Stability Improvement of Nonlinear filter Methods for DNS and LES of Compressible Flows. *Comput. Fluids* **2018**, *169*, 331–348. [CrossRef]
184. Sjögreen, B.; Yee, H.C.; Vinokur, M. On high order finite-difference metric discretizations satifying GCL on mmoving and deforming grids. *J. Comput. Phys.* **2014**, *265*, 211–220 [CrossRef]
185. Bogey, C.; Bailly, C. A Family of Low dispersive and Low Dissipative Explicit Schemes for Computing the Aerodynamic Noise. In Proceedings of the AIAA-Paper 2002-2509, 8th ARAA/CEAS Aeroacoustics Conference & Exhibit, Breckenridge, CO, USA, 17–19 June 2002.
186. Brambley, E.J. Optimized finite-difference (DRP) schemes perform poorly for decaying or growing oscillations. *J. Comput. Phys.* **2015**, *324*, 258–274. [CrossRef]
187. Tam, C.K.W. *A CAA Primer for Practicing Engineers*; AEDC-TR-08-2; Arnold Engineering Development Center: Arnold Air Force Base, TN, USA, 2008.
188. Tam, C.K.W. *Computational Aeroacoustics: A Wave Number Approach*; Cambridge Aerospace Series; Cambridge University Press: New York, NY, USA, 2012; Volume 33.
189. Sjögreen, B.; Yee, H.C. A New Approach for a Wider Class of Entropy Split Methods for Compressible Gas Dynamics and MHD. In Proceedings of the ICCFD11 Conference, Maui, HI, USA, 11–15 July 2022.
190. Tadmor, E. Numerical Viscosity and the Entropy Condition for Conservative Difference Schemes. *Math. Comput.* **1984**, 43, 369–381. [CrossRef]
191. Bermejo-Moreno, I.; Larsson, J.; Lele, S.K. LES of canonical shock-turbulence interaction. In *Annual Research Briefs, Center for Turbulence Research*; Stanford University: Stanford, CA, USA, 2010; pp. 209–222.

192. Larsson, J.; Lele, S.K. Direct numerical simulation of canonical shock/turbulence interaction. *Phys. Fluids* **2009**, *21*, 101–114. [CrossRef]
193. Lee, S.; Lele, S.K.; Moin, P. Interaction of isotropic turbulence with shock waves: Effect of shock strength. *J. Fluid Mech.* **1997**, *340*, 225–247 [CrossRef]
194. Ristorcelli, J.R.; Blaisdell, G.A. Consistent initial conditions for the DNS of compressible turbulence. *Phys. Fluids* **1997**, *9*, 4–6 [CrossRef]
195. Taylor, G.; Green, A. Mechanism of the Production of Small Eddies from Large Ones. *Proc. R. Soc. Lond. A* **1937**, 158, 499–521.
196. Yee, H.C.; Sjögreen, B. Simulation of Richtmyer-Meshkov Instability by Sixth-order Filter Methods. *Shock Waves J.* **2007**, *17*, 185–193. [CrossRef]
197. Castro, M.J.; Gallardo, J.M.; Marquina, A. Jacobian-Free Incomplete Riemann Solvers. In *Theory, Numerics and Application Problems I: Aachen Germany*; Springer: Berlin/Heidelberg, Germany, 2016; pp. 292–307.
198. *Flash Manual–UserManual.wiki*; University of Chicago: Chicago, IL, USA, 2021.
199. Colella, P.; Woodward, P.R. The Piecewise Parabolic Method (PPM) for Gas-Dynamical Simulations. *J. Comput. Phys.* **1984**, *54*, 174–201. [CrossRef]
200. Gurski, K.F. An HLLC-Type Approximate Riemann Solver for Ideal Magnetohydrodynamics. *SIAM J. Sci. Comput.* **2004**, *25*, 2165–2187. [CrossRef]
201. Li, S. An HLLC Riemann Solver for Magneto-Hydrodynamics. *J. Comput. Phys.* **2005**, *203*, 344–357. [CrossRef]
202. Yee, H.C.; Sjögreen, B. On Entropy Conservation and Kinetic Energy Preservation Methods. In Proceedings of the ICOSAHOM-2019, Paris, France, 1–5 July 2019.